Spin-Exchange Optical Pumping with Alkali-Metal Vapors

by

Earl D. Babcock

A dissertation submitted in partial fulfillment

of the requirements for the degree of

Doctor of Philosophy

(Physics)

at the

UNIVERSITY OF WISCONSIN-MADISON

2005

ABSTRACT

While the method of Spin-exchange optical pumping, SEOP, of noble gases has existed since 1960 [Bouchiat60], many fundamental aspects of spin exchange optical pumping have gone largely unexplained. These questions included the values of the rate coefficients for spin-exchange, many aspects of the alkali-metal polarization and density inside the SEOP cells, the mechanisms of ^{3}He wall relaxation, non-ideal values of the observed ^{3}He polarization, and efficiency to produce it. This thesis describes the results of our efforts to quantity all parameters in SEOP and to begin to determine some of these unknowns. This thesis presents measurements of spin-exchange rate coefficients and efficiencies. A method to extend SEOP to multiple alkali species is presented. In addition, limits to the efficiency of optical pumping, the efficiency of spin-exchange, and the observed ^{3}He polarization are explored.

CONTENTS

LIST OF FIGURES

LIST OF TABLES

1. INTRODUCTION

1.1 Motivation

Nuclear spin-polarized ^{3}He and optically pumped alkali-metal vapors are used in many areas of physics research. Optical pumping has been gaining applications in many areas of physics such as optically pumped atomic clocks [Jau04], and atomic magnetmeters [Allred02]. Further, spin exchange between optically pumped alkali-metals and ^{3}He or ^{129}Xe is gaining increasing popularity to create samples of highly polarized noble gas nuclei [Chann03, Babcock03]. The extremely high values of nuclear spin polarization obtained in hyperpolarized noble gases have proven to provide numerous scientific applications in both fundamental and applied fields. Applications of hyperpolarized Noble gas nuclei include; magnetic resonance imaging [Albert94, Moller02], spin-polarized targets [Xu00], neutron spin-filters [Jones00, Chen03] and searches for CPT violation [Bear00].

Spin Exchange Optical Pumping (SEOP) [Bouchiat60, Walker97] is widely used to produce hyperpolarized ^{3}He. The vast majority of SEOP experiments use high-power diode laser arrays [Driehuys96, Chann03] to spin-polarize a Rb vapor by optical pumping [Happer72]. Then spin-exchange collisions between the Rb and ^{3}He atoms transfer the polarization to the ^{3}He via a weak hyperfine coupling between the Rb electron and the ^{3}He nucleus.

In SEOP, D_1 resonant circularly polarized light (at 794.7nm) is absorbed by alkali-

metal vapor contained in a glass cell, thereby depositing angular momentum. Then through collisions with the larger amount of ^{3}He contained in the cell, usually 1 to 8 atmospheres, this angular momentum is transferred from the alkali-metal electrons to the nuclear spin of the ^{3}He. This transfer of angular momentum takes place with a characteristic rate coefficient and efficiency that depends on the alkali metal used.

Traditionally the ^{3}He polarization achieved with SEOP has been on the order of 55% [Rich02]. This limit went largely unexplained due to high levels of uncertainty in the spin-exchange rate coefficient, and alkali density and polarization. Further, the lack of adequate yet convenient laser sources and inconsistency in the SEOP cells placed additional practical limits on the process of SEOP. Much work has been done to reliably produce SEOP cells that produce little ^{3}He relaxation. Some of these cells facilitate ^{3}He relaxation times that approach the dipole-dipole limit to the ^{3}He relaxation [Rich02]. We have developed an external cavity diode laser array that allows us to polarize large volumes of high density Rb vapor, and thus produce spin exchange rates far in excess of the ^{3}He relaxation rate [Babcock05b]. Methods have been developed to measure the alkali density, alkali polarization, spin-exchange rate coefficient and SEOP efficiency by us and by others [Chann02b, Babcock03, Baranga98]. Additionally, we have developed a method that uses mixtures of alkali-metals to increase the SEOP efficiency [Babcock03].

These developments have done much to improve the observed ^{3}He polarizations (to $> 75\%$) and production rate in the practice of SEOP, but many fundamental aspects of SEOP are still poorly understood. These aspects include the fact that the ^{3}He polarization has never been observed to reach parity with the polarization of the alkali metal vapor, and the photon absorption is much higher than the theoretical, ideal value.

However, with the above mentioned advances, we have been able to produce maxi-

mum ^{3}He polarizations of 80% and the highest SEOP efficiencies ever reported [Babcock03, Chann03]. In this thesis I report the details and methods of producing high ^{3}He polarizations and SEOP efficiencies. The details and methods include: the methods to measure all of the parameters in ^{3}He SEOP, the construction and use of our frequency narrowed diode laser optical pumping source, our experimental studies and models of processes in pure Rb optical pumping, Rb spin-exchange, and light absorption in SEOP cells, and optical pumping and spin-exchange using alkali-metal mixtures.

1.2 Overview of SEOP

In spin-exchange optical pumping [Happer72, Walker97, Appelt98], a mixture of normally 50 torr of N_2, 1 to 8 atmospheres of ^{3}He, and alkali metal vapor are contained in a sealed glass cell. The cell is often heated by a flowing hot air system to obtain desirable alkali-metal vapor densities which are normally on the order of 1×10^{14} cm^{-3} to 1×10^{15} cm^{-3}. Circularly polarized light, often from a high-power diode laser, resonant with the $5^2S_{\frac{1}{2}} \rightarrow 5^2P_{\frac{1}{2}}$ transition of Rb at 795 nm, is absorbed by the cell, depositing angular momentum in the alkali-metal electrons. The pressure broadening of the Rb hyperfine levels caused by the ^{3}He and N_2 gas in the cell is on the order of 20 GHz/atm [Romalis97]. This broadening is much greater than the Rb hyperfine splitting, and since the laser linewidth is also much broader the Rb hyperfine splitting, all of the Rb hyperfine levels are pumped equally.

Once the Rb atoms are excited by the laser light, they must decay back to the ground state. If the atoms were allowed to radiatively decay, the resulting fluorescence photons released would be resonant with the optical pumping transition, but would be radiated in random directions. The fluorescence photons would consequently scramble the electron spin polarization we are attempting to accumulate in the Rb ground state.

Therefore a small amount of N_2 gas is added to the cell to collisionally de-excite the Rb faster than the natural exited state lifetime, which is 27 ns [Happer72]. N_2 is normally chosen because it has a large cross section on the order of 50 $Å^2$ with Rb [Hrycyshyn70] and doesn't react with the alkali-metal. A pressure of 50 torr of N_2 will relax the Rb atoms at a rate approximately 10 times faster than the natural lifetime. This excitation energy is deposited in the many vibrational and rotational states of the N_2. This heat is then collisionally transferred to the ^{3}He gas and the walls of the SEOP cell [Walter01]. As a result of this process watts of light are often deposited in the SEOP cells as heat. Consequently, the cell temperatures can be tens of degrees hotter than the ambient temperature of the hot air oven.

The N_2 buffer gas not only returns the Rb atoms to the ground state, but it also collisionally mixes the excited state (and the ground state) with equal probability. Therefore, on average, 1/2 unit of photon angular momentum is deposited in the alkali-metal vapor per unit of photon angular momentum absorbed. Figure 1.1 shows a simplified schematic of optical pumping showing only two Zeeman sublevels. In the optical pumping portion of SEOP, the average photon absorption rate, $\langle \delta\Gamma \rangle$, is given by [Walker97, Appelt98],

$$\langle \delta\Gamma \rangle = (1 - 2\langle S_z \rangle) R_p. \tag{1.1}$$

Here R_p is the pumping rate for unpolarized Rb atoms and $2\langle S_z \rangle$ is the average Rb polarization. The pumping rate is given by [Happer72, Walker97, Appelt98]

$$R_P = \int_0^\infty I(\nu)\sigma(\nu)d\nu, \tag{1.2}$$

where $I(\nu)$ is the intensity of the pumping laser per unit frequency, and $\sigma(\nu)$ is the Rb absorption cross section.

The corresponding rate of change of the average total spin of the Rb atoms, $\langle F_z \rangle$,

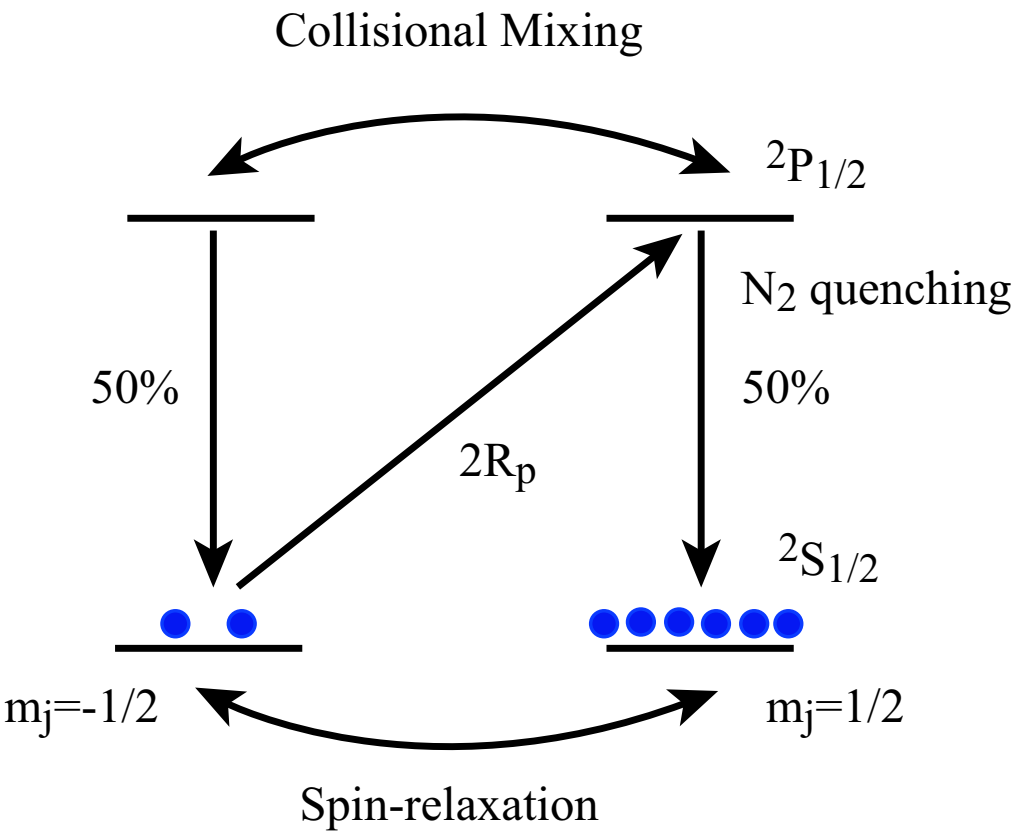

Fig. 1.1: A simplified schematic of optical pumping for a generic $^2S_{1/2} \rightarrow ^2 P_{1/2}$ transition with two Zeeman sublevels.

due to this pumping light is given by,

$$\frac{d\langle F_z\rangle}{dt} = \frac{1}{2}(1 - 2\langle S_z\rangle)R_p - \Gamma_{\mathrm{Rb}}\langle S_z\rangle . \tag{1.3}$$

Here Γ_{Rb} is the total Rb spin relaxation rate. The steady state Rb polarization, $\mathrm{P_{Rb}} = 2\langle \mathrm{S_z}\rangle$, is:

$$P_{\mathrm{Rb}} = \frac{\Gamma_{\mathrm{Rb}}}{\Gamma_{\mathrm{Rb}} + R_p}. \tag{1.4}$$

Given the above assumptions, when the Rb polarization becomes close to 1, the photon absorption rate per Rb atom, $\langle \delta\Gamma \rangle$, should simply be:

$$\langle \delta\Gamma \rangle = \Gamma_{\mathrm{Rb}} P_{\mathrm{Rb}}. \tag{1.5}$$

Consequently, the optical pumping efficiency should approach 100%, meaning that one Rb atom is polarized per photon absorbed.

Once the Rb or other alkali-metal atoms are polarized they undergo spin-exchange collisions with the ^{3}He. These collisions transfer some portion of their spin angular momentum to the ^{3}He nuclei though a weak hyperfine coupling between the alkali-metal electron and the ^{3}He nucleus. This process, spin exchange, constitutes the second step of SEOP [Happer72, Walker97, Appelt98]. Polarization is gained through $^3\mathrm{He} - \mathrm{Rb}$ collisions and is lost by the ^{3}He in other processes such as wall relaxation, He-He collisions, and diffusion though magnetic field gradients at a combined rate of Γ_{He}. The rate of gain of ^{3}He polarization is given by,

$$\frac{dP_{\mathrm{He}}}{dt} = \kappa_{\mathrm{Rb}}[\mathrm{Rb}](P_{\mathrm{Rb}} - P_{\mathrm{He}}) - \Gamma_{\mathrm{He}} P_{\mathrm{He}}, \tag{1.6}$$

were κ_{Rb} is the Rb-^{3}He spin-exchange rate coefficient, [Rb] is the Rb density and Γ_{wall} is the ^{3}He relaxation rate at room temperature. In steady state this gives a ^{3}He polarization of

$$P_{\mathrm{He}} = P_{\mathrm{Rb}} \frac{\kappa_{\mathrm{Rb}}[\mathrm{Rb}]}{\kappa_{\mathrm{Rb}}[\mathrm{Rb}] + \Gamma_{\mathrm{He}}}. \tag{1.7}$$

From this relation one would conclude that if Γ_{He} is sufficiently small for a given cell one would observe P_{He} approach the value of P_{Rb}, but experimentally this has never been the case. The causes of which will be explored in this work.

The Hamiltonian governing the alkali-^{3}He interactions is given as:

$$\mathcal{H} = \mathcal{A}_a \mathrm{I}\cdot\mathrm{S} + g_s\mu_B \mathrm{S}\cdot\mathrm{B} + \mu_{\mathrm{A}}\mathrm{I}\cdot\mathrm{B} + \mu_{\mathrm{He}}\mathrm{K}\cdot\mathrm{B} + \gamma\mathrm{N}\cdot\mathrm{S} + \mathcal{A}_b\mathrm{K}\cdot\mathrm{S} + \mathcal{B}_b\mathrm{K}\cdot(3\hat{\mathrm{R}}\hat{\mathrm{R}} - 1)\cdot\mathrm{S}. \quad (1.8)$$

I, S, and K are the spins of the alkali-metal nucleus, alkali-metal electron, and ^{3}He nucleus respectively. N is the rotational angular momentum of the colliding alkali-metal-^{3}He pair. B is the external applied magnetic field. $\hat{R}$ is the displacement vector between the Alkali-^{3}He pair. The first term, which is the largest, is the hyperfine coupling between the nucleus and electron of the alkali metal. The second, third, and fourth terms are coupling terms to the external magnetic field. The $\gamma\mathrm{N}\cdot\mathrm{S}$ term causes spin relaxation because of the coupling between the spin of the alkali-metal electron and the rotational angular momentum of the alkali-metal-^{3}He pair. The magnitude of the coefficient γ originates from the alkali core electrons and is therefore dependant on the alkali-metal used [Walker89, Walker97]. The $\mathcal{A}_b\mathrm{K}\cdot\mathrm{S}$ term is the term responsible for spin-exchange between the electron spin of the alkali-metal and the ^{3}He nucleus and is called the isotropic hyperfine "Fermi-contact" interaction which aligns the spin of the ^{3}He nucleus and the alkali electron spin. The last term is the anisotropic coupling of the spins of the alkali-metal electron and ^{3}He nucleus due to the long-range classical dipole-dipole interaction [Walter98]. This term is usually ignored because its value is expected to be less than 3% of the $\mathcal{A}_b\mathrm{K}\cdot\mathrm{S}$ term for Rb [Walter98]. However it is important to note that this process would polarize the ^{3}He in an opposite direction to that of the Fermi-contact term and it has never been measured.

The ratio of the values of $\mathcal{A}_b$ to γ is responsible for the obtainable spin-exchange efficiency of a given alkali-metal-^{3}He pair. The $\mathcal{A}_b$ coefficient is expected to be similar

magnitude for all alkali-metals of interest: Cs, Rb, K, and Na [Walker97]. In contrast, the γ is expected to vary by nearly three orders of magnitude, with Cs being the largest and Na the smallest [Walker97]. This trend has been experimentally verified for Rb, K and Na [Baranga98, Borel03, Babcock03]. The resulting maximum spin-exchange efficiencies obtainable are approximately 2% for Rb, 23% for K and up to 90% for Na. Measurements of the spin exchange efficiency and the spin-exchange cross section would allow us to determine both the spin exchange and spin relaxation portions of the Hamiltonian.

1.2.1 Hybrid Spin-Exchange Optical Pumping with K-Rb Mixtures

Although Rb has a low spin-exchange efficiency with ^{3}He, it is experimentally the most common choice because of the ability to optically pump its D_1 line with well developed and inexpensive high-power 795nm diode lasers. Further, multiple effects arising from non-ideal pumping, such as skewed light [Chann02a] and the possibility of fine structure mixing, may actually make Rb much better than the lighter alkali metals for the optical pumping stage, despite its lower spin-exchange efficiency.

Hybrid spin exchange optical pumping, or HySEOP, takes advantage of the increased spin-exchange efficiency of K atoms and combines it with the many experimental advantages of optically pumping Rb atoms. The "hybrid" approach to realizing the higher efficiencies of K or Na spin-exchange was first described in a patent by Happer and co-workers [Happer01] and was recently experimentally verified by our group for a K-Rb alkali-metal vapor mixture [Babcock03]. We optically pump a K-Rb vapor mixture, which can be predominantly K, using a standard Rb laser. Circularly polarized light from a 795nm laser optically pumps the Rb atoms, then spin-exchange collisions between the Rb and K atoms transfer the Rb polarization to the K atoms with little loss. Thus if the K density greatly exceeds the Rb density, ^{3}He polarization is gen-

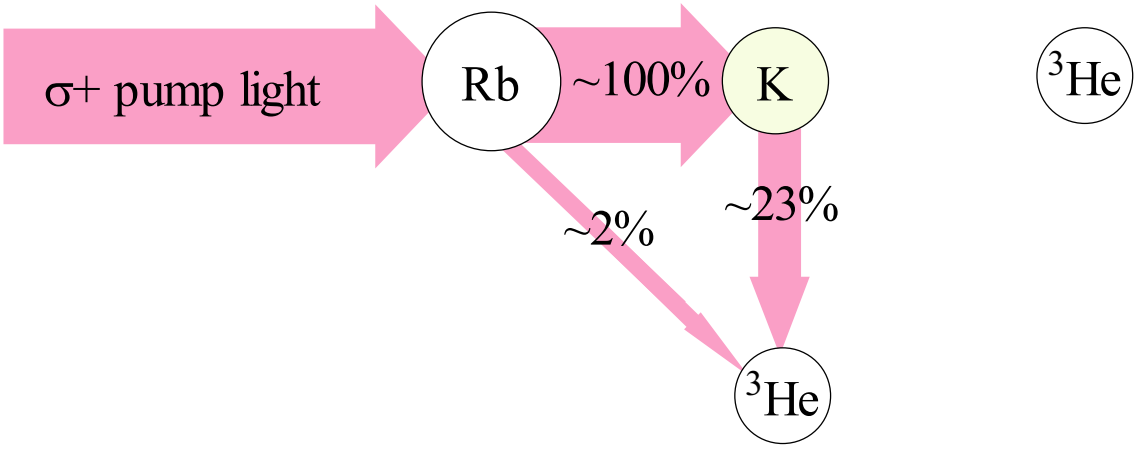

Fig. 1.2: A diagram of HySEOP showing the flow of angular momentum from the pump light. The characteristic efficiencies for each step are shown. If the number density of the K greatly exceeds that of the Rb, the transfer of angular momentum to the ^{3}He will originate almost entirely from highly efficient collisions with K atoms.

erated primarily by highly efficient collisions with K atoms and only slightly via less efficient collisions with Rb atoms. The resulting SEOP efficiency will be an average of the individual efficiencies of the alkali-metals used, weighted by their densities. Figure 1.2 shows a schematic of HySEOP.

In HySEOP the ^{3}He polarization is produced by collisions with polarized K in addition to polarized Rb, and is again lost at a rate of Γ_{He}. Thus in direct analogy to equation 1.6 the HySEOP rate of gain of P_{He} is given by:

$$\frac{dP_{\mathrm{He}}}{dt} = \kappa_{\mathrm{K}}[\mathrm{K}](P_{\mathrm{K}} - P_{\mathrm{He}}) + \kappa_{\mathrm{Rb}}[\mathrm{Rb}](P_{\mathrm{Rb}} - P_{\mathrm{He}}) - \Gamma_{\mathrm{He}}P_{\mathrm{He}}. \tag{1.9}$$

Here κ_{K} is the K spin-exchange rate coefficient and [K] is the K density. The K-Rb spin-exchange cross section is extremely large at roughly 200 Å^2 [Happer72]. Therefore at typical densities of 10^{14} cm^{-3} or more, the K-Rb spin-exchange rate exceeds 10^5 s^{-1} which is much greater than the typical 500 s^{-1} alkali spin-relaxation rates in ^{3}He spin-exchange cells. Thus the K and Rb atoms are in spin-temperature equilib-

rium [Anderson59, Happer72] and have equal electron spin-polarizations P_{A}. With this simplification equation 1.9 becomes

$$\frac{dP_{\mathrm{He}}}{dt} = -\Gamma_{\mathrm{He}} P_{\mathrm{He}} + \Gamma_{\mathrm{SE}}(P_{\mathrm{A}} - P_{\mathrm{He}}), \tag{1.10}$$

where the total hybrid spin-exchange rate is $\Gamma_{\mathrm{SE}} = \kappa_{\mathrm{K}}[\mathrm{K}] + \kappa_{\mathrm{Rb}}[\mathrm{Rb}]$. The rate coefficients for K and Rb are similar in size, therefore the spin transfer rates are nearly proportional to the total alkali density. This equation can be solved in steady state just as with equation 1.6 to obtain an analogous equation to 1.7 where P_{Rb} is replaced by P_{A} and the Rb-^{3}He spin exchange rate is replaced by the total hybrid spin-exchange rate Γ_{SE}.

In HySEOP the advantages to be gained are obvious. We note that the collisional loss of angular momentum for the transfer of spin from the optical pumped Rb atoms to the secondary spin-exchange alkali, in this case K, is negligibly small. Therefore the efficiency of HySEOP becomes the average efficiency of each of the alkalis used weighted by their relative densities.

1.3 Summary of Thesis and Results

1.3.1 Introduction

This thesis contains 8 chapters. The introduction provides an overview of the fundamentals of SEOP and the newly developed HySEOP and outlines the remainder of this thesis. The next two chapters deal with the tools and measurement techniques we have developed to fully study, characterize and implement the SEOP process. This will include a discussion of our high-power frequency narrowed diode array optical pumping source in chapter 2, and ^{3}He and alkali-metal polarization and density diagnostic tools in chapter 3. The next three chapters discuss measurements and results pertaining to

fundamental rates and efficiencies in SEOP. Chapter 4 discusses HySEOP and SEOP efficiency, 5 discusses spin-exchange rate coefficient measurements, and chapter 6 describes EPR frequency shift enhancement factor measurements. The EPR frequency shift enhancement factor is an important constant used to measure absolute ^{3}He polarization. The next two chapters describe processes that place limits on SEOP: extra absorption in optical pumping is discussed in chapter 7, and the remaining unexplained limits to achieved ^{3}He polarization is discussed in chapter 8. This thesis will then be summarized in chapter 9. Appendices will include a general description of optical pumping, spin-temperature, and a section on the fundamental properties of the alkalis.

The following subsections summarize findings presented in each chapter.

1.3.2 Frequency Narrowed Diode Array Bar

In order to polarize large volumes of ^{3}He one must be able to polarize large volumes of Rb at densities ranging from 1×10^{14} cm^{-3} to 1×10^{15} cm^{-3}. To accomplish this one can see, from equation 1.4, it is desirable to have a high pumping rate. We define the power per unit area per unit frequency, or spectral intensity, of the pump laser as the figure of merit for attaining high pumping rates and thus the ability to produce large volumes of highly spin-polarized alkali-metal atoms. Our frequency narrowed diode array bar can produce pumping rates of up to 15 times those of comparable un-narrowed diode array bars.

Diode array bars (DAB) are he most common lasers used in spin-exchange optical pumping because they can provide power up to hundreds of watts relatively easily and inexpensively compared to the other options at 795 nm, namely dye or Ti:Sapphire lasers [Driehuys96]. However, the linewidth of a typical DAB is about 1000 GHz (2 nm). This is much bigger than the absorption linewidth of the Rb atoms, which is 20 GHz/bar [Romalis97]. Conventionally, high ^{3}He or ^{4}He pressures (3 to 8 bar) are

used to broaden the absorption linewidth, but even at 8 bar much of the light cannot be absorbed. In addition, the use of low pressure cells (about 1 bar) is preferred for some applications such as neutron spin filters. Thes low pressure cells further limit the efficiency of using a standard DAB source.

Our frequency narrowed diode array bar, or FNDAB, can reduce the linewidth to approximately 60 GHz. This makes the FNDAB nearly ideally suited for practical optical pumping of Rb.

1.3.3 SEOP Diagnostic Tools and Experimental Setup

To fully study and characterize SEOP and the measurements presented in this thesis, a highly specialized and refined apparatus was needed. Very few measurements of SEOP rate coefficients or efficiencies have been made, largely due to the lack of accurate diagnostics to completely characterize the variables involved.

The work presented in here required many refinements and additional diagnostics to be constructed and implemented in our SEOP apparatus. These additions included an extended temperature forced air oven with non-contact temperature measurement and stabilization, ^{3}He and alkali metal polarization, relaxation rate and density diagnostics, N_2 density measurements, and calibrated photon absorption. We will describe the methods and experimental tools for each of these refinements and additions will be described.

1.3.4 HySEOP Efficiency Measurements

A convenient concept for evaluating SEOP is the efficiency with which light is converted into polarized nuclei. Few measurements of SEOP efficiency have been made [Baranga98, Borel03, Wang03]. Two types of SEOP efficiencies are considered in this thesis: spin-exchange efficiency and photon efficiency. The "photon efficiency" η_γ is

defined as the number of polarized nuclei produced per photon absorbed in the vapor. The "spin-exchange efficiency" η_{SE} is the ratio of the rate at which angular momentum is transferred to the ^{3}He nuclei to the rate at which it is lost by the alkali atoms through various collisional channels [Babcock03]. Baranga et al. [Baranga98] measured spin-exchange efficiencies for Rb and K, and Borel et al. [Borel03] and Wang et al. [Wang03] have made quantitative estimates of photon efficiencies for Na and K respectively. To our knowledge no measurements of Rb photon efficiencies had been reported prior to our results.

The photon efficiency is actually the product of the efficiencies of the two steps involved in SEOP, "optical pumping" efficiency and spin-exchange efficiency. The optical pumping efficiency is simply the ratio of the rate at which Rb atoms gain angular momentum by optical pumping to the rate at which circularly polarized photons are absorbed by the vapor.

The optical pumping efficiency is often assumed to be 100%. If this were the case, the spin exchange efficiency would equal the photon efficiency. In this thesis results of photon efficiency and spin exchange efficiency measurements for both K and Rb are given. Figure 1.3 shows our results of efficiency measurements in K-Rb HySEOP cells. This figure shows that the spin-exchange efficiencies match theoretical expectations [Walker89], but photon efficiencies are nearly a factor of 10 lower under practical conditions. The possible sources and explanations of the much lower than expected photon efficiency are discussed in chapter 4.

1.3.5 Rb-^{3}He and K-^{3}He Spin-Exchange Rate Coefficient Measurements

Prior to this work, for Rb-^{3}He only three measurements of the Rb SEOP rate coefficient, $\kappa_{\mathrm{SE}}^{\mathrm{Rb}}$, had been made. Coulter et al. [Coulter88] determined $\kappa_{\mathrm{SE}}^{\mathrm{Rb}} = 12 \pm 2 \times 10^{-20}$ cm^{3}s^{-1}, whereas Larson et al. [Larson91] found $\kappa_{\mathrm{SE}}^{\mathrm{Rb}} = 6.2 \pm 0.2 \times 10^{-20}$ cm^{3}s^{-1}. Both

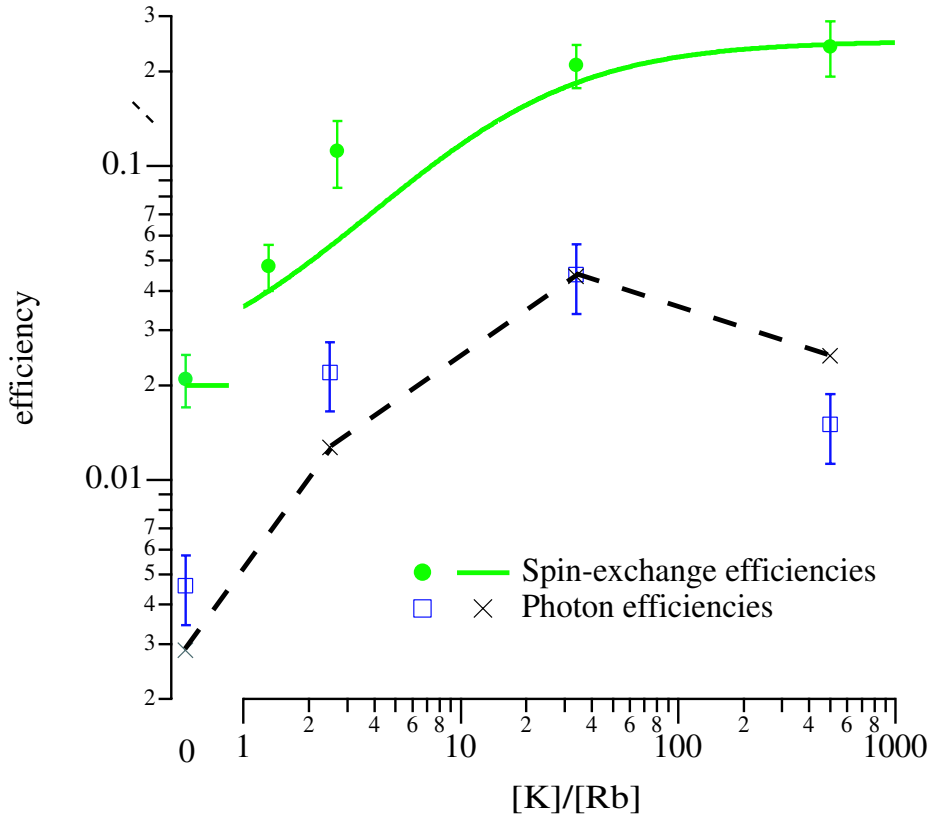

Fig. 1.3: $K - Rb - {}^3$He efficiencies, as a function of the K-Rb density ratio, at a temperature of 190°C. The filled circles are spin-exchange efficiency results, with the associated solid line being the expected values from previous Rb and K efficiency measurements (Ref.[Baranga98]). The hollow squares are photon efficiency measurements for broadband pumping, with the dashed line denoting the expected values corrected for imperfect optical pumping.

groups measured the ^{3}He relaxation as a function of temperature. These measurements relied upon the assumption of a temperature independent ^{3}He wall relaxation, Γ_{wall}, and vapor pressure curves to determine Rb density, [Rb]. However, deducing alkali-metal densities from vapor pressure curves has been shown to induce errors as much as a factor of two or more [Borel02, Jau02]. Baranga et al. [Baranga98] measured $\kappa_{\mathrm{SE}}^{\mathrm{Rb}} = 6.7 \pm 0.6 \times 10^{-20}$ cm^{3}s^{-1} using a method called the "repolarization" method.

This method does not rely on either of the above assumptions and is thus thought to be much more reliable. This method deduces κ_{SE} by measuring the rate, in the absence of optical pumping, at which the alkali atoms regain polarization from spin-exchange with polarized ^{3}He after they have been relaxed.

We also developed a new complementary method to the repolarization method which we call the "rate balance" method. The rate balance method takes advantage of the diagnostic tools developed here to accurately measure alkali density and polarization. This allows us to deduce κ_{SE} from the rate of gain of P_{He} from an alkali-metal vapor of known density and polarization. We note that neither of these methods make any assumptions about the nature of Γ_{He}, the ^{3}He wall relaxation rate.

This work presents measurements of the spin-exchange rate coefficient for Rb-^{3}He using both the repolarization and rate balance methods. Further, both methods were extended for use in HySEOP cells, allowing us to deduce the spin-exchange rate coefficient for K as well. This was accomplished by essentially subtracting off the contribution from ^{3}He spin-exchange with Rb, using the previously determined κ_{SE} for Rb.

By averaging the results of the two methods we obtained a value of $\kappa_{SE}^{Rb} = 6.7 \pm 0.1 \times 10^{-20}$ cm^{3}s^{-1} for Rb-^{3}He, and an average of $\kappa_{SE}^{K} = 5.5 \pm 0.2 \times 10^{-20}$ cm^{3}s^{-1} for K-^{3}He. Our result for Rb-^{3}He agrees very well with the value previously measured by Baranga et al. [Baranga98]. This knowledge of the spin-exchange rate coefficients allowed use to further study and explain the lower than expected values of attainable ^{3}He polarization presented in chapter 8.

1.3.6 EPR Frequency Shift Enhancement Factors for Na, K and Rb

In studying SEOP and HySEOP, it is essential to have a robust and accurate measure of the degree of ^{3}He polarization. It is well established that the alkali-metal EPR

frequency shift in the presence of polarized ^{3}He is a convenient tool for this purpose [Romalis98]. These EPR frequency shifts are proportional to both the ^{3}He polarization and an enhancement factor called κ_0. Previously only the frequency shift enhancement factor for Rb had been measured to high precision [Romalis98] and only for temperatures below $200°C$. Current interest in HySEOP and the use of alkalis other than Rb for SEOP make it important to know the values of κ_0 for the other alkalis, in particular for K and Na, and also to extend the known temperature range for Rb.

This thesis will present measurements κ_0 for K and Na obtained by measuring the ratios of the EPR frequency shifts of K and Na to those of Rb for which the value of κ_0 is well known at temperatures below $200°C$ [Romalis98]. The measured temperature range of κ_0 for Rb was also extended up to $350°C$. Both measurements were accomplished by calibration to the previous low temperature Rb results. The values of κ_0 we obtained for Rb, K and Na respectively are:

$$\kappa_0^{Rb} = 6.39 + 0.00914[\mathrm{T} - 200(^\circ\mathrm{C})], \tag{1.11}$$

$$\kappa_0^{K} = 5.99 + 0.0086[\mathrm{T} - 200(^\circ\mathrm{C})], \tag{1.12}$$

$$\kappa_0^{Na} = 4.84 + 0.00914[\mathrm{T} - 200(^\circ\mathrm{C})]. \tag{1.13}$$

1.3.7 Limits to Photon Efficiency: Light Absorption in Optical Pumping

During the course of these studies on SEOP we have determined that the spin exchange efficiency is limited by imperfect optical pumping [Babcock03]. Two sources that limit the efficiency of optical pumping include skewed light, [Chann02a] and a larger than anticipated off resonant pumping rate of the D_2 resonance.

Skewed light is an effect that causes fully polarized alkali-metal vapors to continue to absorb light when the axis of the optical pumping light is not exactly collinear with the magnetic holding field. This extra absorption is is shown to exceed the ideal case

by a factor of $1+(R/\Gamma)\sin^2\theta$ where R is the optical pumping rate, Γ is the alkali-metal relaxation rate, and θ is the angle between the holding field and the axis of the pumping light. This effect can be readily be minimized by careful collimation and alignment of the pump laser light with the magnetic holding field.

D_2 pumping is an effect caused by the Rb-^{3}He molecular potential, which will be shown to be $P_{3/2}$-like, being resonant with light around the $P_{1/2}$ resonance, causing an effective relaxation. This resonace causes off resonant pumping light to be absorbed by Rb-^{3}He pairs effectively relaxing the alkali-metal spin. This effect is observed by a significant narrowing of the resonance of the circular dichroism of the alkali-metal vapor. This effect causes the maximum achievable polarization to decrease to only 90% for a pump laser linewidth of approximately 2 nm, which is the typical specification for un-narrowed diode array bars. On resonance, with a finite pump laser linewidth, this effect significantly increases the light absorption in an optical pumping cell.

1.3.8 Limits to Observed ^{3}He Polarization, the X-Factor

Traditionally the ^{3}He polarization achieved with SEOP has been on the order of 50%. However this limit was unexplained due to large uncertainties in the spin-exchange rate coefficient, alkali density and polarization; the lack of adequate yet convenient laser sources; and the inconsistency in the SEOP cells. Much work has been done to reliably produce SEOP cells that produce little ^{3}He relaxation. Some of these cells facilitate relaxation times that approach the dipole-dipole limit to ^{3}He relaxation [Rich02]. In addition, our FNDAB allows us to polarize large volumes of high density Rb vapor. Further methods have been developed, including those described in this thesis, to measure the Rb density, Rb polarization and the spin-exchange rate coefficient [Chann02b, Baranga98].

With the above mentioned advances, ^{3}He polarizations on the order of 75% can

readily be obtained. However, given cells with relaxation rates over 20-50 times less than the currently achievable spin-exchange rates, and Rb polarizations in excess of 95%, the ^{3}He polarizations should be even higher, approaching that of the Rb polarization in the limit when the ^{3}He wall relaxation is small compared to the spin exchange rate.

The measured ^{3}He relaxation rate, Γ_{He}, during optical pumping (or loss in the absence of optical pumping) always gives a significantly faster value than the value expected given measured alkali-metal density and spin exchange rate coefficient. The ^{3}He polarization achieved does equal the value of the spin-exchange rate divided by the measured ^{3}He relaxation rate, just as one would expect from a rate balance argument. However, since the measured relaxation rates are faster than anticipated, the resulting value of P_{He} saturates at a value some factor lower than expected. To further complicate matters, this factor seems to vary greatly from one SEOP cell to another, even for cells that are qualitatively physically identical. We have named the proportion of this additional relaxation to that of the spin exchange rate as the "X-factor." for a given SEOP cell.

The value of X measured as a function of the surface area to volume ratio (S/V) for a large number of cells is shown in figure 1.4. While the data in figure 1.4 may appear to be a scattered mess, it gives us important clues into the nature of X. The most important of these clues is the existence of a few low X-factor cells. These cells tell us that the cause of much of the excess relaxation is not a fundamental defect in SEOP, and presumably can be corrected for once it is understood.

Three possible sources are postulated for the extra relaxation mechanism. If the extra relaxation were simply caused by interactions with the walls of the SEOP cells, then one would expect the relaxation to be inversely proportional to the surface to volume ratio of the cells. Second, if the extra relaxation were a bulk effect the extra

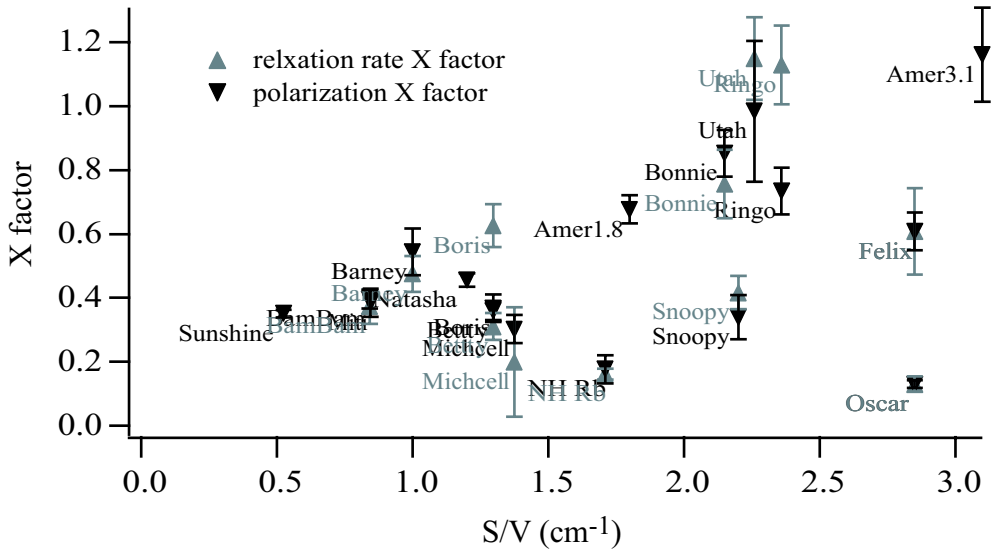

Fig. 1.4: Measured X-factors for a large number of Rb-SEOP cells.

relaxation should be independent of the cell parameters, but show dependance on gas/vapor composition. Third and lastly, if the extra relaxation were a fundamental property of the ^{3}He -Rb interactions, such as anisotropic spin exchange [Walter98], it would be independent of all of these parameters, but depend on the alkali metal used. In this thesis each of these possibilities is discussed.

2. FREQUENCY NARROWED DIODE ARRAY BAR

2.1 Introduction

In this chapter we give an in depth description of the theory and operation of the frequency narrowed diode array bar (FNDAB) and detail the alignment procedures to build one. Un-narrowed high-power DAB's are the most common laser of choice for Rb SEOP; however, the FNDAB we developed can easily out perform un-narrowed DAB's of much higher output powers. Using a FNDAB one can obtain spectral powers (which we define below, in section 2.1.1, as the figure of merit for SEOP pump lasers) of over 10 times those of an un-narrowed DAB. The resulting linewidth, which is on the order of 60 GHz, is well matched to the Rb absorption profile in SEOP cells and thus ideally suited for SEOP. Without the use of this FNDAB, many of the experiments described in this thesis would have been much more difficult if not impossible. This chapter first describes the theory of operation and spectral properties of the FNDAB in section 2.2, and then describes the procedure to build one in section 2.3 [Babcock05b].

2.1.1 Figure of Merit for Lasers Used in SEOP

In spin-exchange optical pumping, resonant circularly-polarized pump light is absorbed by alkali atoms, usually Rb, contained in a sealed glass cell. The transition of interest is ${}^2S_{1/2} \rightarrow {}^2P_{1/2}$ at 795nm. For most practical applications the hyperfine levels are not resolved due to the pressure broadening by the noble gas [Romalis97]. Hence, all

the hyperfine levels are pumped equally. The alkali atoms become spin polarized, then their polarization is transferred to the noble gas nuclei through collisions.

The rate of polarization of the noble gas is given by,

$$[X]\frac{dP_{He}}{dt} = \frac{\Delta\Phi\eta}{V} \tag{2.1}$$

where $\Delta\Phi$ is the absorbed photon flux, η is the Rb-noble gas spin-exchange efficiency, V is the cell volume, and [X] is the noble gas density. Here the ideal absorbed photon flux is given by

$$\Delta\Phi_{ideal} = \frac{\Gamma R_P}{R_P + \Gamma}[A]V, \tag{2.2}$$

where Γ is the alkali relaxation rate, R_p is the pumping rate, and [A] is the alkali density. From equations 2.1 and 2.2 it is apparent that in order to maximize $\Delta\Phi$ and $\frac{dP_{\mathrm{He}}}{dt}$, one desires $R_p \gg \Gamma$. The pumping rate is given by

$$R_P = \int_0^\infty I(\nu)\sigma(\nu)d\nu \simeq \frac{P\pi r_e f c}{A\Delta\nu}, \tag{2.3}$$

where $I(\nu)$ is the intensity of the pumping laser per unit frequency, $\sigma(\nu) = \pi r_e f c g(\nu)$, which is the Rb absorption cross section. Here f is the oscillator strength, $r_e = 2.82 \times 10^{-13}$ cm is the classical electron radius and $g(\nu)$ is a normalized Lorenzian. A is the cross sectional area of the cell being pumped and $\frac{P}{\Delta\nu}$ is the power per unit frequency or spectral power which is the figure of merit for attaining high polarization in spin-exchange optical pumping.

The most common laser used in spin-exchange optical pumping is the diode array bar (DAB) because it can provide power up to hundreds of watts relatively easily and inexpensively compared to the other options at 795 nm, namely dye or Ti:Sapphire lasers[Driehuys96]. However, the linewidth of a typical DAB is about 1000 GHz (2 nm), which is much bigger than the absorption linewidth of the Rb atoms of 20 GHz/bar

[Romalis97]. Conventionally, high ^{3}He or ^{4}He pressures (3 to 10 bar) are used to broaden the absorption linewidth, but even at 10 bar much of the light cannot be absorbed. In addition, some applications such as neutron spin filters prefer low pressure cells (about 1 bar) which further limits the efficiency of using a standard DAB source.

Attempts have been made to increase the efficiency of using diode arrays for optical pumping. Diode arrays of 1-2 emitters (2-4W) have been narrowed with external cavities and used for SEOP showing improved performance [Nelson00, Chupp00]. Further, ref.[Romalis00] describes a method to narrow the linewidth of a 40W DAB by 50% using an etalon to provide feedback, and [Bayram] uses an external cavity to achieve single mode (120 MHz) operation from a 2W single emitter diode array. Our method, first described in [Chann00] and now extended for use at the Rb optical pumping wavelength of 795nm, uses an external cavity to narrow the linewidth of a DAB by as much as a factor of 15.

As a direct comparison, a frequency narrowed DAB, running at 30 W with a linewidth of 65 GHz, produces a pumping rate of 1.6×10^6 1/s for a typical 5 cm diameter, 0.8 bar pressure cell, whereas an unnarrowed DAB running at 60 W and 1000 GHz, has a pumping rate of only 2×10^5 1/s. Stated another way, the frequency narrowed DAB under the above conditions can produce the same pumping rate as 400 W of standard commercially available DAB power. However, even if one chose to attempt to use this much power it would be impractical for experimental use because of difficulties created by cell heating at high laser powers [Walter01] A diagram showing a typical optical pumping apparatus using a frequency narrowed diode array bar is shown in figure 2.1.

Our results from extensive comparisons between our frequency narrowed diode array bar and standard diode array bars are given in reference, showing the clear experimental advantages of using the frequency narrowed laser source.

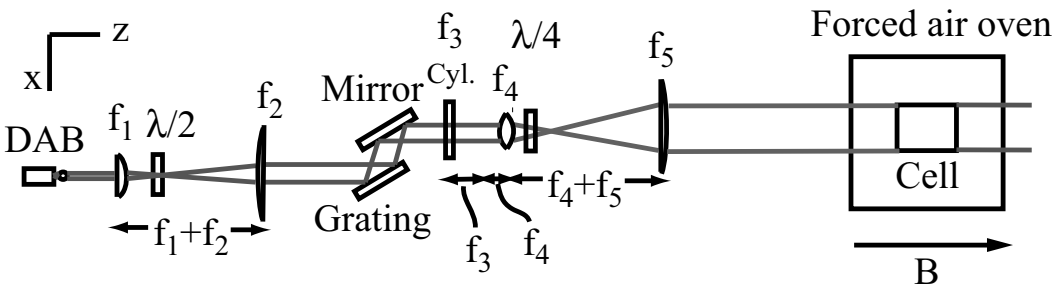

Fig. 2.1: Diagram of a frequency narrowed diode array bar in an optical pumping apparatus5.

2.2 External Cavity Diode Array Bar

A common way to narrow and tune low power single mode diode lasers is to use an external cavity in the Littrow configuration [Wieman91]. In this cavity the laser acts as a near point source with diffraction-limited divergence in both directions so it can be collimated by a single fast aspherical lens. The collimated output is then reflected off a grating. The first order from the diffraction grating is used as a feedback to tune the frequency and reduce the linewidth. The zeroth order is taken as the output.

Using an external cavity for a DAB is more difficult. Each DAB consists of a large number of broad area lasers or emitters (typically 10 to 50), arranged in a length of 1 cm. The dimensions of each emitter are typically 1μm by 100μm with a separation between emitters of 200μm to 500μm. Light emitted perpendicular to the array (fast axis) has a typical diffraction-limited divergence of 40 degrees, while light emitted parallel to the array (slow axis) has a divergence of 10 degrees and is in multi-spatial modes. The asymmetric divergence of the individual emitters requires the use of extra collimation optics. Next, since each of these many emitters has its own spatial mode, the emitters cannot be collimated together with one lens, and thus the Littrow condition is not satisfied for each emitter simultaneously. Lastly, most DAB's are not straight; there is a small curvature of the emitter alignment ("smile") which further complicates the

imaging of the DAB. This smile is usually about 2μm to 10μm and can greatly limit the ability to narrow an array in many cases. A picture of the smile of several DAB's is shown in figure 2.6. Consequently the simple cavity described above does not work for a DAB, but we have shown that a slightly more complex version is effective [Chann00].

The cavity that we developed is shown in figure 2.2. Most DAB's are currently available with fast axis collimation which consists of a cylindrical microlens attached directly to the front of the DAB. This cylindrical microlens forms the first critical element of the external cavity. Next an afocal telescope is used to image each emitter onto a Littrow-mounted grating with a constant diffraction angle, θ, for the ideal no smile case as is shown in figure 2.2. Typical magnification of the telescope is about 4 to 5. The frequency-selected first order diffraction from each emitter is then re-imaged back onto itself, while the zeroth order forms the output. If the DAB does not have an attached, pre-aligned cylindrical microlens, section 2.3 describes how to mount and position one by hand.

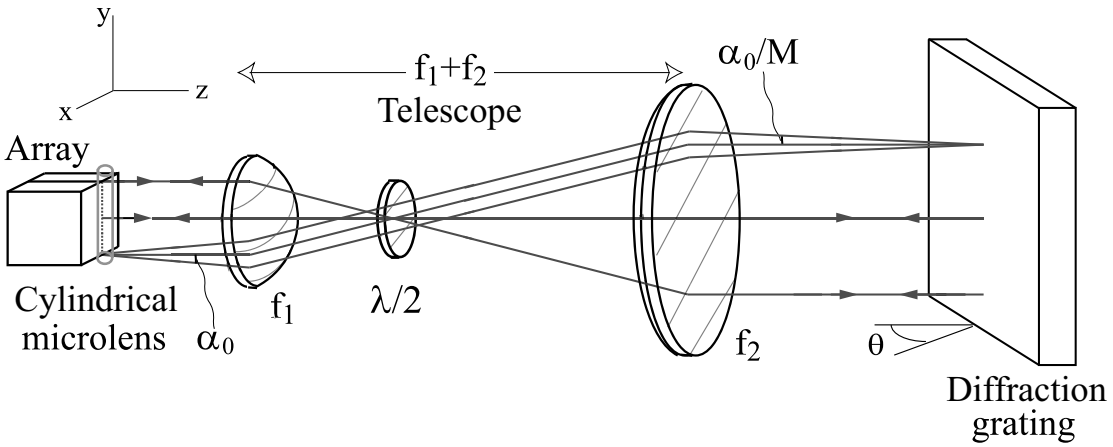

Fig. 2.2: Diagram showing basic components and selected rays of the external cavity diode array bar cavity.

The general equation for the feedback condition in a Littrow cavity for light striking the grating with direction $\hat{z}\cos\alpha\cos\phi + \hat{y}\sin\alpha + \hat{x}\sin\alpha\sin\phi$ with respect to the optical

axis is,

$$\lambda = 2d\sin(\theta - \phi)\cos\alpha \tag{2.4}$$

or

$$\delta\lambda/\lambda_0 \approx -\alpha^2/2 - \phi\cot\theta, \tag{2.5}$$

where θ is the angle between the optical axis and the grating normal that satisfies the condition $\lambda_0 = 2d\sin\theta$. α is the divergence of the light along the slow-axis, and ϕ is the angular spread due to the smile, both of which contribute to broadening of the narrowed laser spectrum. $\delta\lambda = \lambda - \lambda_0$, and the angles α and ϕ are assumed to be small.

The term depending on α represents broadening due to the multi-mode angular distribution of a single emitter along the slow axis. The ϕ term vanishes in the absence of smile. The telescope, shown in figure 2.2, reduces the angular spread from the laser, α_0, by a factor inversely proportional to the magnification of the telescope or $\alpha = \alpha_0/M$, where M is magnification of the telescope. Thus, from equation 2.5 the telescope reduces the α contribution to the laser linewidth by the square of the magnification.

The afocal nature of the telescope causes the angular spread of rays at the grating, from off-axis elements, to be symmetrically centered around zero, providing improved performance over finite focal length imaging lens systems which were also attempted. The telescope reduces angular spread due to the smile to $\phi = x/Mf_c$, where x is the deviation of the laser output from the ideal straight, vertical output caused by the smile of the laser, and f_c is the focal length of the micro-lens. The smile contribution to the linewidth is then

$$\frac{d\lambda}{\lambda} = \frac{x\cot\theta}{Mf_c}. \tag{2.6}$$

Consequently it is easy to see how a large magnification telescope along with a large diffraction angle θ work to minimize the broadening effects caused by smile.

While we have tested many DAB's, we report here narrowing a 60W, 49 emit-

ter array with fast axis collimation from Nuvonyx Inc. The array was selected by the manufacturer to have a smile of about 1μm and center wavelength of 798nm. The cavity consists of a telescope with plano-convex lenses in which the convex surfaces are mounted inward as shown in figure 2.1, providing a magnification $M = 4$, a 40mm×40mm 2400 lines/mm holographic grating, and a $\lambda/2$ plate. Exploiting the different S and P polarization efficiencies of the holographic grating allows the feedback to be adjusted by rotating the $\lambda/2$ plate. The output of the zeroth order beam is then set to about 70% of the free running power by rotating the $\lambda/2$ plate, and the free running wavelength is set to 795nm by adjusting the temperature of the laser cooling water to about 15^oC. The linewidth was measured with a home-made parallel-plate scanning Fabry-Perot spectrometer.

Table 2.1 shows the performance of our cavity with the Nuvonyx array for various output powers.

Tab. 2.1: **Laser performance**

Current (A)	Unnarrowed Power(W)	Narrowed Power(W)	Efficiency (%)	FWHM (GHz)
50	45	30	67	64
37	30	21	70	61
28	20	14.5	72.5	51

Next we set the narrowed output to a moderate power of 16 W and adjusted the wavelength by merely changing the angle of the diffraction grating. Figure 2.3 shows the tuning range and spectral power of the external cavity diode array bar demonstrating a tuning range of over 7nm at the half power points. At the highest output powers, this range decreases slightly to about 4-5nm. Here the unnarrowed spectrum was obtained

with an Ocean Optics Inc. S2000 spectrometer. Also it is important to note that the tuning range can be extended by adjusting the temperature. DAB's have a temperature coefficient of $\frac{2.4nm}{10^oC}$; consequently, the center of the pattern in figure 2.3 can be shifted within the limits of the cooling system and the laser specifications.

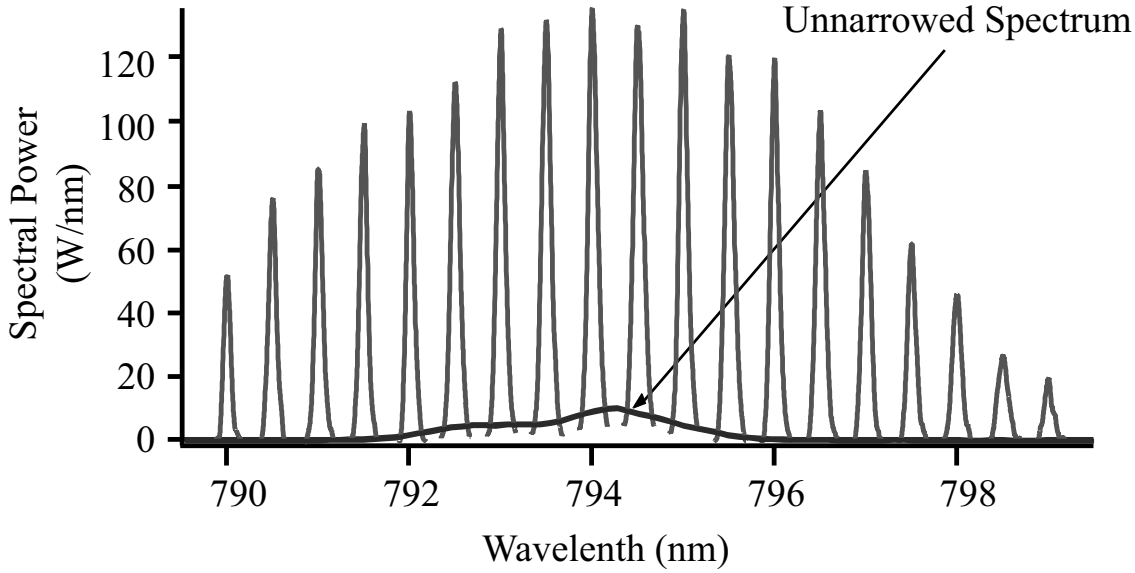

Fig. 2.3: Tuning range and spectral power density of the external cavity diode array bar. The spectral density of the narrowed array is about 10 times greater than the free-running power density.

In order to more fully quantify the full line shape of the laser, we greatly increased the FSR of our parallel-plate Fabry-Perot spectrometer by simply moving the mirrors closer together. To accurately determine the shape of the unnarrowed output as well as provide a good estimate of the proportion of power in the narrowed peak under normal operating conditions, the narrowed peak was tuned approximately 0.5 nm away from the center of the free running laser output, allowing the two contributions to be resolved. The FSR of nearly 2nm required for this measurement caused the instrumental function of our Fabry-Perot to became significant compared to the linewidth of the narrowed

portion of the spectrum. Therefore, the linewidth of narrowed portion had to be measured with the Fabry-Perot set to a lower FSR. Figure 2.4 shows a composite of the unnarrowed portion of the spectrum with the narrowed peak removed, and the narrowed portion. The unnarrowed portion was measured using a FSR of 2 nm while the narrowed portion was measured using a FSR of 0.3 nm. The respective widths for the fits are 0.9nm or 430 GHz for the broad background and 0.14 nm or 60 GHz for the narrowed peak with approximately 75% of the power in the narrowed peak.

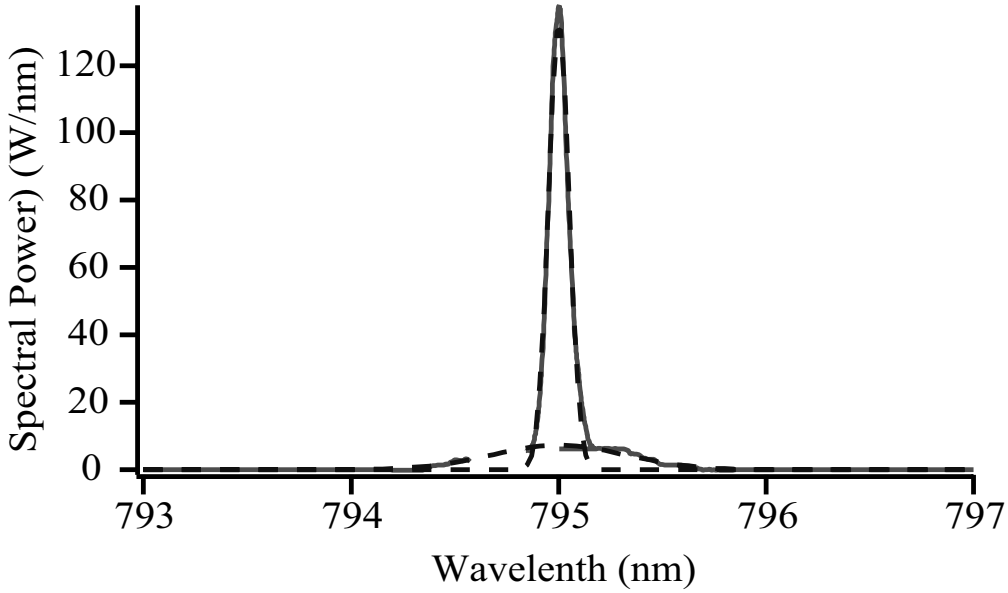

Fig. 2.4: Spectral profile of the frequency narrowed diode array bar. The dotted lines are Gaussian fits. Approximately 75% of the power is in the narrow peak.

We have also successfully narrowed a variety of other DAB's including 19 emitter, 40W, 795nm lasers from Coherent Inc., which did not have fast axis collimation, and several 17W to 20W, 46 emitter, 795nm to 801nm lasers from CEO, with and without fast axis collimation. Using a typical laser from Coherent Inc. with a "smile" of about 2μm, we obtained 14W of power out of about 22W of free-running power. In this case the measured spectral linewidth was 125 GHz at 795 nm, whereas for a particular CEO

laser with 1μm smile running at 12.2W out of 18W free running power the linewidth was only 47 GHz. The increased linewidth was largely due to the contribution from the smile, from equation 2.6 the additional contribution to spectral width just from the smile is about 40 GHz/μm. Second, from the data with the Nuvonyx laser in table 2.1 there is also slight broadening associated with higher output powers.

We recently reported extensive comparisons between spin-exchange optical pumping with a spectrally narrowed Coherent array, and SEOP with standard free running DAB's. The complete details of these tests are provided in [Chann03]. With the Coherent array running narrowed with 14W output at 125 GHz linewidth, the measured rubidium polarization was $> 99\%$ at a temperature as high as 180^{o}C, in a cylindrical cell with diameter 4.7 cm and length 4.9 cm. Using 42W of unnarrowed DAB power (22W from an unnarrowed Coherent DAB and 20W from two Spectra Physics DAB's) the rubidium polarization under the same conditions was only 77%. In the cell used for these measurements, which has a ^{3}He wall relaxation time of 240 hours, the observed ^{3}He polarization was as high as 73% compared to 59% with the unnarrowed arrays. The highest ^{3}He polarization we have produced to date using one of our external cavity diode array bars was 81% in a 3 bar 22.5 cm^3 cell. This is the highest ^{3}He polarization ever obtained with a DAB. Further, in results from our ongoing work in Hybrid SEOP, and results presented later in this thesis, we have shown that under certain conditions unnarrowed DAB's are unable to produce alkali polarizations as high as those obtained with our FNDAB regardless of the amount of power used [Babcock03].

2.3 Detailed Alignment Procedure

The alignment procedures for building an external cavity diode array bar are listed in detail in the following subsections. Here it is assumed that the DAB is already mounted

and operational with the appropriate power supply and adequate cooling source. The first two subsections explain the alignment of the microlens with the array bar. If the DAB has fast axis collimation from the manufacturer the first two subsections can be skipped altogether.

2.3.1 Mount Microlens

To obtain the needed degrees of freedom for aligning the cylindrical microlens, it must be mounted in a mount that allows at least 3 axis rotational adjustment. We use a Newport GM-1R wave plate holder mounted on a 2 axis (x,z) translation stage. To mount the microlens in the wave plate holder, we mill a 2 cm diameter hole in a solid insert, then mill a 1.5mm diameter groove, semicircular in cross section, across the insert. Using glue, the micro cylindrical lens is then attached to the groove and the assembly is put into the wave plate holder. In order to ensure that the distance from the DAB to the lens can be made small enough to collimate the DAB output, on the order of 1mm, the microlens must protrude from the surface of the mount and the machined insert.

2.3.2 Align Microlens

The microlens/translational stage assembly is positioned directly in front of the DAB, ensuring that the center of the microlens and the center of the DAB are at the same height. Then the vertical axis of the diode array bar is approximately aligned with the vertical axis of the microlens. The DAB is then turned on just above its threshold current and the output is observed on a screen about 1 meter away. The microlens is then adjusted carefully though an iterative process until the lens is aligned exactly with the DAB and the fast axis is collimated. At this point the beam size is a few millimeters across, and the microlens is very close to the emitting face of the DAB.

Figure 2.5 shows a picture of the diode array bar mounted on the diode mount with the microlens aligned in front of it.

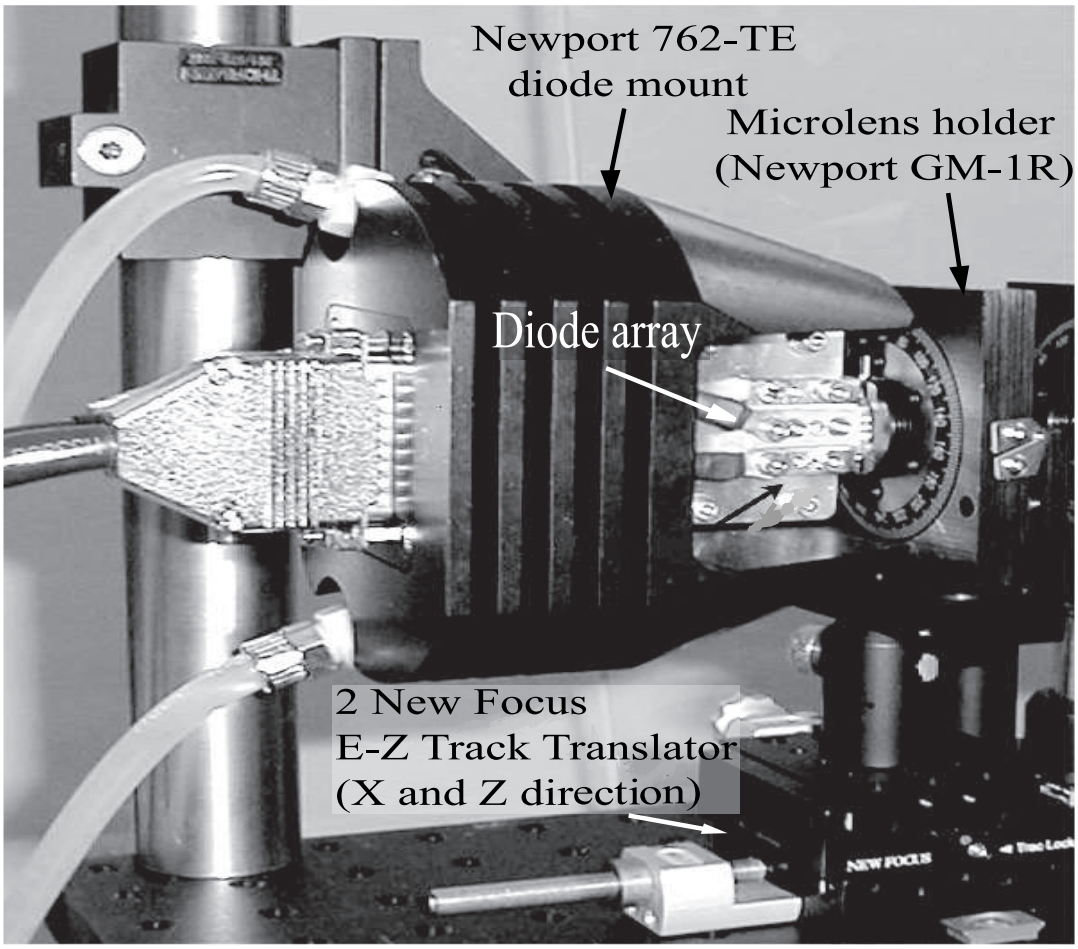

Fig. 2.5: Picture of diode array on the mount with the microlens aligned.

2.3.3 Align telescope

The first telescope lens ($f = 62mm$) is placed at $z \simeq f_1$, making sure that the lens is aligned in the vertical and horizontal direction with the DAB, such that the light from the center of the DAB passes through the center of the lens. The beam is projected onto a large screen or wall several meters from the DAB, and the lens is moved back and forth until the individual emitters of the DAB are imaged in the vertical direction,

forming individual rectangular spots on the screen. Then the $\lambda/2$ plate is placed a few centimeters from the first lens somewhere near its focal plane so that the entire beam can pass through cleanly. The second telescope lens ($f = 250mm$) is then placed at $z \simeq 2f_1 + f_2$, making sure the vertical and horizontal position of the beam is aligned with the diode array bar. This lens is adjusted until the horizontal axis is collimated. If the screen is sufficiently far from the array this will be when the horizontal direction is the narrowest. At this point the beam should be a narrow vertical stripe on the screen. Figure 2.1 shows this arrangement. Note that the lenses shown are plano-convex, which is the preferred choice for minimum aberrations. However, in practice we find that a bi-convex f_2 performs adequately.

2.3.4 Mount and Position Grating

The grating we chose was a 40mm×40mm 2400 line/mm holographic grating. We used this grating in order to accommodate the magnified output of the DAB, to provide a large diffraction angle at $\lambda = 794nm$, and to provide the desired feedback efficiency. This grating is mounted on a 3 rotational axis wave plate holder in order to give the required degrees of freedom for optimal alignment and tuning. The grating is therefore mounted on a GM-1R wave plate holder, like the microlens was, but this time the grating is simply glued to the front of an unmodified insert. At $z \simeq 2f_1 + 2f_2$, there should be a 4×, magnified image of the array with the individual emitters forming sharp rectangular spots in a vertical row as in figure 2.6. The grating is positioned in this image plane, making sure that grooves of the grating are along the vertical direction. Lastly the power output is measured and the $\lambda/2$ plate is rotated until maximum power output is obtained (i.e. minimum feedback). This is to give the greatest sensitivity to the feedback alignment as further adjustments are made, as well as to ensure that the DAB is not damaged with excessive feedback.

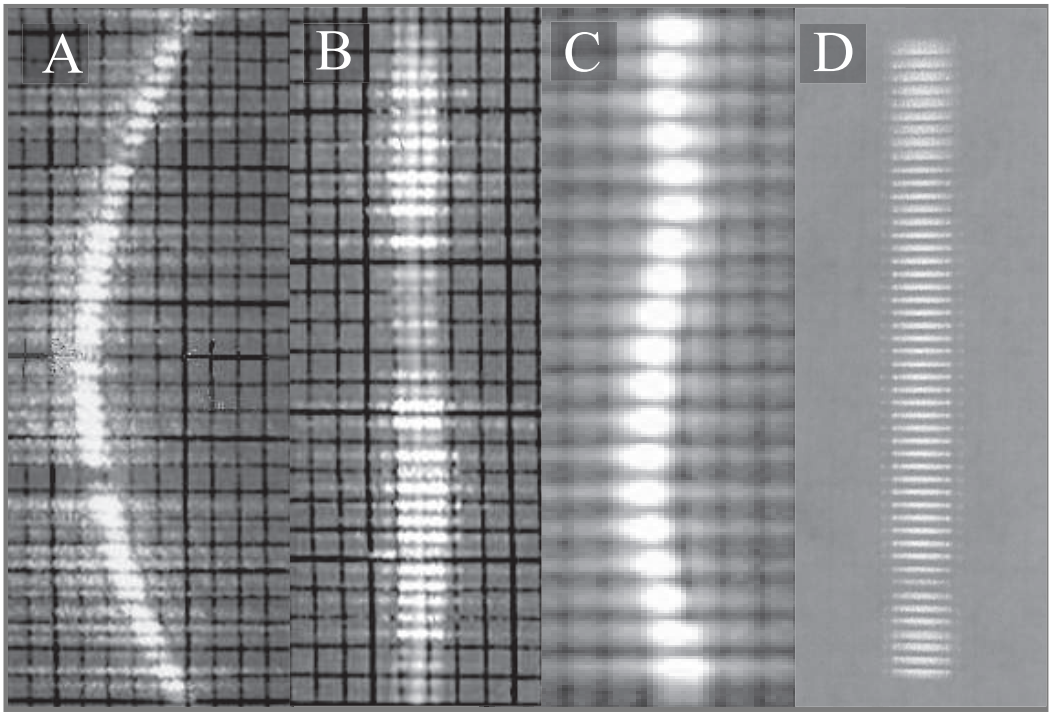

Fig. 2.6: Picture showing the images of 4 different diode array bars. Notice the "smile" or curvature of the laser. A is a picture of a 7 μm smile 46-element CEO laser, B is of a 1 μm smile 46-element CEO laser, C is of a 19-element Coherent laser with 2 μm smile, and D is a 49-element Nuvonyx laser with $< 1\mu$m smile.

2.3.5 Adjust Feedback

Once all the lenses and grating are in place, a spectrometer is used for observing the frequency of the array output in real time; we use an Ocean Optics S2000. Care must be taken to make sure that the spectrometer samples all of the diode bar elements equally, since each emitter essentially acts as a separate laser. A good method is to focus the output beam onto a small spot on a holographic diffuser. The spectrometer is then placed behind the diffuser to sample the light. The angle and tilt of the grating is then adjusted to allow the first order diffraction light to propagate back to the laser co-linear with the original output beam. Thus allowing the first order diffraction to

provide feedback. A narrow peak above a broad background should show up on the spectrometer. The wavelength of this peak can be changed by adjusting the grating angle.

Most likely the external cavity diode array is not working optimally yet and needs further adjustments. From our experience, the most sensitive adjustments are the positions of the microlens and the grating. The goal is to maximize the proportion of power in the tuning peak. Slight adjustments are made to the tilt and rotation of the grating while observing the output on the spectrometer. Once that is maximized, further improvement can sometimes be made with the microlens by adjusting the z position. Extreme caution should be taken with this adjustment because the microlens is very close to the DAB. Once all these adjustments are maximized the feedback is adjusted using the $\lambda/2$ plate until the desired spectrum is obtained. Usually, the feedback required for optimal operation is about 30% of the free-running power output. Finally the laser current is adjusted to give the desired power output.

In order to maintain long lifetimes of our DAB's we do not let the intercavity power exceed the rating of the DAB. The intercavity power is simply the power of the laser before the diffraction grating plus the power in the first order diffraction. This intercavity power is equal to the power before the grating minus the power after the grating. Running in this regime we have obtained DAB lifetimes of over a year running continuously. Consequently we do not feel that the external cavity shortens the normal 10,000 hour DAB lifespan by an appreciable amount. We note that one may be able to run a frequency narrowed diode array bar at higher output powers, perhaps approaching the free running power specification. However we have not attempted any tests of DAB lifetimes under such conditions. Figure 2.7 shows the picture of the external cavity diode array bar.

The highly spatially asymmetric output of the laser is efficiently coupled to a cell

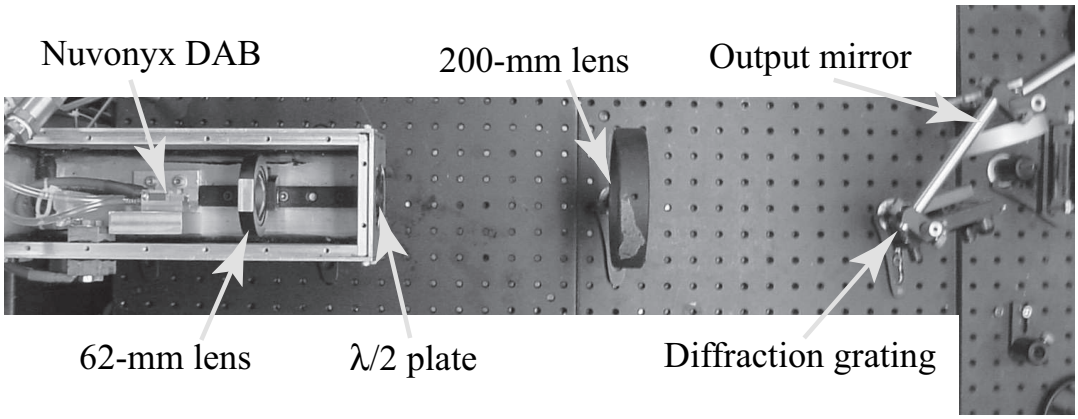

Fig. 2.7: External cavity diode array bar.

using the optical set up as shown in figure 2.8. We have shown that one should use collimated light in optical pumping [Chann02a]. One can normally achieve this by using a cylindrical lens to first focus the elongated laser output to a 4-5 mm square. Then a telescope of arbitrary magnification (10× in this case) is used to produce the desired collimated beam size. Shown in figure 2.8 is a setup for pumping a typical cell with a diameter of 47 mm. Again we note that the ideal choices for the lenses are shown, however, in practice we use a bi-convex f_2 for this telescope, which performs adequately. Depending on the experimental conditions a variation of this scheme can be implemented.

In order to achieve a fixed direction of the output of the cavity as the laser is tuned, and thus a constant input into the cell coupling optics, we place a mirror as shown in figure 2.1. This mirror is mounted such that it remains parallel to the grating as the Littrow diffraction angle is changed, thus fixing the output in a constant direction. Figure 2.7 shows this mirror which is attached to a standard kinematic mount and is mounted to the top of the grating mount using simple posts.

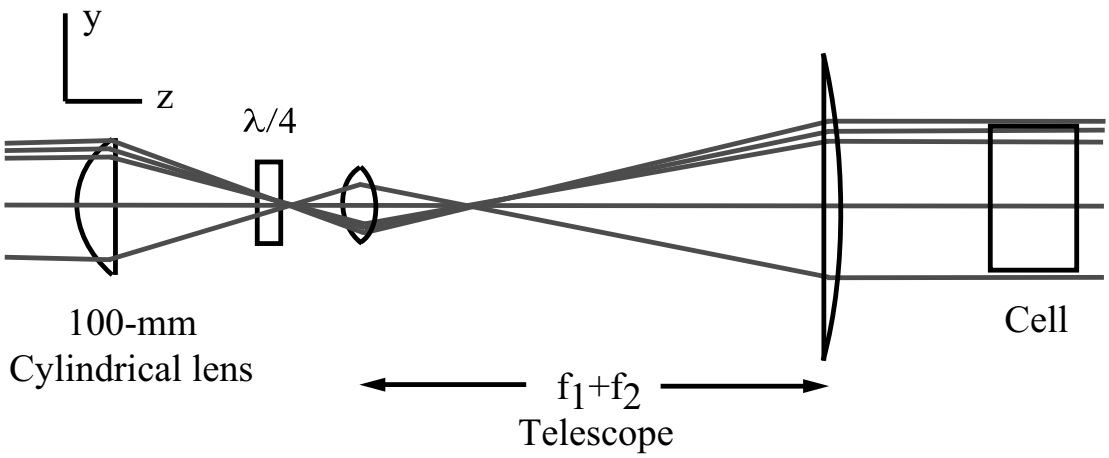

Fig. 2.8: Ray tracing optical setup for the external diode array laser coupling to the cell. The z axis is scaled by 50% relative to the y axis. The grating, not shown, is at z=0. In this example $f_1 = 25mm$ and $f_2 = 250mm$. The cell is typically overfilled to insure uniform Rb polarization. Again note that in practice f_2 is bi-convex.

2.4 Conclusions

We have demonstrated a versatile method for frequency narrowing and tuning various types of diode array bars. The resulting output is highly suited to the demands of efficient spin-exchange optical pumping. Using current technology, it is possible to achieve powers in excess of 30 W at a linewidth of 65 GHz or less with only a 33% loss in output power, with 75% of the total resulting output contained within the narrowed output. We anticipate that if this same technique was applied to an AR coated DAB one could achieve even higher output efficiencies and a wider tuning spectrum, as is currently achieved in external cavities with low power, single mode AR coated diodes that are now commonly commercially available. Further, this technique could also be extended to stacks of several DAB's to obtain narrowed outputs in excess of 100 W.

3. SEOP EXPERIMENTAL DESIGN

3.1 Introduction

The apparatus for producing polarized ^{3}He using SEOP can contain relatively few components. A typical apparatus may consist of little more than field coils to produce a uniform magnetic holding field, a several watt laser which is often a high-power diode array bar, a heat source which is normally hot flowing air with temperature regulation, a SEOP cell, either celled or valved, and often a means to measure ^{3}He polarization, normally calibrated NMR. However for the course of these studies, several modifications and additional diagnostics were required to fully characterize the SEOP process and quantify and explain the many unknowns. A full description of the entire apparatus and all of these diagnostics is included in this chapter.

Figure 3.1 shows a picture of our SEOP apparatus and figure 3.2 gives a schematic diagram. The combination of extensive diagnostics in our apparatus is unprecedented in a single SEOP experiment. The ability to make such a wide variety of complementary measurements has allowed us to discover many new insights into the SEOP process Our FNDAB pump laser, described previously, is used to optically pump the alkali-metal vapors, which are contained in a sealed glass cell inside a flowing hot air oven. The FNDAB light is collimated to be collinear with the holding field from a set of 100 cm diameter Helmholtz coils. The earths field can be compensated for with an additional set of transverse (in the vertical direction) field coils. The oven is capable of

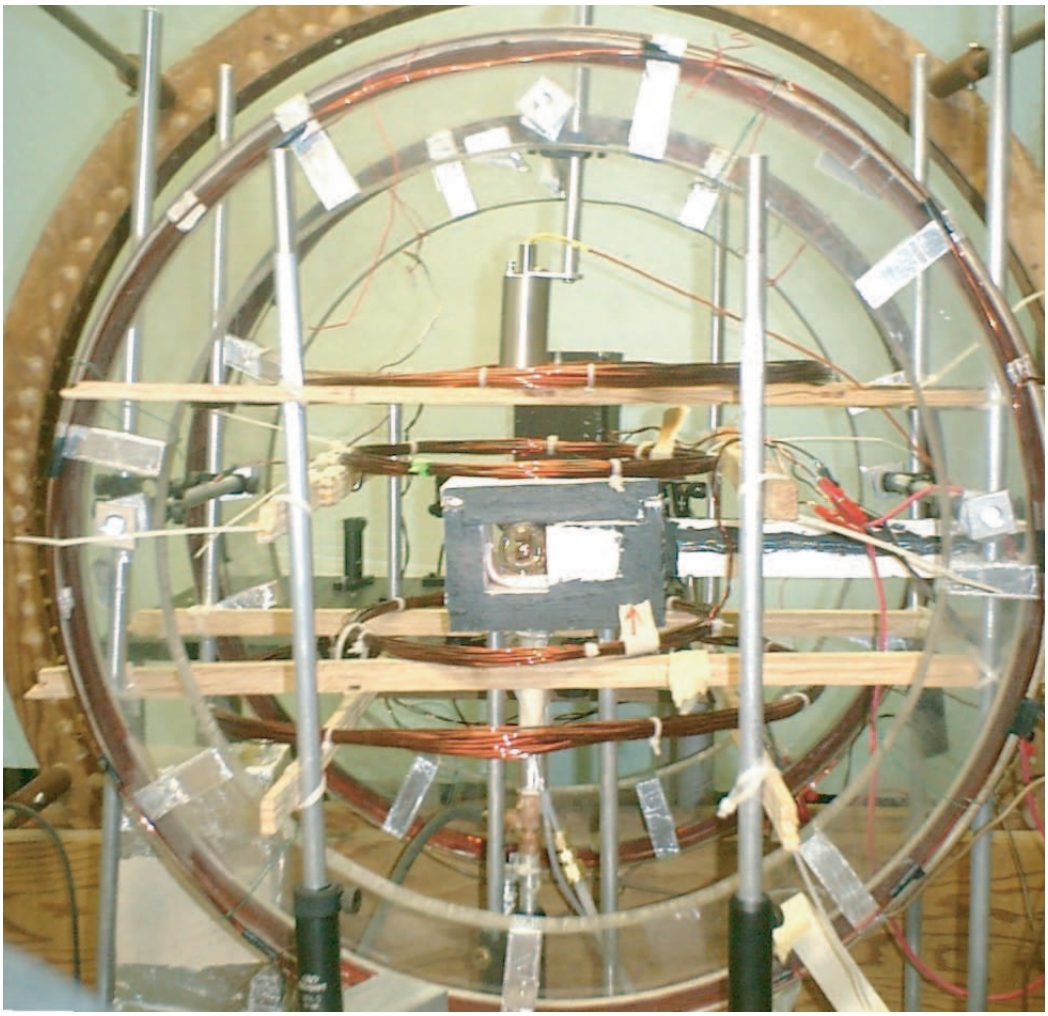

Fig. 3.1: Picture of the SEOP apparatus. A drawing labeling the components is given in 3.2.

temperatures of over 400 $^{\circ}C$ and is temperature stabilized by non-contact temperature measurement of the SEOP cell. Many of our alkali-metal diagnostics are based in the Faraday rotation of a low power, $\ll$ 1 mW, linearly polarized probe laser, also longitudinal with the holding field. This probe is normally tuned to about 2 nm from the Rb D_2 line at 780 nm, but can also be tuned to the K D_1 and D_2 lines at 770 nm and 766 nm respectively. The Faraday rotation of this probe is used to measure the alkali-metal density, and alkali-metal polarization using EPR spectroscopy. This is accomplished with the aid of a tuned EPR rf coil to excite the alkali-metal EPR

transitions and a set of field coils to sweep through the transitions. Further the EPR frequency shifts are used to measure the P_{He} during reversal of the ^{3}He polarization by adiabatic fast passage, AFP. Finally we have a simple un-calibrated NMR free induction decay, FID, setup to measure the relative time dependance of P_{He}.

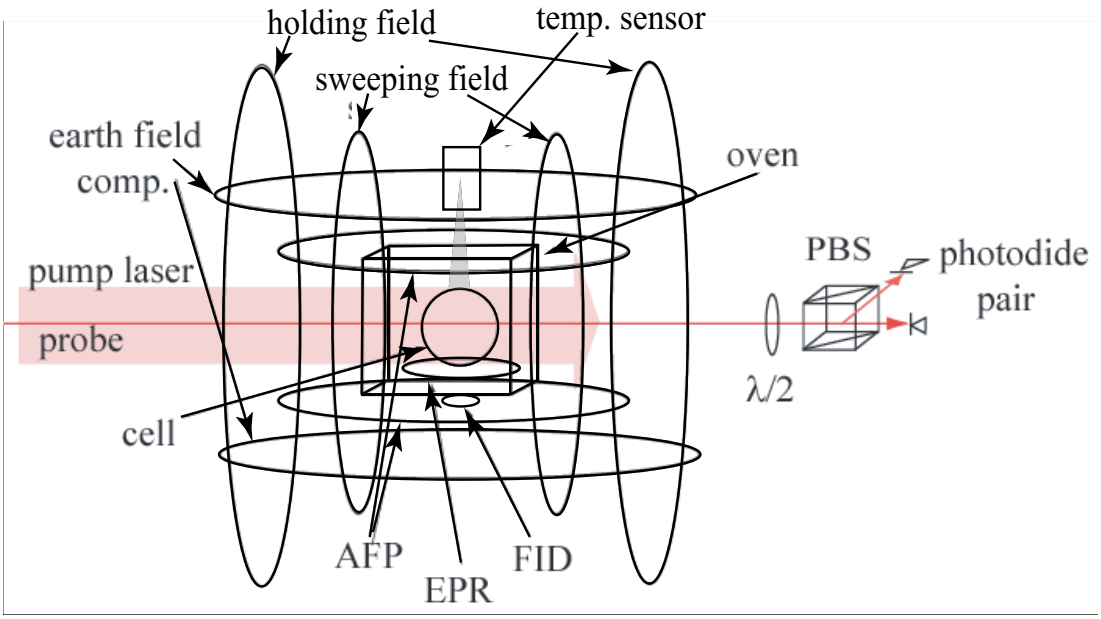

Fig. 3.2: Diagram of our SEOP setup showing all the basic components used for SEOP and diagnostics.

This chapter is divided into 7 sections related to describing techniques to measure all of the fundamental parameters in SEOP. The sections 3.2, 3.3, and 3.4 describe the basic components including the oven to heat the SEOP cells, the field coils, and a description of the many SEOP cells we have performed measurements on. The next section, 3.5, describes the alkali-metal diagnostics including the techniques to measure the alkali-metal polarization, alkali-metal density, alkali-metal spin-relaxation rate, and repolarization of the alkali-metal in the presence of polarized ^{3}He. The following section, 3.6, describes the ^{3}He polarimetry, including NMR FID to measure

^{3}He relaxation rates, absolute ^{3}He polarization using EPR frequency shifts (which includes discussions of the frequency shift enhancement factor), and NMR AFP. The final two sections describe measurements of the density of the ^{3}He and N_2 gas, in section 3.7, and the absolute photon absorption in section 3.8.

3.2 High Temperature Forced Air Oven

^{3}He SEOP is very sensitive to field gradients created by magnetic materials because the field gradients can cause significant ^{3}He polarization relaxation [Cates88]. Thus extreme care must be take to use non-magnetic material whenever it will be in close proximity to the SEOP cell. Our first ovens for Rb-^{3}He SEOP were cubes made from $\frac{1}{2}$" teflon sheets with $\frac{3}{8}$" thick 5"$\times$5" pyrex windows held in place by groves machined into the teflon sides. For temperature stabilization using an optical pyrometer, an additional window made of KBr, or other salt capable of transmitting the black body IR radiation emitted from the surface SEOP cell, is placed in the top of the oven [Omega]. The oven is held together with aluminum screws. Heat is delivered from an Omega ACH series 2 kW process air heater with a maximum exit air temperature of $700°C$ is delivered through an insulated $\frac{3}{8}$" diameter copper tube fitted though a hole in the bottom of the oven. The forced air is provided by an external compressed air source at a flow rate of a few FPM.

The teflon oven is suitable for temperatures up to $210°C$. This is adequate to produce the necessary vapor pressures for Rb, however, the low vapor pressure curves of K and Na require an oven capable of much higher temperatures. For this purpose we constructed a high temperature oven. This oven was similar in form to the teflon ovens but the walls were made of $\frac{1}{2}$" calcium silicate thermal insulation board fastened together using alkali-silicate furnace gasket cement. The windows are either pyrex or

UV fused silica. The materials of this oven, other than the windows, should be capable of withstanding temperatures in excess of $1000°C$ which is far in excess of the highest temperatures required for Na HySEOP. For this high temperature oven the forced air had to be delivered via a braided $\frac{1}{2}$" diameter stainless steel tube. Since stainless steel has a $\mu \simeq 1.004$ it could not be placed close to the SEOP cell [SMCHandbook]. Therefore a $\frac{1}{2}$" I.D. square tube fabricated from the oven materials and cement was used to transport the air the last 30 cm to the oven. Pictures of two of the ovens used are in figure 3.3

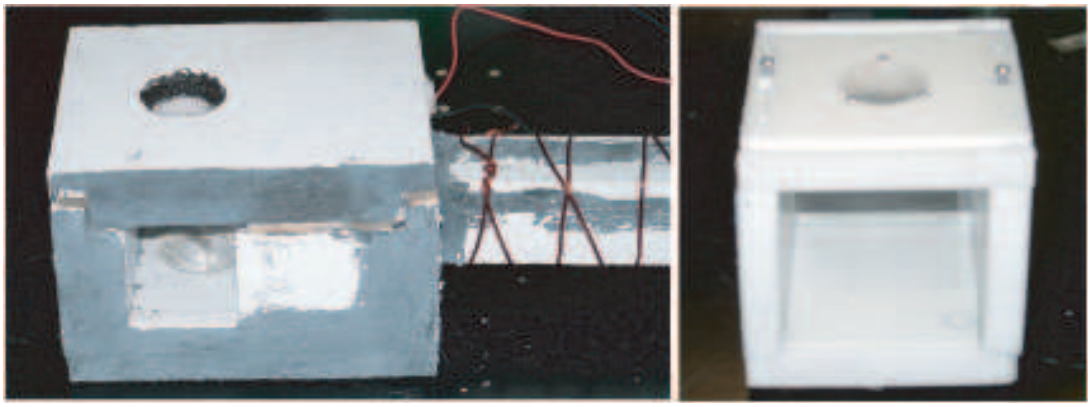

Fig. 3.3: The oven on the left is a calcium silicate high temperature oven, this one has double layer walls and smaller windows to be able to reach temperatures on the order of $500°C$. The oven on the right is a standard Rb SEOP teflon oven.

The temperature of the oven was measured and stabilized by controlling the heater using an Omega Inc. PID, TTL, temperature controller with an Exergen Inc. part no. (IRt/c. 170 K) optical pyrometer placed 20 cm above the cell for the temperature sensor. This sensor has an imaging lens to allow remote measurement, thus it was simply aimed through the KBr window in the top of the oven at a piece of high-temperature fiberglass reinforced aluminum foil tape (with silicon adhesive), blackened with high-temperature flat black enamel, on the top of the SEOP cell. This allows us

to consistently determine the temperature of the cell under optical pumping conditions and compensate for cell heating effects caused by absorption of the pump laser.

3.3 Field Coils

^{3}He SEOP can be done at relatively low fields, we normally run our holding field at 5 to 9 gauss. For diagnostics that require higher fields the holding field coils and sweeping field coils can be used together to provide a maximum D.C. field of 60 gauss for a few hours at a time. Several other D.C. and rf fields are used for our diagnostics, they consist of earth field compensating coils, NMR "Adiabatic Fast Passage" (AFP) coils to reverse the ^{3}He polarization, an NMR "Free Induction Decay" (FID) pulse and sensing coil to measure relative ^{3}He polarization, and an "Electron Paramagnetic Resonance" (EPR) coil to measure alkali polarization and relaxation rate. Figure 3.2 shows all of the field coils used in our setup. Table 3.1 list the specifications and power source of each coil. The apparatus is oriented with the longitudinal axis directed north facing, since the earth's field in Madison Wisconsin is directed upward at approximately 70° and nearly due north, so only one set of compensating coils is required to cancel the earth's field [NGDC].

3.4 SEOP Cells

A critical component of a SEOP apparatus are obviously the SEOP cells. A SEOP cell is typically a closed glass container, either spherical or cylindrical, containing a small amount of alkali-metal, 1 to 8 atmospheres of ^{3}He and $\sim$ 50 torr of N_2 . At Wisconsin we have not duplicated the cell manufacturing capabilities developed extensively at other laboratories. Instead, we have heavily relied many friends who have loaned extraordinary cells to us. Many cells have been loaned and created for us by Tom

Tab. 3.1: Field coils used in this experiment.

Coil	Diameter(cm)	Gauge	Turns	Field(G)	Power source
FID	2	34	300	$\ll 1$	LabView
Holding Field	100	14	135	30	Sorensen DHP
Sweeping Field	59	14	54	30	HP 6574A
AFP	22	14	10	<1	see fig.3.21
EPR	8	14	3	1	see fig.3.23,SRS DG345
Earth Cor.	40	14	20	0.5	HP 6574A

Gentile, Wangchun Chen and Jeff Anderson at NIST-Gaithersberg, but we also have two cells on loan from Bill Hersman at the University of New Hampshire, several on loan from Amersham Health, one from the University of Michigan and one from the University of Utah. The lifetimes (T1) of these cells range from a few hours to over 700 hours with varying glass compositions, gas mixtures, shapes and surface to volume ratios, (S/V). Figure 3.4 and shows several of the SEOP we used in this work. A list containing all of the SEOP cells we used with their specifications is given in figure 3.2.

Betty, Michcell, and Boris are cylinders with Corning 1720 bodies and GE180 flat optical windows, BamBam is also a corning 1720 body but with ^{10}B depleted Corning 1720 windows (to allow high neutron transmission). The remainder of the cells are blown 1 piece GE180. $[^3He]_1$ is the density as measured using Rb absorption spectroscopy, $[^3He]_2$ is the density deduced at the time of filling from a pressure gauge before the cell was "pulled off" of the gas manifold. $[^3He]_3$ is inferred from neutron absorption. $[N_2]$ pressures with a 1 subscript were measured by Rb absorption spectroscopy, the other $[N_2]$ pressures were deduced from the pressure at the time of filling. All the parameters are listed in table 3.2.

Tab. 3.2: List of Rb SEOP cells used in this work. Dimensions listed are, D=diameter for spherical cells, or D=diameter× L=length for cylindrical cells.

Cell name	$[^3He]_1$ (amg)	$[^3He]_2$ (amg)	$[^3He]_3$ (amg)	$[N_2]$ (torr)	Loaned from	T1 (hrs)	Dimensions (cm)	S/V cm^{-1}
Betty	0.74	0.79	0.80	50	NIST	240	4.5×4.9	1.297
BamBam	0.84	.77	.75	50	NIST	119	9.6×4.7	0.842
Natasha	0.6	0.77			NIST	436	5×5	1.2
Saam	2.5			38	Utah	115	3.25	2.7
MITI	2.73			15	N.C.	182	7.1	0.845
Michcell	0.65	0.67			Mich.	8.1	4.3×4.5	1.375
Barney	0.98	1.07		50	NIST	70	4.5×4.9	1
Bonnie		3.17		50	NIST	110	2.8	2.15
Boris		0.77	0.77	50	NIST	70	4.5×4.9	1.297
Sunshine		0.5		50	NIST	550	11.4	0.525
NH Rb	3.2	3.27		98	N.H.	94	3.5	1.714
Felix	2.6		2.8	100_1	NIST	143	1.6×5.05	2.85
Oscar	2.8			175_1	NIST	29	1.6×5.05	2.85
Ringo		3.5		50	NIST		2.5	2.36
Amer1.8		1		6	Amersham	51	4.6×2.1	1.8
Amer3.1		1		6	Amersham	44	2×1.9	3.1
Amer Rb		2		50	Amersham	50	7.1	0.845
Lion		0.51		300	NIST	510	4.5×5	0.845
Tin Man		0.51		150	NIST	80	4.5×5	0.845

Fig. 3.4: Picture of several of the SEOP cells used in this work.

3.4.1 Special Concerns for Hybrid SEOP Cells

Hybrid SEOP places additional requirements on the SEOP cells. First they must be filled with appropriate ratios of alkali-metal in the solid phase to produce desirable density ratios in the vapor phase. Second, the cell's optical surfaces must be able to withstand attack from alkali-metals at the higher temperatures required for HySEOP because of the lower vapor pressure curves of Na and K. Further, K, and especially Na, are more reactive and more apt to etch and darken the glass of the SEOP cells. Table 3.3 lists the HySEOP cells used in this work. Figure 3.5 shows several of the HySEOP cells used in this work. All of the 7.1 cm diameter cells from Amersham Health were

Tab. 3.3: List of cells used for HySEOP studies in this work. A * indicates the cell was valved for gas refilling.

Cell name	2^{nd} alkali	$[^3He]_1$ (amg)	$[^3He]_2$ (amg)	Density ratio	$[N_2]$ (torr)	Loaned from	T1 (hrs)	Geometry (cm)
NH KRb	K	3.3	3.3	1.4:1	98	NH	94	D=3.25
NH Rb		3.3	3.2	0:1	98	NH	145	D=3.25
Amer2.5	K	7.9*		2.5:1	50	Amersham Health	20	D=7.1
Amer34	K	7.9*		34:1	50	Amersham Health	65	D=7.1
Amer2.5	K	7.9*		500:1	50	Amersham Health	55	D=7.1
AmerRb		7.9*		0:1	50	Amersham Health	50	D=7.1
AmerNa	Na	3*		$\sim$ 1:1	50	Amersham Health	254	D=7.1
Sapphire	Na	0.9					0.2	D=2.4,L=5

identical to the one shown.

Since the saturated vapor densities for pure metals obey $[Rb]_0 \gg [K]_0 \gg [Na]_0$ at a given temperature, it is necessary to sublimate from a metal mixture containing a small amount of Rb dissolved into mostly K or Na metal. For a quantitative estimate, we assume that the vapor densities approximately obey Raoult's law [CRC], $[Rb] \approx f_{Rb}[Rb]_0$, where f_{Rb} is the mole fraction of Rb in the metal and $[Rb]_0$ is the saturated vapor density for pure Rb metal. Using saturated vapor curves we estimate that $f_{Rb} \approx$ 3% gives a 10:1 vapor density ratio at 250°C. for Na $f_{Rb} \approx 0.1\%$ gives a 10:1 vapor density ratio at 350°C. Vapor pressure curves useful for this approximation are given in appendix C.

All types of glass will turn black with time in the presence of hot alkali-metal vapors. The most resistant glasses to attack from high temperature alkali-metal vapors are GE180 and Corning 1720 [Souza]. Schott also makes an alkali resistant glass, 8436,

Fig. 3.5: Picture of several of the HySEOP cells used in this work. The slight discoloration of the NH KRb cell due to reactions with high temperature K can be seen in comparison with the NH Rb cell. The body of the Sapphire cells shows the discoloration of glass due to Na after less than 1 week.

whose coefficient of expansion is matched to that of sapphire, (the potential importance of which will be explained below) however we have no experience with SEOP cells made with this glass. It is not in current production and would require a custom lab melt to obtain it. GE180 and Corning 1720 have fair resistance to alkali and will not darken after years of use in standard Rb SEOP. These glasses are also adequate for K-Rb HySEOP, however after approximately 6 mo. of use at temperatures up to 260 $^{\circ}C$, the NH K-Rb cell which was made of GE180 began to form a light brown film. However,

this film has yet to significantly hinder the cells usefulness for HySEOP.

We also attempted to use GE180 for Na-Rb HySEOP (Amer Na-Rb), but this cell became an opaque brown after approximately two weeks of use at temperatures approaching 350 $^{\circ}C$. The most chemically resistant, and optically transparent, material to contain a Na vapor at the temperatures required for Na-Rb HySEOP is sapphire (Al_20_3) or PCA (poly-crystalline alumina also Al_20_3). PCA is often used to contain an Hg-Na amalgams at 400 $^{\circ}C$ in sodium lamps [Souza]. Quartz is also commonly used in high pressure sodium and MH lamps [Lister04]. Gallagher et, al developed a simple method to fuse PCA (or presumably sapphire) windows to a machined PCA body [Gallagher95]. Consequently we feel this method may be adaptable for use in SEOP, further sapphire tubes of up to several inches in diameter with one closed end are commercially available. Researchers at KEK in Japan have worked on development of both quartz and sapphire windowed cells with some success, but at ^{3}He pressures below 1 atmosphere, and only for Rb SEOP [Ino04]. There is a method to seal sapphire windows to glass using rf induction heaters, provided the coefficient of glass is sufficiently well matched to that of the sapphire to prevent cracks from mechanical strain as the seal is cooled. We were able to obtain several 1 inch diameter cells of such construction which had a Kimble-Konts glass body. This glass is engineered for sealing to kovar-steel so it has a slight mismatch in the coefficient of linear expansion with sapphire which limits the maximum size to one inch. Unfortunately these cells produced ^{3}He wall relaxation time constants less than 10 minutes. The exact reason for the surprisingly high wall relaxation is unknown. Based on the experience of our friends with glass bodied cells, it could have resulted from the tooling used to make the cells or the type or purity of the glass itself. Groups have obtained longer lifetimes with Sapphire windowed cells in SEOP so we do not feel it is a property of the sapphire itself [Ino04].

3.5 Alkali-Metal Diagnostics

3.5.1 Alkali-Metal Polarimetry

The method of alkali-metal vapor polarimetry we developed was inspired by, and is a variation of, a method introduced by the optical pumping group at Princeton [Young97]. Their method uses a transverse rf field turned to the Rb EPR resonance frequency to create a polarization dependant transmission of a circularly polarized transverse probe beam modulated at the rf frequency. By scanning the rf frequency across the Zeeman sublevels, the relative populations of the levels are obtained from the relative areas of the transmission peaks created by each sublevel.

The method we developed instead uses the polarization faraday rotation [Kadlecek00, Wu86, Vliegen01] of a longitudinal probe modulated by driving rf transitions between adjacent Zeeman sublevels again with an amplitude modulated transverse sinusoidal magnetic field at the alkali-metal EPR frequency.

The Hamiltonian for an alkali-metal in a transverse sinusoidal magnetic field of amplitude B_x is given by,

$$\mathcal{H} = \sum_m E_m |m\rangle\langle m| + g_s \mu_B S_x B_x \cos(\omega t). \tag{3.1}$$

For well resolved resonances, using the density matrix approach [Happer87, Happer77], the equation of motion for the coherence between states $|m\rangle$ and $|m-1\rangle$, $\rho_{m,m-1}$, is

$$\frac{id\rho_{m,m-1}}{dt} = (E_m - E_{m-1} - \omega)\,\rho_{m,m-1} - i\gamma\rho_{m,m-1} + V_{m,m-1}\,(\rho_{m-1} - \rho_m)\,, \tag{3.2}$$

here ρ_m and ρ_{m-1} is the probability to be in state $|m\rangle$ and $|m\rangle$with energy E_m and E_{m-1} respectively, and γ is the decay rate. If we assume the coherence has the form $\rho_{m,m-1} = \sigma e^{-i\omega t}$, then 3.2 can be rewritten as,

$$\frac{id\sigma}{dt} = (E_m - E_{m-1} - \omega)\,\sigma - \frac{i\rho\sigma}{2} + \langle m|V|m-1\rangle\,\frac{(\rho_{m-1} - \rho_m)}{2} \tag{3.3}$$

where $V = g_s \mu_B S_x B_x$. Solving equation 3.3 in steady state we obtain;

$$\sigma = \frac{\langle m|V|m-1\rangle}{2\left(\Delta + i\gamma/2\right)}\left(\rho_{m-1} - \rho_m\right), \tag{3.4}$$

where $-\Delta = (E_m - E_{m-1} - \omega)$. The equations of motion that describe the behavior of the density of the sublevels $|m\rangle$ and $|m-1\rangle$ are,

$$\frac{id\rho_m}{dt} = \frac{\langle m|V|m-1\rangle\,\sigma^* - \langle m-1|V|m\rangle\,\sigma}{2}, \tag{3.5}$$

$$\frac{id\rho_{m-1}}{dt} = \frac{\langle m-1|V|m\rangle\,\sigma - \langle m|V|m-1\rangle\,\sigma^*}{2}. \tag{3.6}$$

From equations 3.4, 3.5, 3.6, given adequate resolution that only one resonance is driven at a time by the rf field it can be shown that [Chann00],

$$\frac{dF_z}{dt} = \frac{|\langle m|V|m-1\rangle|^2 \gamma\left(\rho_{m-1} - \rho_m\right)}{\Delta^2 + \gamma^2/4} \tag{3.7}$$

$$= \left(\frac{\gamma}{\Delta^2 + \gamma^2/4}\right)\left(\frac{g_s \mu_B B_x}{2I+1}\right)^2 (F(F+1) - m(m-1))\frac{(\rho_{m-1} - \rho_m)}{4}, \tag{3.8}$$

where $dF_z/dt = d(\rho_m - \rho_{m-1})/dt$. Consequently the signal observed will be proportional to $(F(F+1) - m(m-1))(\rho_m - \rho_{m-1})$.

Now from equation 3.8, using the properties of an equilibrium "spin-temperature" distribution of states [Anderson59], the ratio of the areas under two successive peaks will be

$$A = \frac{F(F+1) - m(m-1)}{F(F+1) - (m-1)(m-2)} e^{\beta}. \tag{3.9}$$

The equation for the electron spin polarization in terms of the spin-temperature parameter β is given by [Happer72, Walker97],

$$\mathrm{P} = 2\langle S_z\rangle = tanh(\beta/2) = \frac{e^{\beta/2} - e^{-\beta/2}}{e^{\beta/2} + e^{-\beta/2}} = \frac{e^{\beta} - 1}{e^{\beta} + 1}. \tag{3.10}$$

If we calculate equation 3.9 for ^{85}Rb for $F = I + J = 3$ $(I = 5/2, J = 1/2)$, the ratio of the area of the $F = 3, m_F = -F \rightarrow -F+1$ peak to the $F = 3, m_F = -F+1 \rightarrow -F+2$ peak is

$$A = (3/5)e^{\beta}. \tag{3.11}$$

Therefore the alkali polarization for resolved hyperfine levels in $I = 5/2$ isotopes such as ^{85}Rb becomes

$$P = \frac{5A - 3}{5A + 3}. \tag{3.12}$$

Figure 3.6 shows an example spectrum where all of the resonances are resolved.

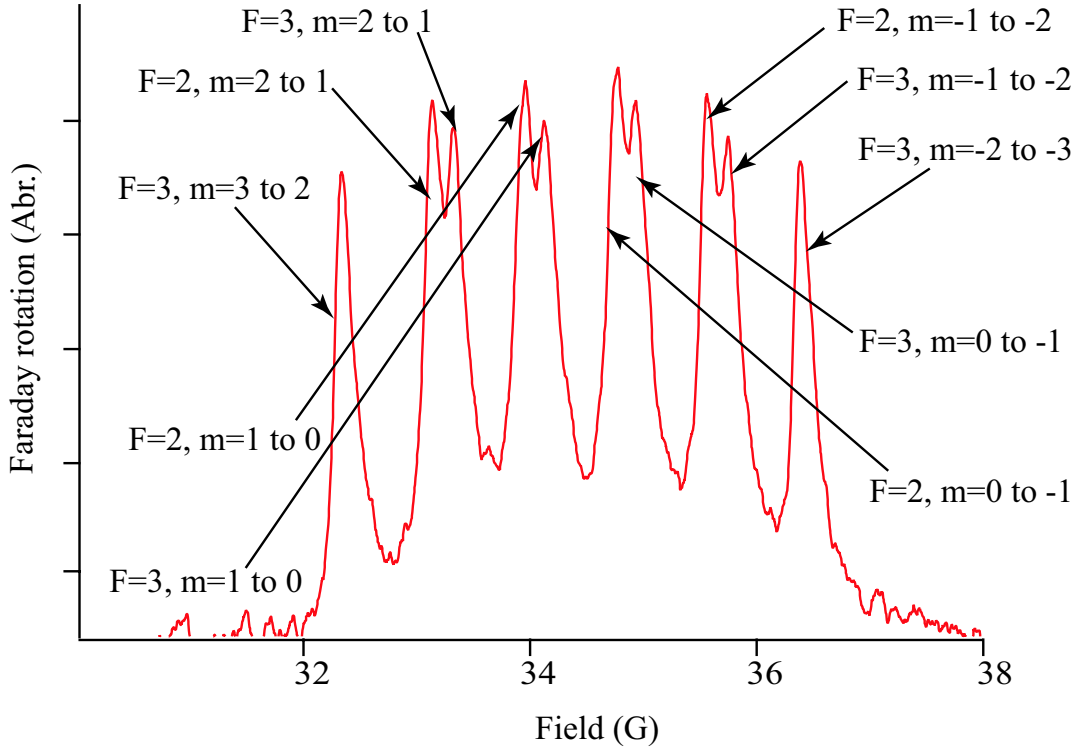

Fig. 3.6: EPR spectra of ^{85}Rb taken at low temperature and low polarization showing all of the Zeeman sublevels resolved.

In practice we must work with a field less than 60 gauss where the $F = I - J = 2, m_f = -2 \rightarrow -1$ and $F = I + J = 3$, $m_f = -2 \rightarrow -1$ resonances are nearly degenerate. In addition, spin-exchange broadening of these resonances [Appelt99] under common optical pumping conditions makes these resonances unresolvable. Thus we resolve equation 3.11 for the area of the ratio of the $F = 3, m_f = -3 \rightarrow -2$ peak to the combined area of the $F = 2, m_f = -2 \rightarrow -1$ and $F = 3, m_f = -2 \rightarrow -1$ resonances.

In this case, the resulting alkali-metal polarization for an $I = 5/2$ alkali is

$$P_{I=5/2} = \frac{7A-3}{7A+3}. \tag{3.13}$$

Examples of such spectra under optical pumping conditions are given in figure 3.8

If we do the same analysis for $I = 3/2$ alkali-metal isotopes such as ^{87}Rb, ^{39}K, ^{41}K, and ^{23}Na, the polarization in the resolved hyperfine level case is

$$P_{I=3/2} = \frac{3A-2}{3A+2}, \tag{3.14}$$

where A is the ratio of the area of the $F = 2, m_f = -2 \rightarrow -1$ to the $F = 2, m_f = -1 \rightarrow 0$ resonances. The corresponding, experimentally more common unresolved case is given by,

$$P_{I=3/2} = \frac{2A-1}{2A+1}, \tag{3.15}$$

where A is the ratio of the area of the $F = 2, m_f = -2 \rightarrow -1$ to the combined area of the $F = 2, m_f = -1 \rightarrow 0$ and $F = 1, m_f = -1 \rightarrow 0$ resonances.

Now we will look at the static magnetic holding field B_0 required to resolve the various Zeeman resonances enough to perform alkali-metal polarimetry. At low field the Zeeman splitting goes to zero and the resonances are degenerate. Therefore we use the Breit-Rabi formula to calculate the necessary field to resolve the resonances. The energy shift, E for a resonance with given F and m at field B_0 is [Ramsey53]

$$E(F,m) = -\frac{h\delta\nu_{\text{hfs}}}{2(2I+1)} - g_I\mu_B B_0 m \pm \frac{h\delta\nu_{\text{hfs}}}{2}\left(1 + \frac{4m}{2I+1}x + x^2\right)^{1/2}, \tag{3.16}$$

where F is the total spin quantum number, m is the projection of F along the quantization axis, and x is given by

$$x = \frac{(g_J + g'_I)\mu_B B_0}{h\delta\nu_{\text{hfs}}} \tag{3.17}$$

where $h\delta\nu_{\text{hfs}} = \Delta E$ is the energy of the hyperfine splitting of the particular alkali-metal isotope and $(g_J + g'_I) \simeq g_S$ for ground state alkali-metal atoms ($g'_I \ll g_s$). The $\pm$

corresponds to the $F = I \pm J$ hyperfine levels. Expanding 3.16 to third order in terms of x we obtain,

$$\begin{aligned} E(F,m) &= -\frac{h\delta\nu_{\rm hfs}}{2(2I+1)} - g_I'\mu_B B_0 m \pm \\ \frac{h\delta\nu_{\rm hfs}}{2}\Bigg[1 &+ \frac{x}{2}\frac{4m}{(2I+1)} + x^2\left(1 - \frac{4m^2}{(2I+1)^2}\right) - 6x^3\left(\frac{m}{(2I+1)} - \frac{4m^3}{(2I+1)^3}\right)\Bigg]. \end{aligned} \tag{3.18}$$

Here we have included the third order term because it becomes important if one is trying to determine the EPR frequency of K at most of the fields we use because of the small $\delta\nu_{hfs}$ for K. For the other alkali-metals the 2^{nd} order term would be sufficient. The resonance frequency between two Zeeman sublevels, $F, m \leftrightarrow F, m-1$ is approximately,

$$|\nu| = \frac{|E(F,m) - E(F,m-1)|}{h} \approx \frac{\nu_0}{2I+1} + \frac{\nu_0^2}{(2I+1)^2}\left[\frac{1-2m}{\delta\nu_{\rm hfs}}\right] \pm \frac{g_I}{g_J}\nu_0 \tag{3.19}$$

where

$$\nu_0 = \frac{g_J\mu_B B_0}{h}. \tag{3.20}$$

Using the above relation, we can make a quick approximation of the splitting between adjacent transitions to be

$$|\nu|_{F,m\leftrightarrow m-1} - |\nu|_{F,m-1\leftrightarrow m-2} = \frac{2\nu_0^2}{\delta\nu_{\rm hfs}(2I+1)^2}. \tag{3.21}$$

If we assume a width of about 50 kHz at a typical Rb SEOP temperature of $170°C$ approximately 25 gauss would be required to give 100 kHz of separation for the ^{85}Rb transitions. Since the linewidth is normally further broadened by spin-exchange, under experimental conditions higher fields may be needed. In practice we often operate near the maximum field of our apparatus from 34 to 50 gauss. In HySEOP cells the spectrum can be further complicated by the different Zeeman splittings of multiple isotopes with

the same nuclear spin, I. A full discussion of the spectra obtained in these instances is given in section 6.2. For K-Rb HySEOP cells we often choose to observe the spectra of ^{39}K because the smaller $\delta\nu_{\rm hfs}$ gives much higher resolution at a given field.

Another unique property of EPR spectroscopy in a mixture of alkali-metals again takes advantage of the properties of spin temperature. In spin temperature, the polarizations of each of the individual alkali species are in equilibrium, thus exciting a rf transition in the either the Rb or K atoms will cause a change in polarization in both. Therefore, the K and Rb spectra are simultaneously observed by tuning the probe near resonance for either alkali and sweeping though the Zeeman transitions of both. Since the amplitude of the EPR signal is proportional to the alkali density the best signal to noise is achieved by tuning the probe laser next to the resonance of the of the more abundant alkali (D_2 for Rb, D_2, or D_1 for K). In practice any of the resonances provide more than adequate signal to noise in all the cells except for the $\mathcal{D} = 500$ cell for which we had to tune the probe to one of the K lines because the typical Rb densities in this cell under optical pumping conditions where [Rb] $< 1\text{x}10^{12}$, which is just at the resolution limit of our EPR detection. Additionally, under most conditions this method also allows us to use a diode laser at the commonly available Rb wavelengths to probe the EPR spectra of alkali-metals whose wavelengths are otherwise difficult to access with a diode laser such as Na at 589 nm.

To measure the alkali-metal polarization we set the oven to the desired temperature, tune the pump beam to resonance (often by observing the maximum value of the faraday rotation of our probe beam), and de-tune the probe beam such that it is not significantly absorbed by the vapor in the cell usually, 1.5 to 2.5 nm. In the example given we fixed the rf frequency at 16 MHz and amplitude modulate it at 2 kHz. The magnetic field is then swept across the Zeeman resonances. The detector signal is sent to a lock-in amplifier and mixed with the modulation reference frequency. The output

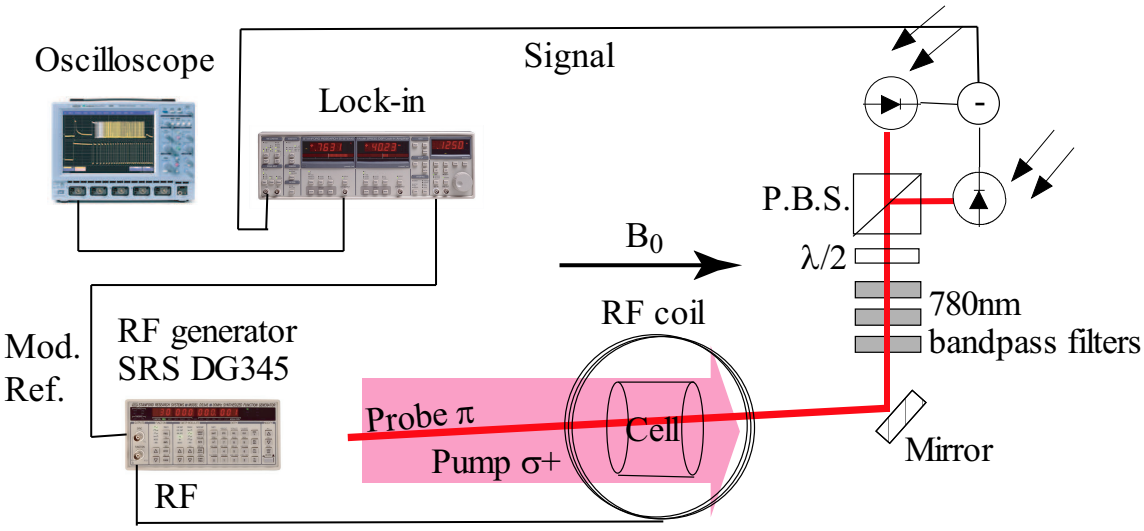

Fig. 3.7: Diagram of our EPR setup showing optical and electronic components.

is sent to the oscilloscope, averaged, and recorded. Figure 3.7 shows the experimental setup. Figure 3.6 shows a ^{85}Rb EPR spectra taken at low temperature, 120°C, and very low polarization in order to observe and resolve all of the Zeeman resonances, and Figure 3.8 shows the ^{85}Rb EPR spectra at 180°C for various pump laser spectral profiles.

3.5.2 Density Measurements

In order to make accurate measurements of SEOP, one must have accurate alkali-metal density measurements. We have developed three methods to measure the alkali-metal density. Two are based on the absolute value of the Faraday rotation of our probe beam [Kadlecek00, Vliegen01, Wu86]. The third, on the absorption of the $5s \rightarrow 6p$ transitions in Rb. All three methods give self consistent verification of the Rb under the respective conditions of the measurement. The following sub section describe each of these measurements in detail.

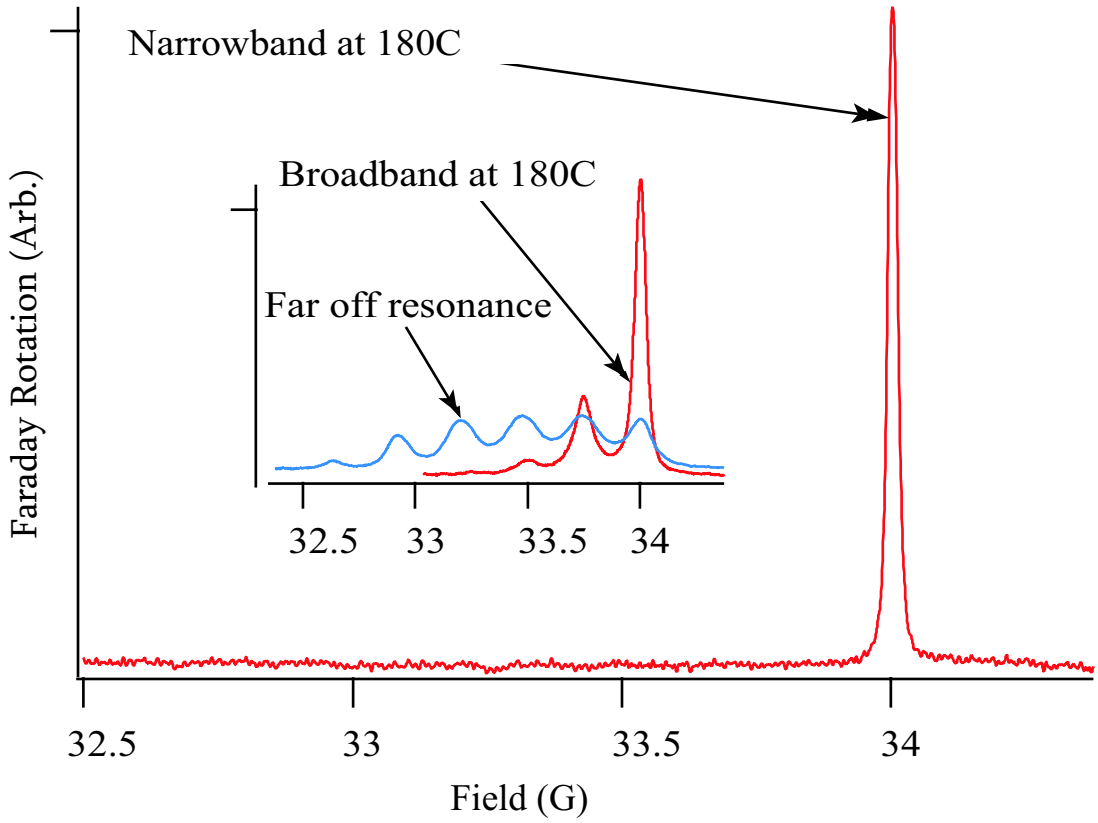

Fig. 3.8: Example of typical EPR spectra of ^{85}Rb taken under optical pumping conditions. Under most experimental conditions, using our FNDAB, only the $m_f = -F \leftrightarrow -F+1$ peak is observable

3.5.2.1 Polarization Faraday Rotation

The Faraday rotation angle for probe detuning much greater than the atomic linewidth and hyperfine structure, at constant magnetic field, and alkali polarization, P, is given by [Kadlecek00, Vliegen01, Chann02a]

$$\theta_P = \frac{[\mathrm{A}]le^2}{6mc}\left(\frac{1}{\Delta_{3/2}} - \frac{1}{\Delta_{1/2}}\right)P. \tag{3.22}$$

Here l is the length of the cell where the probe beam is passing through it, e is the electron charge, m the electron mass and c the speed of light. The notation $\Delta_J = \nu - \nu_J$ denotes the probe detuning from the $nS_{1/2} \rightarrow nP_J$ transition, and [A] is

the alkali density.

To measure the alkali density we send a linearly polarized probe beam, power $<$ 1 mW, tuned a few nm away from the alkali-metal D_2 line, ie the $nS_{1/2} \rightarrow nP_{3/2}$ transition, through the center of our cell. The probe detuning is measured is measured with a New Focus Inc. 7711 Fizzeau wave meter. The probe then passes through several bandpass interference filters to remove all possible light contamination from the 795 nm pump light and into our detector 3.9. Our detector consists of a $\lambda/2$ plate mounted in a precision rotation mount, a polarizing beam splitter cube and a subtracting photodiode pair. In some instances, with extremely high alkali densities on the order of $1 \times 10^{15}\text{cm}^{-3}$, the measured rotations can be much greater than 100 degrees. Therefore we developed a following procedure to measure these large rotations.

The absolute rotation Faraday angle created by the alkali polarization is measured by rotating the $\lambda/2$ plate to hold the detector signal at 0 while slowly changing the polarization of the pump beam, and thus the alkali atoms, from $\sigma+$ to $\sigma-$ or vise versa. This is done by rotating the $\lambda/4$ plate used to circularly polarize the pump laser by 90°. The total change in rotation from this procedure is $2d\theta_\text{P}$. The difference of the corresponding start and end values of the rotation angle of the $\lambda/2$ plate are taken and given the alkali polarization which is measured independently (and is normally 1 under intense pumping conditions) we can then calculate the alkali density. We note here that when a the atoms rotate the probe beam by θ the corresponding rotation of the $\lambda/2$ plate to re-zero the detector signal will be only $\theta/2$, therefore all $\lambda/2$ plate rotations must be multiplied by 2 to get the absolute rotations caused by the atoms. We also note one must be careful to insure that the temperature of the SEOP cell has time to stabilize after the polarization is reversed due to the large temporary increase of absorption of the pump light as its circular polarization passes through zero. The apparatus used to measure the polarization Faraday rotation is shown in figure 3.9. For

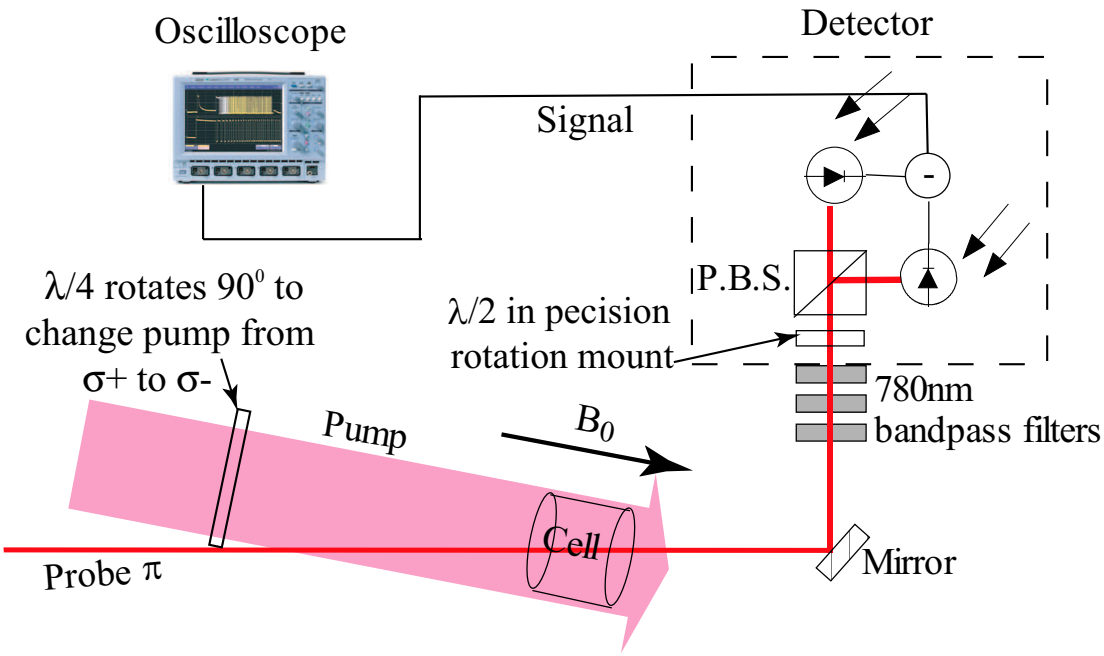

Fig. 3.9: Optical setup for measurement of the polarization Faraday rotation

the case of a K-Rb HySEOP cell, since the cell contains a mixture of Rb and K vapor where the Rb D_1 and D_2 transitions are at 795 nm and 780.2 nm and the K D_1 and D_2 transitions are at 766.7 nm and 770.1 nm respectively, it is necessary to add the contributions from both in order to get an accurate density measurement. The total polarization-Faraday rotation for the K-Rb case then becomes

$$\theta_P = \frac{le^2}{6mc}\left[[\mathrm{K}]\left(\frac{1}{\Delta_{3/2_\mathrm{K}}} - \frac{1}{\Delta_{1/2_\mathrm{K}}}\right) + [\mathrm{Rb}]\left(\frac{1}{\Delta_{3/2_\mathrm{Rb}}} - \frac{1}{\Delta_{1/2_\mathrm{Rb}}}\right)\right] P_\mathrm{A}. \tag{3.23}$$

Where the Rb and K subscripts denote the probe detunings from the respective K or Rb resonances and [Rb] and [K] are the densities of each species. Therefore we take measurements of the Faraday rotation for typically four or five probe detunings around each of the K D_1 and D_2 resonances and the Rb D_2 resonance.

The necessary wavelengths ranging from 764 nm to 782 nm were produced using a single mode 780 nm diode laser tuned using temperature control and a Littrow configured external cavity. The wavelength of a typical diode laser at 780 nm has

a temperature coefficient of 2.5nm/10° C. Thus a 780 nm laser can be tuned to 770 nm by changing the temperature from $20°C$ to $-20°C$. In addition we can tune the wavelength and additional ±5 nm or more by adjusting the diffraction angle of the grating in the Littrow cavity.

For measurements with probe detunings near the K resonances the Rb D_2 bandpass filters were replaced with two 770 nm bandpass filters. The data, shown in figure 3.10 was fit to the above equation which represents the data very well.

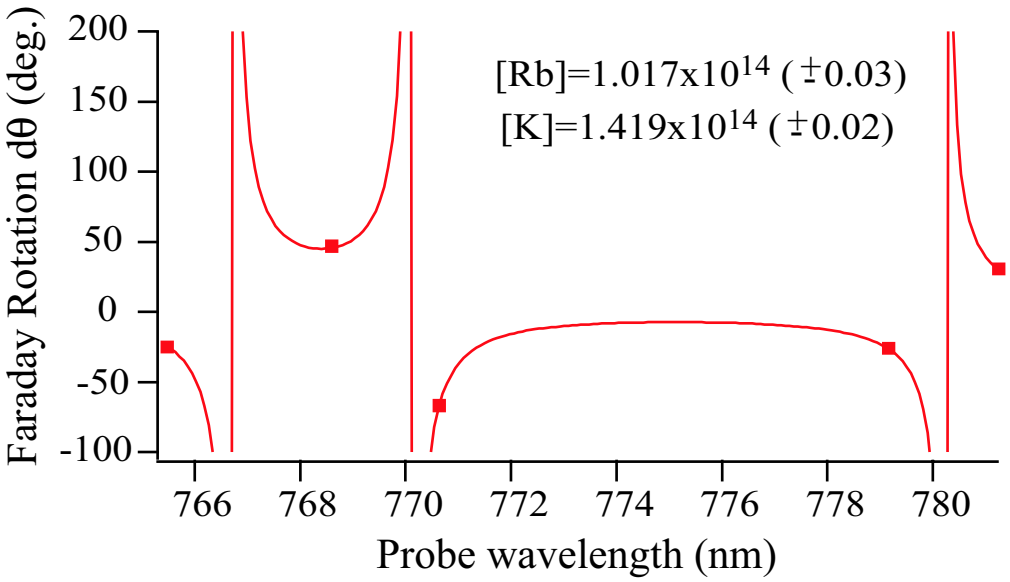

Fig. 3.10: Polarization Faraday rotation as a function of probe wavelength for a K-Rb Hy-SEOP cell. The squares represent the data points; the solid line represents the data fit to equation 3.23. The probe wavelength was measured with a calibrated Fizzeau wave meter (New Focus Inc. model 7711) to a precision of 0.001 nm.

3.5.2.2 Field Faraday Rotation

The full Faraday rotation created by an alkali-metal vapor actually has two components, the alkali-metal polarization dependent term, and a magnetic field dependant term

which is given by [Kadlecek00, Vliegen01, Chann02a]

$$\theta_B = [\mathrm{Rb}]\frac{le^2\mu_B B}{18mhc}\left(\frac{4}{\Delta_{1/2}}^2 + \frac{7}{\Delta_{3/2}^2} - \frac{2}{\Delta_{1/2}\Delta_{3/2}}\right). \tag{3.24}$$

Since this portion of the Faraday rotation is dependant on the inverse of the probe detuning squared, as opposed to the inverse probe detuning dependence of the polarization dependant term, its amplitude is much smaller, on the order of 10^{-3} deg for the (<60 gauss) magnetic fields attainable in our setup.

Due to the small signal for this measurement we use a photoelastic modulator (PEM) and lock-in amplifier. The probe beam is now circularly polarized and passes through the PEM which basically acts as a $\lambda/2$ plate modulating at 50 kHz.

After the probe passes through the cell it enters the same Faraday rotation detector and the resulting signal is mixed with the 50 kHz reference by the Lock-in amplifier. The field is ramped from 10 to 40 gauss and the signal is recorded and averaged by a digital oscilloscope. The resulting trace is calibrated to absolute field with the analog output of a gauss meter, and the voltage amplitude of the Faraday rotation signal is calibrated to an absolute rotation by rotating the $\lambda/2$ plate a known amount. A diagram of this optical setup is shown in figure 3.11. A typical data set is shown in figure 3.12.

3.5.2.3 2^{nd} Order Resonance Absorption

For one final check of the alkali density measurements, we also performed much more time consuming measurements on the absorption of the $5s \rightarrow 6p$ transitions of Rb. There are two corresponding transitions, a $P_{3/2}$ and a $P_{1/2}$ at 420.185 nm a 421.552 nm respectively. These transitions are chosen because they have a combined oscillator strength of approximately 1% of the $5s \rightarrow 5p$ transitions at 780 nm and 795 nm [Migdalek98]. This is important because the high alkali-metal densities used would

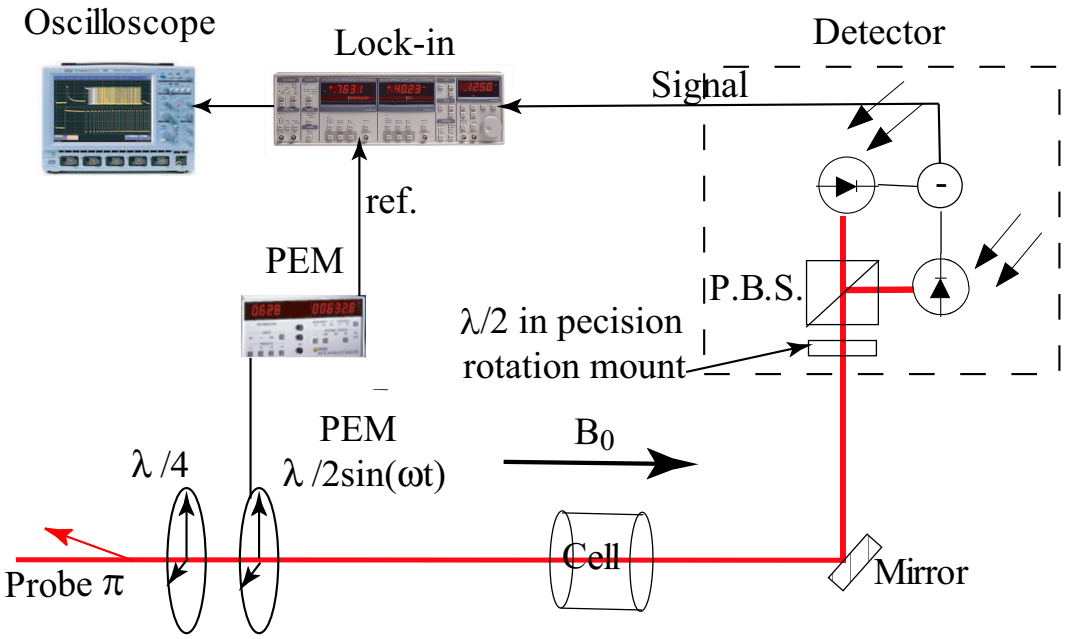

Fig. 3.11: Optical setup for field Faraday rotation using a PEM.

make the $5s \rightarrow 5p$ transitions around 100 optical depth thick, so the lower oscillator strength of the $5s \rightarrow 6p$ transitions allows the probe light to transmit enough even on resonance to perform accurate absorption spectroscopy.

The intensity of light that will be transmitted is given by,

$$I_t = I_0 e^{-[\mathrm{Rb}]\sigma(\nu)l}, \tag{3.25}$$

where l is again the cell length and the absorption cross section, $\sigma(\nu)$, the basis of this measurement is given by [Kadlecek00, Romalis97]

$$\int_{\infty}^{\infty} \sigma(\nu) d\nu = \pi r_e f c. \tag{3.26}$$

Here f is the oscillator strength and $r_e = 2.82 \times 10^{-13}$cm is the classical electron radius. From these equations and the known oscillator strengths the alkali density can be determined. We take the oscillator strengths to be the average of the two experimental values, $4 \times 10^{-}3$ and $3.75 \times 10^{-}3$ for the $6P_{1/2}$ state and $9.37 \times 10^{-}3$ and $9.54 \times 10^{-}3$ for the $6P_{3/2}$ state [Migdalek98].

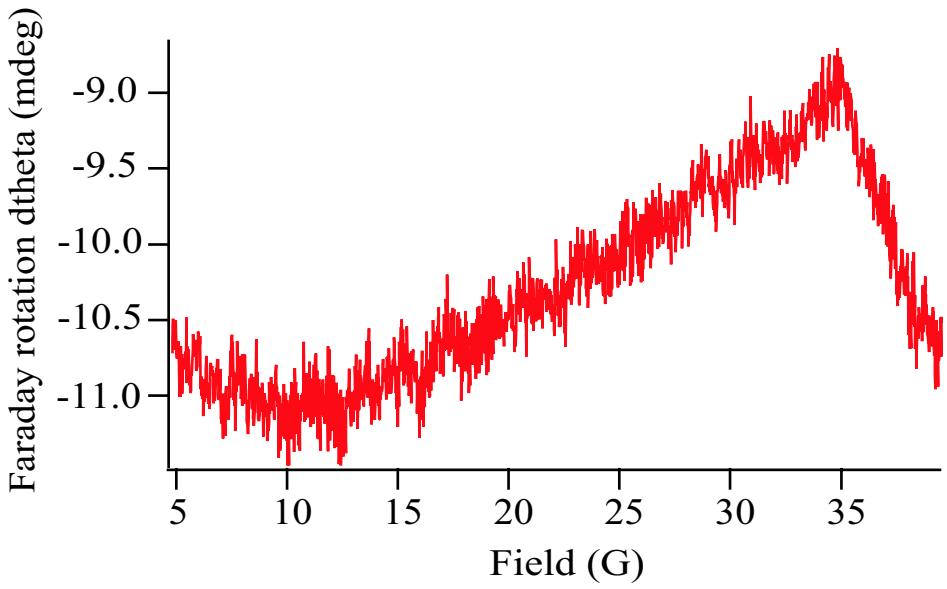

Fig. 3.12: Field Faraday rotation as a function of magnetic field for a fixed probe wavelength.

To access these resonances we frequency double a 150 mW 830 nm Sanyo laser diode (part no.DL8032-001) tuned to 840 nm by a Littrow external cavity. Using this setup we can produce several μW of light from 419-423 nm to fully resolve the resonances. The Sanyo pump laser is first narrowed and tuned with the external cavity, then focused with a 100 mm spherical lens to a waist of approximately $3 \times 7 \mu m$. A 1 cm $LiIO_3$ crystal is placed in the waist. The resulting 420 nm output is then collimated with a 100 mm cylindrical lens (oriented with its focus along the ordinary axis of the frequency doubling crystal i.e perpendicular to the polarization axis of the doubled output). Note the crystal is mounted on a precision rotation stage in order to fine tune the phase matching angle and maximize frequency doubled output. This setup is rather robust and was also developed for potential use on the $3s \rightarrow 4p$ transitions of Na by replacing the laser with a 50 mW 660nm Mitubishi diode laser (part no.ML101J8-01) and the $LiIO_3$ crystal with a 7mm BBO crystal. The oscillator strengths for the $3s \rightarrow 4p$ transitions in Na are given in [Zhang99]. A diagram of this general diode laser

frequency doubling setup is given in figure 3.13.

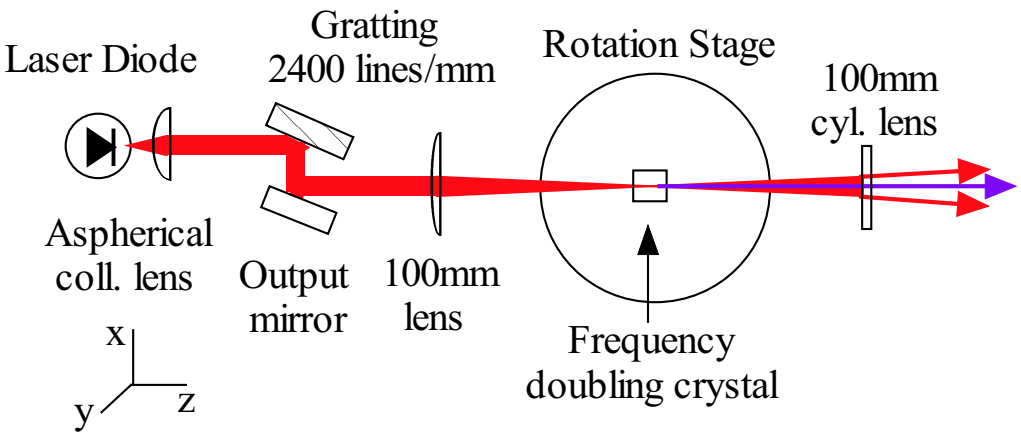

Fig. 3.13: Diode laser frequency doubling apparatus. The plane of polarization of the pump laser is in the y plane and the polarization of the doubled output is in the x plane.

The blue light was split into two beams to provide a reference power to normalize the transmission value to, and a small amount of the light is split off before the 100 mm cylindrical lens and the red light is used to measure the wavelength of the light with a wavemeter. For both the reference intensity, and transmission signal beams, the blue light was spatially separated from any remaining red pump light by a prism, then passed through a narrowband interference filter (CVI #F10-420-0-4-0.4) and is finally detected by blue light sensitive photodiodes (Hamamatsu G1893). The red light was allowed to propagate with the blue to aid in alignment. To further aid the S/N the blue light was chopped with an optical chopper to measure the transmission and reference amplitudes. A diagram of the optical setup is given in figure 3.14

The resulting transmission spectra are the fitted to determine the areas under both peaks. Using the known oscillator strengths we then calculated the Rb density. Figure 3.15 shows a sample of the data. Using this method we were able to determine the Rb density to 15% accuracy.

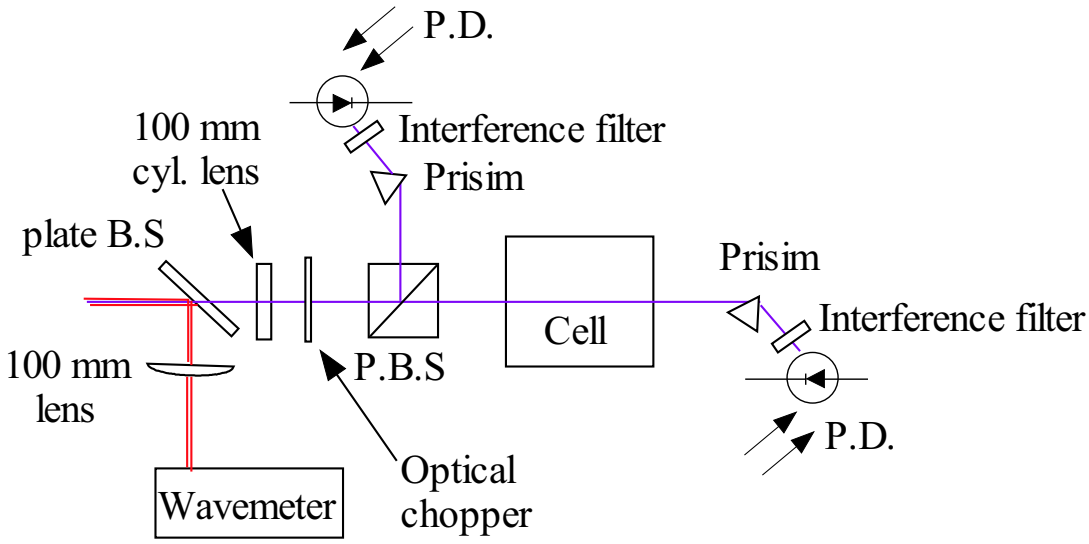

Fig. 3.14: Optical setup for measuring the absorption of the $5s \rightarrow 6p$ transitions of Rb.

3.5.3 Alkali-Metal Spin-relaxation

The alkali-metal relaxation is done using the "relaxation in the dark method" [Franzen59]. This is done by turning down the pump laser intensity and tuning it several nm off resonance to insure the alkali polarization is low, on the order of a few percent or less. For this method we place either an optical chopper or a shutter near the fucus of our pump laser collimation optics. The pump is then chopped at $\sim$ 1 Hz and the exponential decay rate of the Faraday rotation signal of our probe beam is recorded and analyzed. The observed relaxation rates are "slowed down" by a factor of s with respect to the real relaxation rates because of the spin exchange between the alkali-metal electron and nuclear spins. The resulting actual alkali-metal relaxation rate, Γ_A is given by $\Gamma_A = s\gamma$ where γ is the observed relaxation rate and s is the nuclear slowing down factor [Chann02b]. The slowing down factor for natural abundance Rb is 10.8 and 6 for $I = 3/2$ nuclei (see appendix B).

We also measure the spin relaxation simultaneously with the repolarization signal described next by simply measuring the rate of gain of the alkali-metal polarization

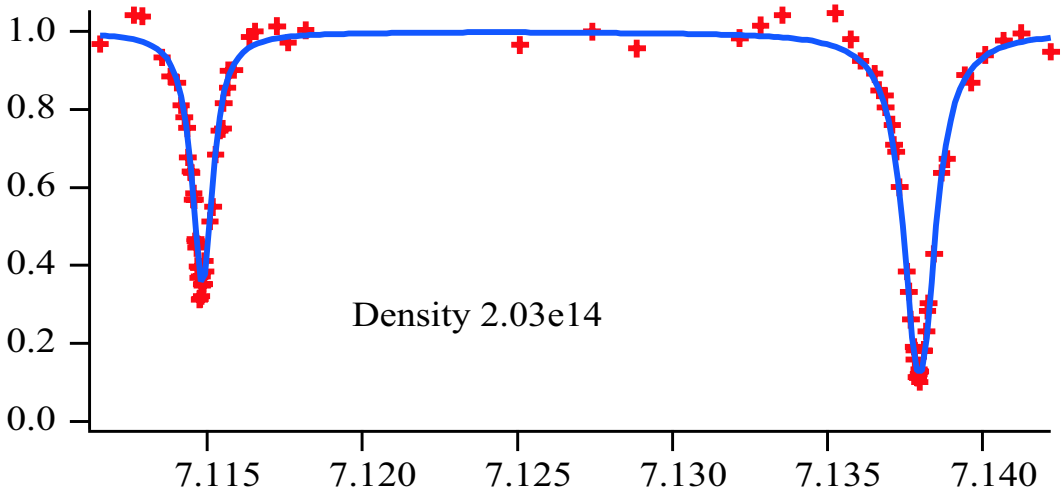

Fig. 3.15: Sample absorption spectrum of the two $5s \rightarrow 6p$ transitions of Rb with fit.

due to spin-exchange with the polarized ^{3}He in the absence of optical pumping. The two methods agree to a few percent. A sample of the repolarization method to measure the alkali-metal relaxation rate is shown in figure 3.17.

3.5.4 Alkali-Metal repolarization

As stated above the alkali-metal "repolarization" refers to the polarization created in the alkali-metal vapor through spin-exchange collisions with polarized ^{3}He in the absence of optical pumping. The amplitude of this signal is governed mainly by the total spin-exchange efficiency of the particular alkali-metal or combination of alkali-metals used and the polarization of the ^{3}He. Thus for the case of a pure Rb vapor this limits the maximum repolarization signal to less than 2%.

To measure the absolute value of this repolarization of the alkali-metal, we "chop" the alkali-metal polarization using a strong rf pulse at the alkali-metal EPR resonance to strongly saturate and depolarize the alkali-metal. The magnetic holding field is kept low, $\sim$ 6 gauss, in order to insure the EPR resonances are nearly degenerate, thus allowing the rf to fully depolarize the alkali-metal electrons. The amplitude of

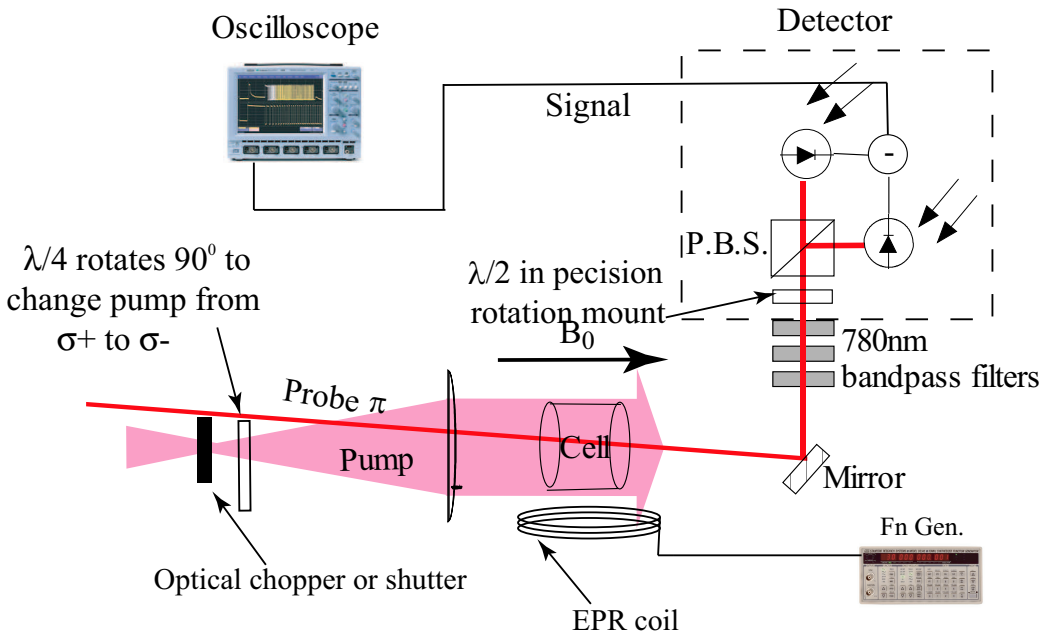

Fig. 3.16: Setup for measuring alkali-metal relaxation rates. To use the "chopper" method the pump is detuned so that the alkali polarization $< 5\%$. Either a shutter or a chopper suitable to operate at ~ 1 Hz is placed near the focus of our pump laser collimation optics. For the rf method, the pump is blocked, and the alkali-metal is relaxed by a strong, resonant, 1 Hz square wave, amplitude modulated, rf.

this signal is calibrated to an absolute Faraday rotation angle by again moving the $\lambda/2$ plate on the Faraday rotation analyzer by an known amount, usually one degree or less, and taking the ratio of the resulting angular amplitude to that of the fully polarized sample obtained during the alkali-metal density measurement for the same probe detuning. The PEM can be used to increase the S/N but often is not needed. Thus the experimental setup for this measurement is the same as that for the alkali-metal relaxation with the addition of the chopping rf source. We used the same rf coil as was used for the alkali-metal polarimetry. For the EPR frequency at the 6 gauss holding field required for this measurement, this coil is driven by the either the SRS DG345 or Tektronix CFG253 function generator. A sample repolarization trace which

was used to measure both the repolarization amplitude and alkali-metal relaxation rate is shown in figure 3.17.

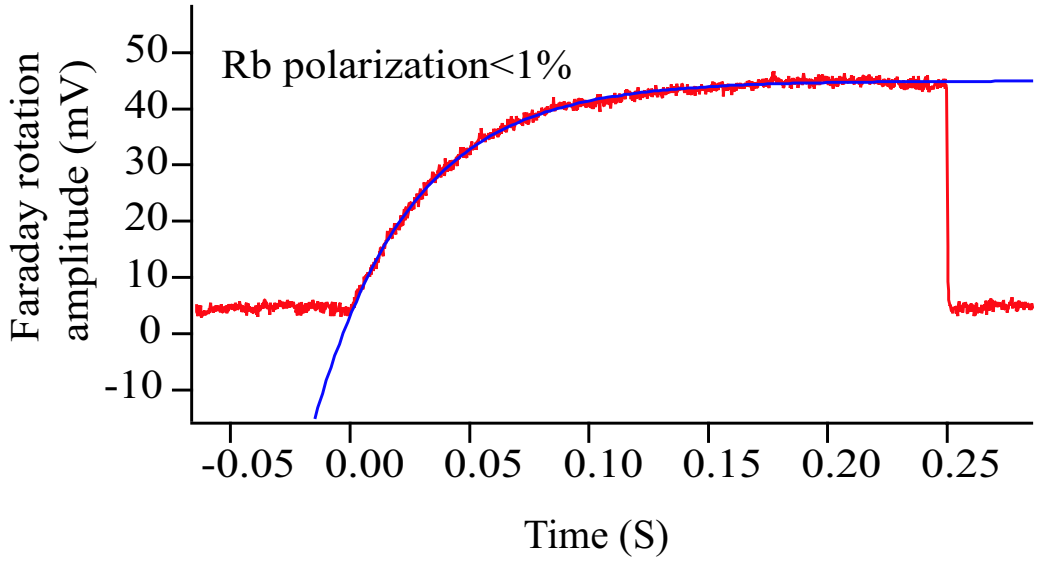

Fig. 3.17: Sample of repolarization data showing exponential fit to determine the alkali-metal relaxation rate.

3.6 ^{3}He Polarimetry

3.6.1 Relative ^{3}He Polarimetry using FID NMR

We use Free Induction Decay (FID) to monitor the relative change in P_{He} as a function of time. Our FID system is controlled and automated by a computer with a LabView Daq card and program. The computer synthesizes a pulse at the ^{3}He NMR resonance frequency (3.24 kHz/gauss) and sends it through an external signal conditioning circuit which drives a 300 turn, 34 gauge, 2 cm diameter coil placed under the SEOP cell. This pulse gives a small "tip," in the plane perpendicular to the magnetic holding field, to the nuclear spin of a small number of ^{3}He atoms directly over the coil. The tipped ^{3}He atoms then begin to precess around the magnetic holding field at the NMR frequency

for the particular field and de-phase with a time constant T_2. T_2 in our apparatus is normally on the order of 100 ms or more and dominated by field gradients and diffusion. The resulting oscillating magnetization created by the ^{3}He atoms is then sensed by the same coil, pre-amplified by our signal conditioning circuit, and sent to a lock-in amplifier which is referenced to the ^{3}He NMR frequency with an offset of 100 Hz. The offset is adjusted by tuning the internal reference frequency of the lock-in amplifier until a desirable signal is obtained. The output of the lock-in is then sent back to LabView where it is recorded. An example data set is shown in figure 3.19. A diagram of the NMR FID signal acquisition system is shown in figure 3.18.

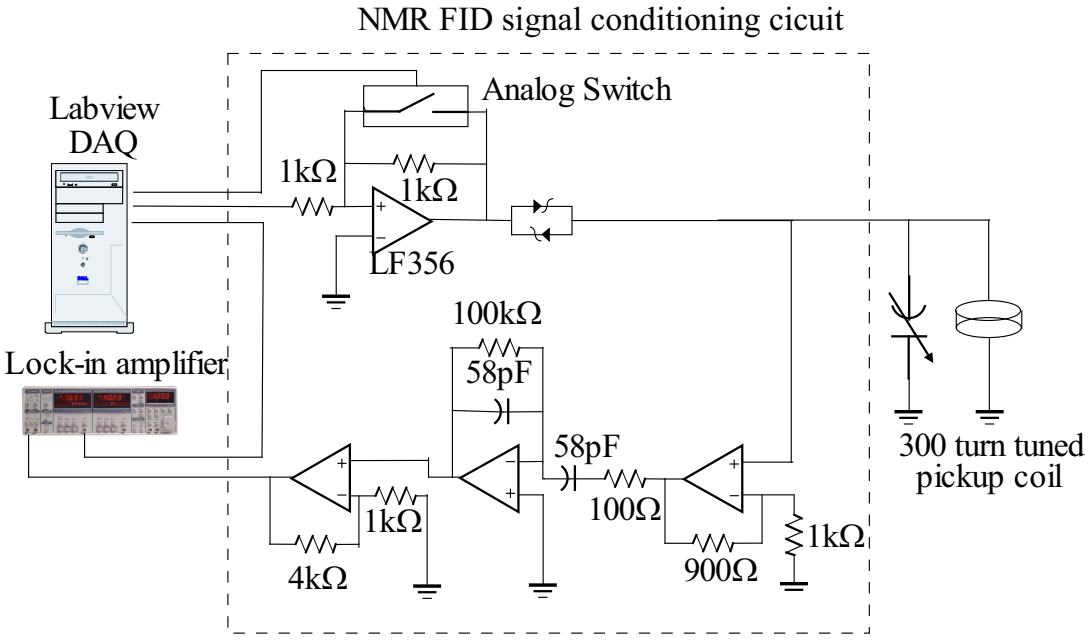

Fig. 3.18: Diagram of the NMR FID setup showing the FID signal conditioning circuit.

The transverse magnetization of the polarized ^{3}He atoms is given by [Abragam61]

$$M = M_z \sin\theta e^{-t/T_2} \tag{3.27}$$

where θ is the tip angle. This magnetization induces a voltage, V, in the pickup coil

given by

$$V_{atoms} = QE \tag{3.28}$$

where Q is the quality factor of our coil (typically around 100) and E is the emf in the coil from the precessing ^{3}He magnetic moments which is given by Faraday's law as,

$$E = \omega M_z n A \sin\theta e^{-t/T_2}, \tag{3.29}$$

where $\omega = 3.24 kHz/gauss$ is the ^{3}He Larmor precession (or NMR) frequency, A is the area of the pickup coil, and n the number of turns.

The lock-in amplifier (SRS 830) multiplies the signal,

$$V_{atoms} \sin(\omega t + \phi), \tag{3.30}$$

by the lock-in reference signal,

$$V_{ref} = \sin(\omega_{ref} t + \phi_{ref}). \tag{3.31}$$

The resulting output is then low pas filtered to give,

$$V_{out} = 1/2 V_{atoms} V_{ref} \sin((\omega - \omega_{ref})t + (\phi - \phi_{ref}))e^{-t/T_2} * G(\omega - \omega_{ref}), \tag{3.32}$$

where $\omega - \omega_{ref} = \Delta\omega$ is the offset of the lock-in amplifier reference frequency from the NMR frequency of the ^{3}He. We normally operate at an NMR frequency of 18 to 27 kHz with a $\Delta\omega$ of $\sim 100 Hz$. $G(\Delta\omega)$ is the "roll off" or frequency offset dependance of the lock-in amplifier gain as a function of offset frequency, a value which we measured.

Therefore the data recorded by LabView is fit to the equation

$$V(t) = G(\Delta\omega) V \sin(\Delta\omega t + \Delta\phi) e^{-t/T_2}, \tag{3.33}$$

with four fit parameters, V which is the amplitude of the recorded signal, $\Delta\omega$ which is the period of oscillation of the signal, $\Delta\phi$ an arbitrary phase difference between the

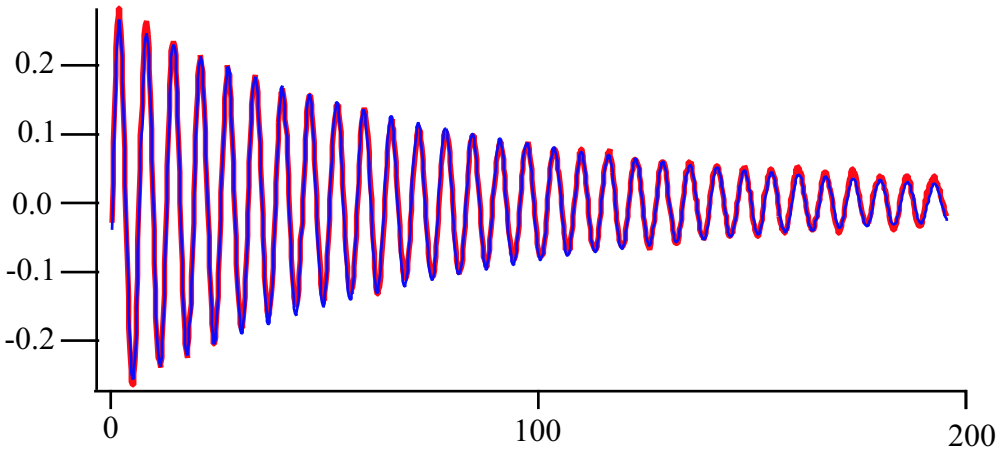

Fig. 3.19: Example NMR FID signal with fit to equation 3.33.

reference and atom signals, and T_2. Figure 3.19 shows an example of a the signal from a typical FID pulse. In order to record the rate of gain or loss of polarization by the ^{3}He our computer is programmed with LabView to automatically acquire, fit and record the FID amplitudes, V_{out}, at timed intervals, usually every 30 minutes. Exponential fits of the resulting spin-up or spin down data for a given alkali-metal density give Γ_{He}, the ^{3}He spin relaxation rate. An example data set of a typical spinup is shown in figure 3.20.

3.6.2 Absolute ^{3}He Polarimetry using Alkali-Metal EPR Frequency Shifts

Accurate absolute ^{3}He polarimetry is very crucial for studies of SEOP. There are several well established methods to accomplish this. The standard method involves calibrating the V_{out} of an NMR FID or AFP pickup coil to thermally polarized water molecules at known field ($\sim$ 1 Tesla) in a cell of the same geometry and construction as the SEOP cell being used [Romalis98]. Another method uses the absorption of a polarized neutron beam [Jones00, Heil99]. Yet another less common method involves measuring the macroscopic magnetic field produced by the P_{He} with a sensitive magnetometer placed

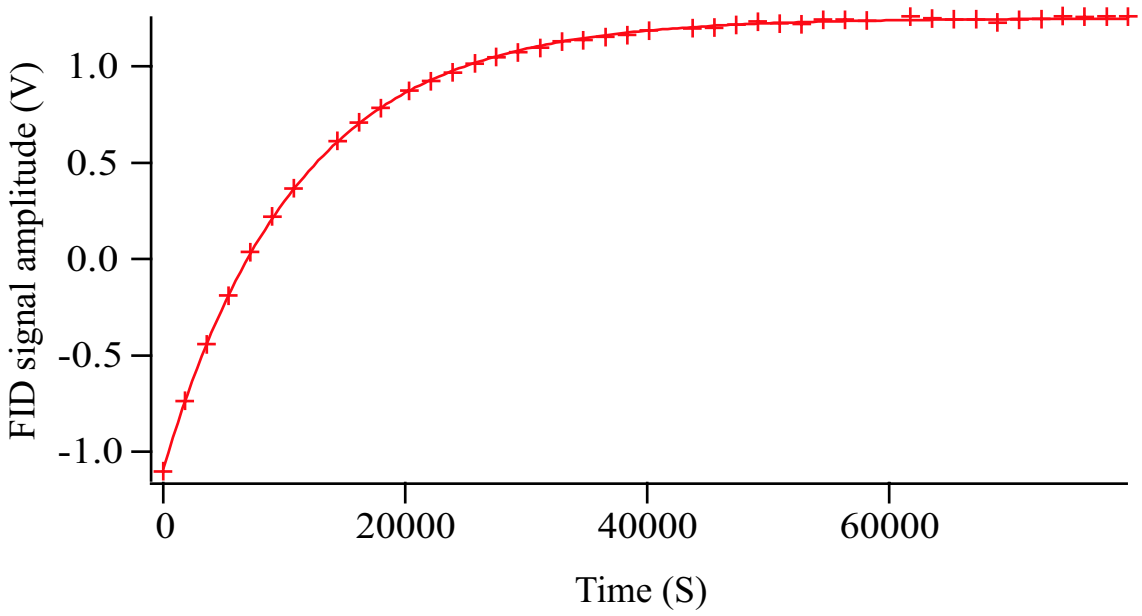

Fig. 3.20: Example of a ^{3}He spin up, showing the gain in P_{He} as a function of time. The transients can begin from 0 polarization or negative polarization as in this example. For spin downs the pump laser is turned off and the data starts from P_{He} and goes to 0.

next to the cell [Wilms97]. The final method which has become very well established due to its experimentally robust nature, measures the frequency shift in the alkali-metal EPR resonance due to the interaction with the polarized ^{3}He nuclei [Scheafer89, Newbury93, Barton94, Romalis98]. These EPR frequency shifts are proportional to [He], P_{He} and an enhancement factor κ_0 which has been measured very accurately by Romalis et al. [Romalis98] for Rb-^{3}He and for K-^{3}He and Na-^{3}He in this work which is described in chapter 6 and [Babcock05].

Our procedure for measuring the EPR frequency shifts involves using a PID locking circuit, described later, to lock to the alkali-metal EPR frequency which is then recorded with a digital counter. The P_{He} is then reversed from positive to negative or vise versa by NMR adiabatic fast passage (AFP) while the lock follows the change in the EPR

frequency. Figure 3.25 shows a diagram of the apparatus to measure the EPR frequency shifts. The following subsections describe the derivation of κ, the fundamentals of AFP, and a detailed description of the experimental procedure used to measure P_{He} with the EPR frequency shifts.

3.6.2.1 EPR Frequency Shift Enhancement Factor

The EPR shift is largely caused by the Fermi-contact interaction $\alpha\mathbf{K}\cdot\mathbf{S}$ between the nuclear spin $\mathbf{K}$ of the noble gas nucleus of magnetic moment μ_K and the electron spin $\mathbf{S}$ of the alkali atom. The measured shift is therefore qualitatively similar to the expected Zeeman interaction with the field produced by the bulk ^{3}He nuclear magnetism, but is larger by an enhancement factor, termed κ_0. Given that the enhancement arises from alkali-metal electron-^{3}He nuclear overlap during binary collisions, it is not surprising that κ_0 is different for each alkali partner, and is slightly temperature dependent [Scheafer89]. Thus we begin our analysis of the EPR frequency shifts by reviewing the Zeeman frequency between $F, m \rightarrow F, m-1$ states given by the Breit-Rabi formula [Ramsey53] (equation 3.16) to be

$$\begin{aligned}\nu_{F,m\rightarrow m-1} &= \frac{g_I\mu_B m B_0}{h} - \frac{\Delta E x}{h(2I+1)} - \frac{\Delta E 2x^2}{h(2I+1)^2}(2m-1) \\ &\quad +\Delta E 3x^3\left(-\frac{1}{(2I+1)^3}+\frac{4\left(3m^2-3m+1\right)}{(2I+1)^3}\right) \qquad (3.34)\end{aligned}$$

where $\Delta E = h\delta\nu_{hfs}$ and the terms in the second line are from the third order term in the expansion of the Breit-Rabi formula. We note that for $g_J \approx g_S \gg g_I$, and that $x = g_S\mu_B B_0/\Delta E$. Now to see how this frequency will change due to the change of magnetic field created by the ^{3}He polarization we take the derivative of equation 3.34 with respect to field to get,

$$\Delta\nu_{F,m\rightarrow m-1} = -\frac{g_S\mu_B}{h(2I+1)}\Delta B - \frac{g_S\mu_B}{h^2\delta\nu_{hfs}(2I+1)^2}(2m-1)2B\Delta B$$

$$+\frac{g_S^2\mu_B^2}{h^3(\delta\nu_{hfs})^2}\left(\left(\frac{3m^2-3m+1}{(2I+1)^3}\right)-\frac{1}{2I+1}\right)3B^2\Delta B. \tag{3.35}$$

For alkalis with sufficiently large $\delta\nu_{hfs}$ such as ^{85}Rb for which $\delta\nu_{hfs} = 3036MHz$ and at low fields all but the second term can be neglected. (A list of atomic parameters important to SEOP are given in appendix C.) With this approximation the frequency shift caused by the polarized ^{3}He becomes

$$\Delta\nu = \frac{g_s\mu_B}{h(2I+1)}\Delta B \tag{3.36}$$

If the change in field, ΔB, is due to a spherical volume, the field inside a magnetized sphere is given by,

$$\Delta B = \frac{8\pi M}{3} \tag{3.37}$$

where the magnetization M produced by the polarized ^{3}He of density [He], polarization P_{He} and magnetic moment μ_K is

$$\Delta B = \frac{8}{3}\pi\mu_K[\mathrm{He}]P_{\mathrm{He}} \tag{3.38}$$

However since the magnetic field felt by the alkali-metal electrons is enhanced by the probability of being within the nucleus of the ^{3}He atom during binary collisions we must multiply this result by the κ_0 for a given alkali-metal species[Walker89]. Thus combining equations 3.36, 3.38 and κ_0, the resulting frequency shift caused by the polarized ^{3}He is [Romalis98]

$$\Delta\nu_0 = \frac{8\pi}{3}\frac{g_s\mu_B}{(2I+1)h}\kappa_0\mu_K[\mathrm{He}]P_{\mathrm{He}} \tag{3.39}$$

$$= (1.13\frac{\mathrm{kHz}}{\mathrm{amagat}})\kappa_0[\mathrm{He}]P_{\mathrm{He}} \tag{3.40}$$

when [He] is given in amagats.

A complete list of κ_0's with temperature coefficients is given in table 6.2. For fields higher than a few gauss and for ^{39}K ($\delta\nu_{hfs} = 462MHz$) the third order term must be included. This results in multiplying equation 3.40 by $(1+\epsilon)$ where ϵ is the magnetic moment correction factor. A graph of ϵ vs. EPR frequency is given in figure 6.2 and a full discussion of how and when to correct for a non-negligible 2^{nd} order term is given in chapter 6.

Since the relation as defined in equation 3.40 was derived assuming cells of spherical geometry, for cells of non spherical geometry an additional geometric correction factor, κ', must be included to correct for the different magnetization of the cell caused by the ^{3}He nuclei. The total effective frequency shift enhancement factor, κ_{eff} can be defined as [Romalis98]

$$\kappa_{\text{eff}} = \kappa_0 + \kappa' = \kappa_0 + \frac{3}{8\pi}C(\vec{z}) - 1, \tag{3.41}$$

here $C(\vec{z}) = B_z/M_{\text{He}}$, where $M_{\text{He}} = \mu_K[\text{He}]P_{\text{He}}$. $C(\vec{z})$ can be calculated using the method of magnetic scalar potential [Jackson]. For spherical cells $C(\vec{z}) = 8\pi/3$ and is uniform throughout the cell giving $\kappa' = 0$. If we were to consider a cell defined by an ellipsoid of revolution with the major axis along $\vec{z}$, the direction of the applied holding field, $C(\vec{z})$ remains constant throughout the cell and becomes [Skomski]

$$C(\vec{z}) = 4\pi\left[1 - \frac{1}{k^2-1}\left(\frac{k}{\sqrt{k^2-1}}\text{arcosh}(k) - 1\right)\right] \tag{3.42}$$

where $k = a/b$ is the ratio of the lengths of the semi-major to semi-minor axes. For geometries not definable as an ellipsoid, the field inside the cell is not uniform and one must average the geometric contribution along the detection volume. We did this for a probe beam passing through the middle (perpendicular to the flat windows) of a cylindrical geometry, here $C(\vec{z})$ is [Chann02a]

$$C(\vec{z}) = \frac{8\pi}{3}\left[\frac{3}{2l}\left(\sqrt{a^2+l^2} - a\right)\right] \tag{3.43}$$

For the two extremes of a very long cylinder, parallel or perpendicular to the magnetic holding field, $C(\vec{z})$ will have its maximum values of 4π and 2π respectively. The largest correction factor of any cell we used was for Oscar and Felix for which $\kappa' = 0.23$ corresponding to a correction of less than 5% in the measured P_{He}.

3.6.2.2 Adiabatic Fast Passage

The principle of adiabatic fast passage or AFP can be considered either classically or quantum mechanically. Here we will consider the classical approach [Abragam61]. Consider that the atoms experience a field that is the sum of two fields, a constant field, $\mathbf{B_0} = \hat{k}B_0$ and a field $\mathbf{B_1}$ perpendicular to $\mathbf{B_0}$ and rotating at angular velocity ω. Now consider the ^{3}He atoms in the rotating frame of $\mathbf{B_1}$. If we define the $\hat{i}$ unit vector in the rotating frame to be along $\mathbf{B_1}$, the atoms will experience an effective field given as,

$$\mathbf{B_{eff}} = \left(B_0 + \frac{\omega}{\gamma}\right)\hat{k} + B_1\hat{i}. \tag{3.44}$$

Where $\gamma = \mu_K/\hbar I$, the gyromagnetic ratio, is the constant of proportionality between the applied field, $\mathbf{B_0}$, and the Larmor precession frequency, $\omega_L = -\gamma\mathbf{B_0}$ [Ramsey53]. For ^{3}He $\gamma = 3.24$ kHz/gauss. Thus in the rotating frame the atoms only see this $\mathbf{B_{eff}}$ as if it were a static holding field and will precess around it with angular frequency $\omega_{eff} = -\gamma\mathbf{B_{eff}}$. A further discussion of how to calculate the angle θ between $\mathbf{B_{eff}}$ and $\mathbf{B_0}$ which will go from 0 to π is given in [Abragam61].

Under experimental conditions, $\mathbf{B_0}$ will be much greater than $\mathbf{B_{eff}}$ and we will define a ω_1 as $\omega_1 = -\gamma \mathrm{B}_1$. We see can from equation 3.44 that $\mathbf{B_1}$ can only significantly reorient the nuclear spins if $|\omega - \omega_L| \sim |\omega_1|$. This is a resonance phenomenon with a width on the order of ω_1 [Abragam61]. Here we quickly note that experimentally a linear oscillating sinusoidal rf field given as $2\mathrm{B}_1\cos\omega t$ is used for AFP, not a rotating

field as used in 3.44. However we can consider this field as the superposition of two fields of amplitude $\mathbf{B_1}$ rotating in opposite directions at $\pm\omega$. In the rotating frame the component rotating at $-\omega$ would create a precession at $2\omega_1$ which is off resonance by $2\omega_1$ and thus creates a negligible effect [Abragam61]. Consequently the linear oscillating rf field is well described by the rotating field in the derivation.

The adiabatic theorem basically states that as long at the rate of change of the frequency of oscillating rf, $\dot{\omega}$, is slow compared to the Larmor frequency, the magnitude of the magnetization of the atoms will remain constant and point along $\mathbf{B_{eff}}$. This is the equivalent statement to saying that the angle of $\mathbf{B_{eff}}$ created by the oscillating rf, θ, must change slowly from 0 to π compared to Larmor frequency, thus allowing the spins to follow $\mathbf{B_{eff}}$. If we begin at a frequency far above resonance and sweep to a frequency far below resonance, the magnetic moments which begin parallel to $\mathbf{B_0}$, will remain parallel to $\mathbf{B_{eff}}$ and thus end anti-parallel to $\mathbf{B_0}$ [Abragam61]. In addition to the adiabatic condition we must also add the condition that the AFP sweep must be fast compared to the rate of transverse spin relaxation in the rotating frame. Combining these two conditions we arrive at the AFP parameters given as [Romalis98],

$$\gamma B_1 \gg \frac{\dot{\omega}}{\gamma B_1} \gg D\frac{|\Delta B_z|^2}{B_1^2} \tag{3.45}$$

where D us the diffusion coefficient and ΔB_z is the field gradient of the D.C. holding field.

In order for use to comfortably satisfy the AFP conditions given in equation 3.45 it is easy to see that one wants a large value of B_1. As a result we amplify our AFP function generator (SRS DG345) with a power amplifier to create a desirable field strength. Figure 3.21 shows the circuit diagram of the amplifier we developed to help meet the power and frequency demands of our AFP procedure.

Using this power amplifier we can produce a P-P voltage on our AFP coils of

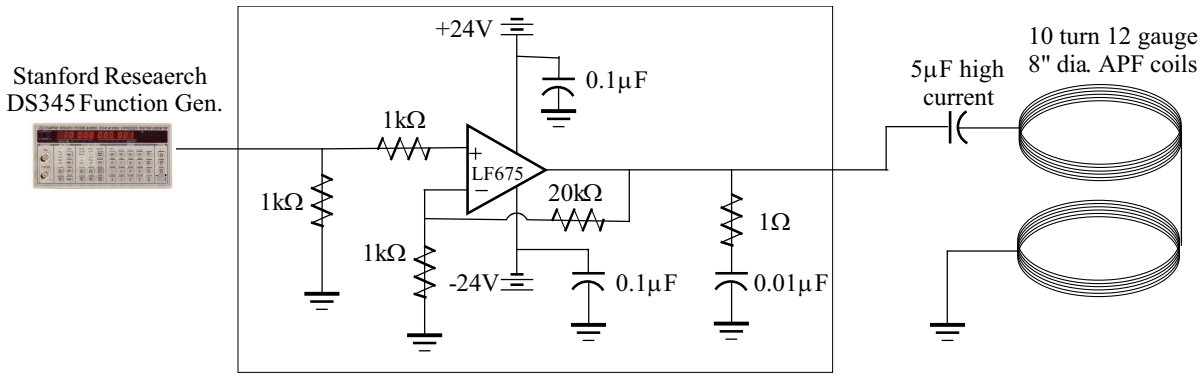

Fig. 3.21: Circuit diagram for the 30W power amplifier to drive the AFP coils.

40V and a $\mathbf{B_1}$ of 0.25 gauss and 0.4 gauss at center frequencies of 70kHz and 45kHz corresponding to a $\mathbf{B_0}$ of 22 and 14 gauss respectively. Our field gradient is on the order of 1-10mG. We generally sweep our rf frequency with a span of 28kHz at a rate of 2Hz. Thus for the 75kHz center frequency sweep, substituting these values in to equation 3.45 we obtain 810Hz $\gg$ 49Hz $\gg$ 0.001Hz. The loss of P_{He} during a typical AFP is on the order of 0.5% or less.

3.6.2.3 Experimental Procedure

In order to lock to the EPR resonance and measure the frequency shift before and after an AFP reversal of the P_{He}, we use a process very similar to that used to lock diode lasers. Assume that the resonance line shape of the voltage of the Faraday rotation signal as a function of applied rf frequency $V(\nu)$ is a Lorentzian,(see figs. 3.8, and 6.1), then if the rf field frequency modulates the signal with an amplitude A at frequency ν_m the resulting signal will be,

$$V(\nu) = V(\nu + A\sin\nu_m t) \tag{3.46}$$

This can then be expanded with a Taylor series expansion to obtain,

$$V(\nu) = \sin\nu_m t\left(A\frac{dV}{d\nu} + ...\right) + \cos 2\nu_m t\left(-\frac{A^2}{4}\frac{d^2V}{d\nu^2} + ...\right) + ... \tag{3.47}$$

When this signal is mixed with the modulation frequency by the lock-in, the signal is proportional to the derivative of the Lorentzian giving the needed dispersion like line shape. This dispersion output of the lock-in is then sent to a PID locking circuit (lock box) shown in figure 3.22. This circuit then produces an error signal that controls the central frequency of the rf and locks it to the dispersion zero crossing.

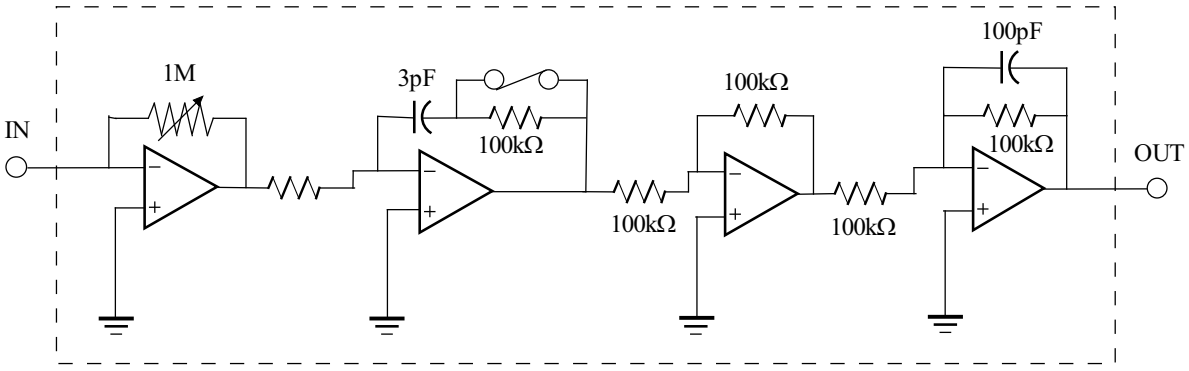

Fig. 3.22: Circuit diagram of the lock box used to lock to the EPR resonance.

The dispersion signal is produced with a home-built VCO controlled function generator to drive the rf coil. A diagram of the circuit is given in figure 3.23. This function generator has a built-in adder with independent gains on each of the two inputs. The first input accepts the modulation source which is created by the reference output of our SRS 830 lock-in amplifier. The second input accepts the PID output from the dispersion signal created by the lock box. We generally modulate at $\nu_m = 2$ kHz with an amplitude that creates a frequency amplitude of approximately $A = 5$ kHz, ie the output of the function generator is giving an output with a central frequency at the EPR frequency modulating $\pm$ 2.5 kHz at a rate of 2 kHz. It is important to note that all of the Fourier components of this modulated rf driving frequency must be much less than the Larmor precession frequency of the ^{3}He atoms for the given holding field or severe relaxation of the P_{He} will result.

The frequency of the function generator output is measured using a HP53131A

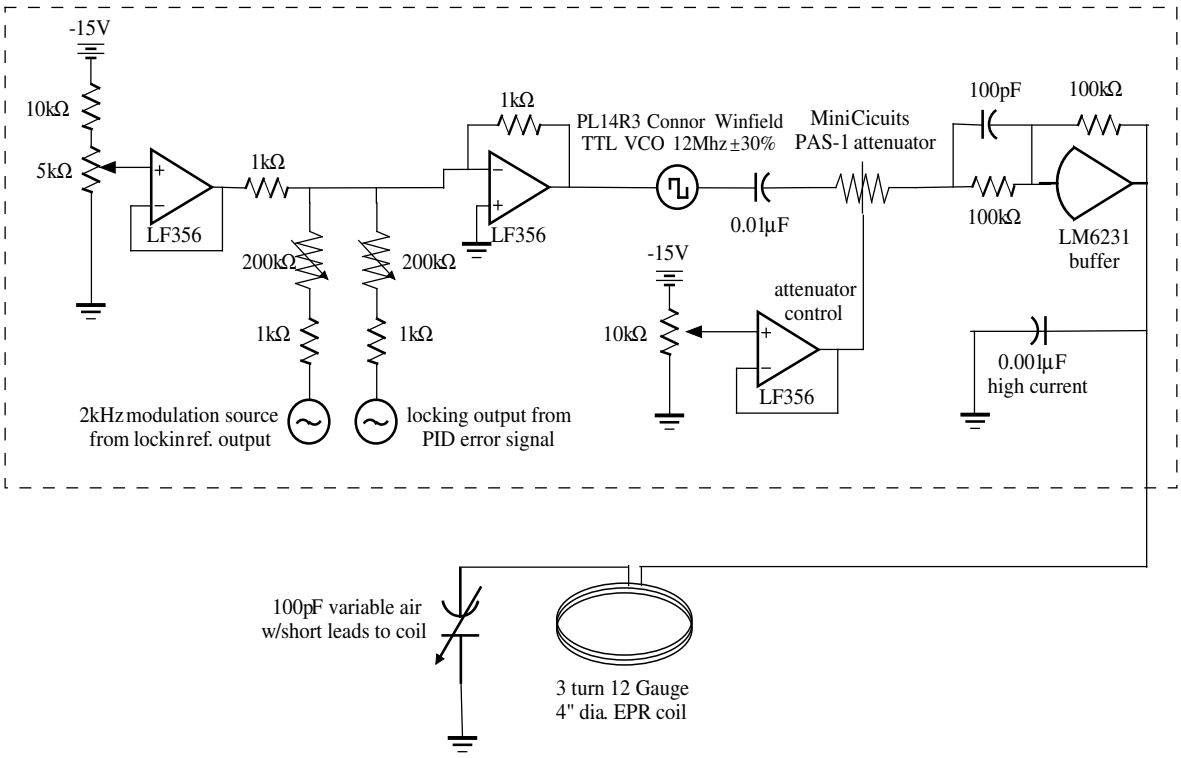

Fig. 3.23: Circuit diagram of the 9-14MHz VCO function generator used to drive the EPR coils at the necessary frequencies for our measurements. This circuit could be replaced by an adder to sum the two VCO inputs and a function generator with a VCF (voltage controlled frequency) input.

digital counter. This counter is set with an acquisition time constant of 0.3 s and therefore measures the average frequency of the frequency modulated rf. The output of the frequency counter is then sent to a computer via a GPIB interface to record the EPR frequency as a function of time. The ^{3}He spin is then reversed (from spin-up to spin-down or vice versa) by AFP, while recording the corresponding shift in the EPR frequency. Note that the total frequency shift of the monitored EPR peak is $2\Delta\nu_0$ because the ^{3}He polarization is being changed from $+P_{\rm He}$ to $-P_{\rm He}$. The magnetic field was not stabilized for the experiment. Under some circumstances there was a small loss of $< 0.5\%$ per AFP reversal that was corrected for by taking four successive

EPR spectra in rapid order, pausing between spectra for about 20 seconds to acquire frequency data and to perform AFP to reverse the ^{3}He spins. Figure 3.24 shows a typical data set. The absolute value of the difference in frequency between adjacent EPR spectra ($\Delta\nu$(N)), was taken and plotted versus the counting number of the AFP reversal, N.

The value of ν_N, the EPR frequency after the N^{th} AFP reversal, assuming a loss coefficient of ε, is given by,

$$\nu_N = -1(\nu_0(1-\varepsilon))^N \simeq -1^N\nu_0(1-N\varepsilon) \tag{3.48}$$

where ν_0 is the initial value of the EPR frequency and the term on the left side of the $\simeq$ is the first order expansion about $\varepsilon = 0$ for the remaining signal after the N^{th} AFP. The measured frequency shift is the difference between the N^{th} and the $(N-1)^{th}$ frequency. Therefore the corresponding difference in frequencies, $\nu_N - \nu_{N-1}$, from equation 3.48, is taken to give,

$$|\nu_N - \nu_{N-1}| = \Big|\Delta\nu(\mathrm{N})| = |2\Delta\nu_0\left(1-\left(\mathrm{N}-\frac{1}{2}\right)\varepsilon\right)\Big|. \tag{3.49}$$

The frequency difference data is then fit to this function to extrapolate the value of $\Delta\nu_0$. We note that the AFP loss coefficient ε determined from the EPR spectra was in agreement with NMR FID data taken directly before and after the spectra. The resulting value of $\Delta\nu_0$ is then used to calculate P_{He} using the measured temperature to calculate κ_0, and the measured [He] using equation 3.40.

3.7 N_2 and ^{3}He Gas Density Measurements

Traditionally the ^{3}He and N_2 pressures in SEOP cells are deduced from pressure gauge measurements of the total pressure in the gas manifold before a particular cell is sealed. Some cells were filled with gas mixtures of known compositions while others introduce

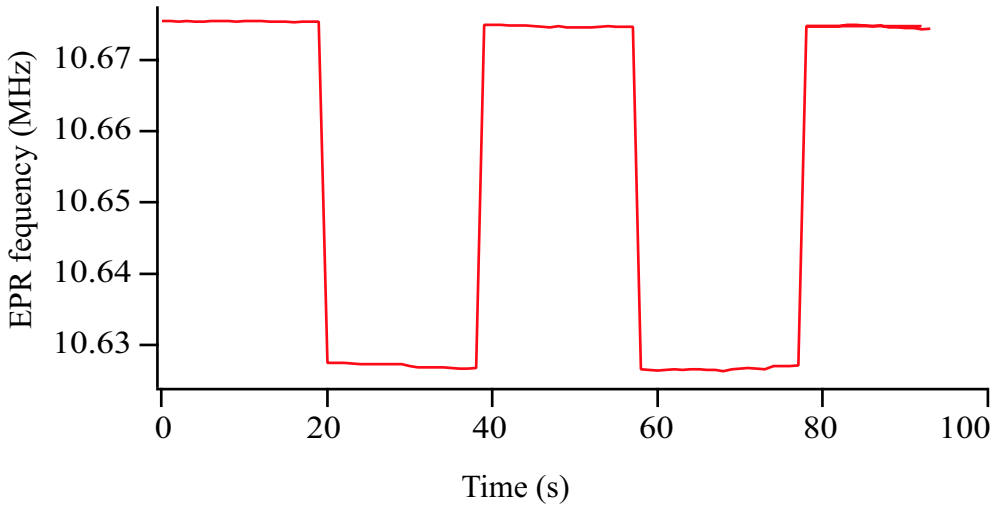

Fig. 3.24: A sample data set showing the EPR frequency as a function of time during a series of AFP reversals of the P_{He}.

a small pressure of N_2 followed by the ^{3}He. These cells are then "pulled off" of the gas manifold by using a flame to melt and seal the glass stem that was used to fill the cell. For cells with a total pressure over 1 atm this is done by holding the cell over liquid N_2 to keep the total pressure in the cell less than 1 atmosphere while it is being sealed.

Little work has been done to confirm that the final gas compositions have remained unchanged in these cells compared to the pressures deduced from the pressure gauge before the cell was sealed. This creates a potentially large and unknown source of error in determining the critically important ^{3}He polarization as well as other parameters important to accurate measurements in SEOP. The use of cells with valves to introduce the gas obviously would not pose these problems.

The neutron absorption of the cell is one method to deduce the partial ^{3}He pressure in a sealed SEOP cell. Further we have previously used the total pressure broadening of the Rb D_1 and D_2 transitions [Romalis97] to deduce the total density, but not the N_2 density. Here we describe a method that is a slight variant of the method described in [Chann02b]. We present an optical method to simultaneously determine the pressures

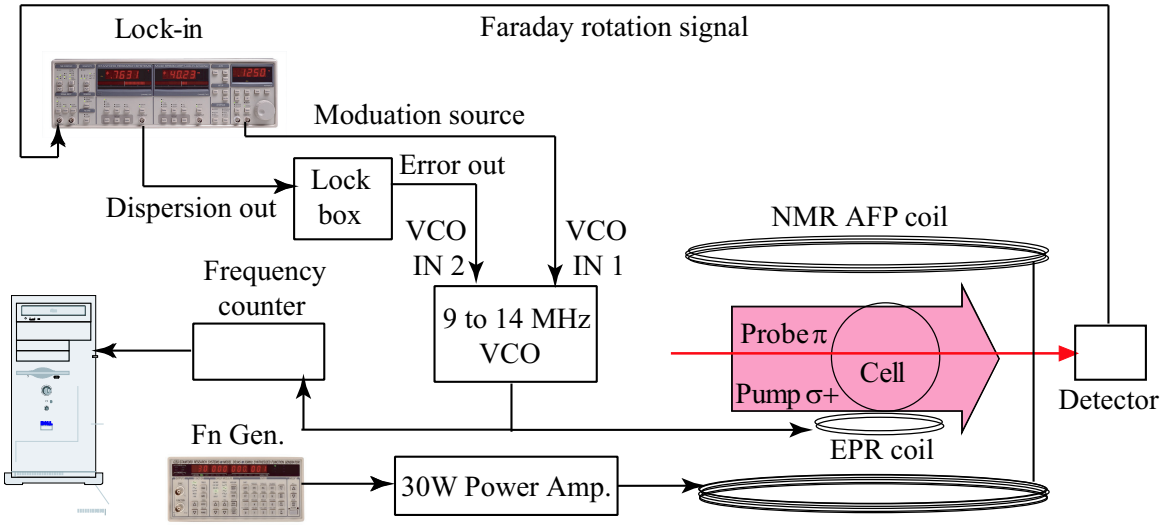

Fig. 3.25: Diagram of the setup used for the EPR frequency shift measurements, diagrams of the electric circuits for the 9-14MHz VCO, 30W power amplifier, and lock box are given in diagrams 3.23,3.21,and 3.22 respectively. The 9-14MHz VCO can be replaced by an adder to sum the two inputs and any function generator with a VCF input.

of both ^{3}He and N_2 inside sealed spin-exchange optical pumping cells. This is accomplished by measuring the combined [^{3}He] and [N_2] dependent linewidth broadening and line shift of the Rb $S_{1/2} \rightarrow P_{1/2}$ transition at 795nm [Romalis97]. Romalis and the Princeton group made precision measurements of these pressure broadening and pressure shift parameters. Table 3.4 lists the measured values for the pressure shifts and pressure broadening of the Rb D_1 and D_2 lines caused by ^{3}He and N_2. The N_2 data was taken at 353°C and the measured temperature dependance of the ^{3}He data is also listed [Romalis97]. The lines were also found to have a slight asymmetry, however this effect is negligibly small for the pressures used in SEOP [Romalis97].

Writing down the equations for the total pressure shifts and broadening by N_2 and ^{3}He, we obtain the following relations for the full width, $\Delta\nu_{FWHM}$, and center

Tab. 3.4: Values of the pressure broadening and pressure shifts coefficients for Rb in the presence of ^{3}He and N_2 . The temperature coefficients for ^{3}He are included, the N_2 data was taken at $353°C$[Romalis97].

Line	^{3}He	Temp. dep. (^{3}He)	N_2
D_1 full width	18.7 ± 0.3	$T^{0.05\pm0.05}$	17.8 ± 0.3
D_1 line shift	5.64 ± 0.15	$T^{1.1\pm0.1}$	-8.25 ± 0.15
D_2 full width	20.8 ± 0.2	$T^{0.53\pm0.06}$	18.1 ± 0.3
D_2 line shift	0.68 ± 0.05	$T^{1.6\pm0.4}$	-5.9 ± 0.1

frequency, ν_c, to be

$$\Delta\nu_{\mathrm{FWHM}} = [^3\mathrm{He}]\Delta\nu_{\mathrm{He}} + [\mathrm{N_2}]\delta\nu_{\mathrm{N_2}} \tag{3.50}$$

$$\nu_c = [^3\mathrm{He}]\nu_{\mathrm{He}} + [\mathrm{N_2}]\nu_{\mathrm{N_2}} + \nu_0. \tag{3.51}$$

Here $\Delta\nu_{\mathrm{He}}$ and $\delta\nu_{\mathrm{N_2}}$ are the contributions to the measured D1 linewidth from the ^{3}He and N_2 respectively and ν_{He} and $\nu_{\mathrm{N_2}}$ are the corresponding contributions to the line shift. Measuring both $\Delta\nu_{\mathrm{FWHM}}$ and ν_c allows us to deduce both $[^3\mathrm{He}]$ and $[\mathrm{N_2}]$.

A diagram of the optical setup to measure the absorption profiles is given in figure 3.26. The cell was heated to approximately $80°C$ to match the reference temperature of [Romalis97] and provide an appropriate optical depth for high signal to noise. The cell temperature is allowed to fully equilibrate for several hours. Data was then taken by tuning the probe laser in approximately 0.5 GHz steps which was the maximum resolution of our New Focus Inc. 7711 Fizzeau wave meter, and recording the detector signal of the reference beam and the absorption beam. The probe beam was chopped at about 1 Hz to allow us to easily measure the signal amplitudes. The resulting intensity normalized transmission as a function of frequency was fit to a Lorentzian

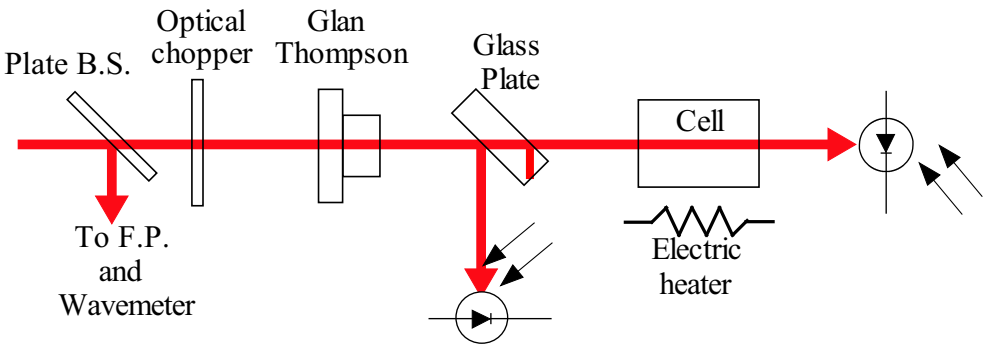

Fig. 3.26: Diagram of the setup used for measuring the line with and line shift of the Rb absorption profiles to determine [^{3}He] and [N_2].

absorption profile which included the hyperfine splitting of the ground state and the isotopic composition. An example of this data for the D_1 line is given in figure 3.27. The non-shifted reference value of the location of the Rb resonance was determined by replacing the SEOP cell in this apparatus with a vacuum Rb vapor cell that is normally used for locking lasers. The Doppler broadened spectra of this cell was then taken in the same way and fit to the same function to determine ν_0. A sample of the Doppler broadened spectra with fit is shown in figure 3.28. Placing the resulting ν_0, ν_c and $\Delta\nu_{FWHM}$ into equations 3.50 and 3.51 both [^{3}He] and [N_2] were determined.

In order to obtain highly accurate absorption profiles and more critically to accurately determine ν_0, the linewidth of the probe laser must be much less than the width of the absorption profile, and be free of etalon effects and scattered light that could provide errors in the normalization to the reference intensity. Therefore we constructed a simple single mode external cavity diode laser probe using a Hitachi 790 nm diode laser. A diagram of this cavity is shown in figure 3.29. The plate beam splitter proved to be a very important element to achieve single mode operation because without it, the grating, operating at the minimum feedback efficiency, gave too much feedback causing multi-mode operation with a linewidth greater than 2GHz. The diode was

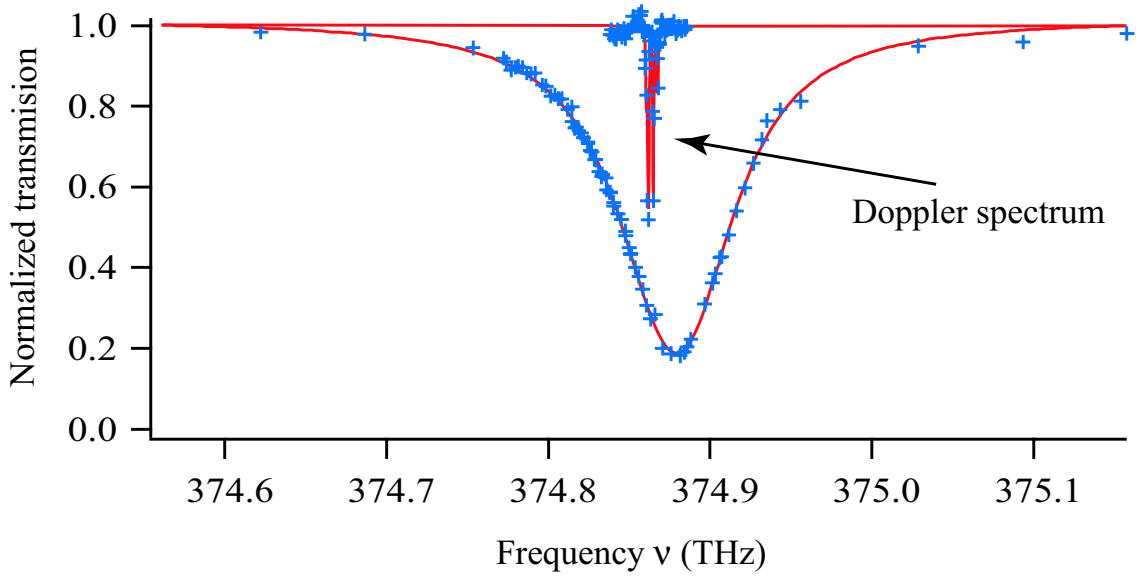

Fig. 3.27: Sample absorption spectra from Oscar and a vacuum vapor cell to show the pressure induced frequency shift.

tuned to the appropriate frequencies to scan the absorption profile by first tuning the temperature of the diode laser to cause it to lase near the desired frequency, then single mode operation was induced by a careful adjustment of the tilt and diffraction angle of the grating, fine tuning the diode current and adjusting the etalon. Once a stable single mode was found with iterative adjustments of these parameters, the laser frequency could be continuously tuned in single mode operation over tens of GHz by fine adjustments to the diode current. To insure proper operation during the course of a measurement the laser linewidth was continuously qualitatively monitored with a 1.5 GHz FSR Fabry Perot.

This procedure was performed on two visually identical SEOP cells, Felix and Oscar, the resulting values obtained are listed in table 3.2. If one is confident of the $[N_2]$ from the time of filling, one can just measure $\Delta\nu_{FWHM}$ to determine $[^3He]$ as we did for several cells with the results included in table 3.2.

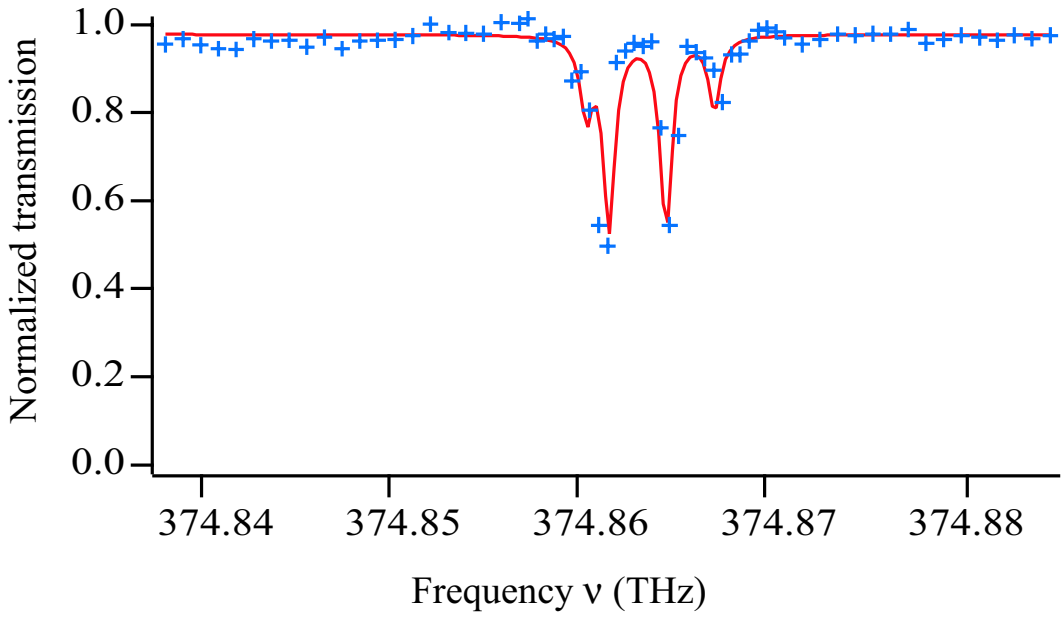

Fig. 3.28: Doppler absorption spectrum used to determine ν_0

3.8 Calibrated Photon Absorption

In our studies of SEOP we found it important to quantify the actual efficiency of turning polarized photons into polarized ^{3}He. We defined the photon efficiency of SEOP simply as the ratio of the ^{3}He polarization rate at low P_{He}, to the photon flux, $\delta\phi$, deposited in the volume V. The photon efficiency and the spin-exchange efficiency (the proportion of angular momentum transferred from the alkali-metal to the ^{3}He) are equal when the deposited photon flux is the ideal value,

$$\Delta\phi_i = \Gamma'_{\mathrm{Rb}} P_A[\mathrm{Rb}]V. \tag{3.52}$$

If the deposited photon flux exceeds $\Delta\phi_i$, the photon efficiency will be smaller than the spin-exchange efficiency.

The photon flux was determined by first measuring the intensity I, in $\frac{\mathrm{W}}{\mathrm{cm}^2}$, of our pump beam using a power meter with an aperture of fixed area placed directly in front of our oven. A geometric correction is made for any divergence of the pump beam

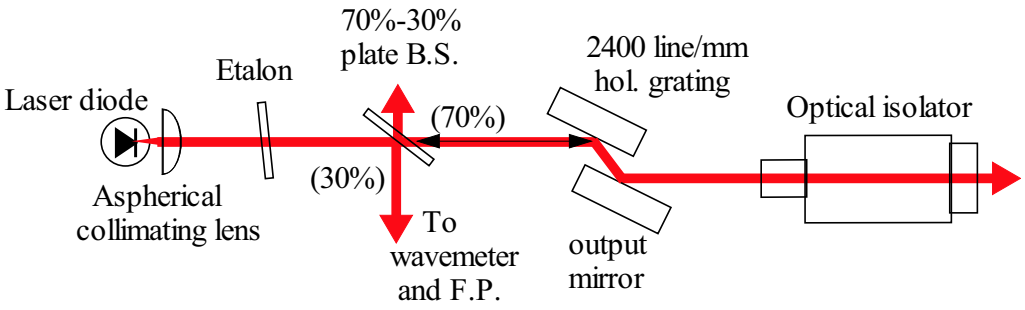

Fig. 3.29: Diagram of the single mode external cavity diode laser probe used for ^{3}He and N_2 density measurements.

before its light enters the cell. Further we subtract the power lost due to reflection at the front window of our oven and the front of the cell itself.

Next we measure the relative absorption, α, of the pump light passing through the center of the cell. This is done by using a lens placed behind the cell to form an image of the front of the cell. A pinhole is placed in the center of the image such that only the light that has passed through the center of the cell is allowed through. This light is then collected by another lens and focused onto a photodiode (see figure 3.30). A reference voltage is measured is when the cell is at room temperature to give the 100% transmission value or V_0. Then the oven and cell are heated to the temperature used for optical pumping and the corresponding voltage, V, is recorded and normalized to the 100% transmission value giving $\frac{V}{V_0}$. The absorption is then,

$$\alpha = I_0(97\%)^4 \left(1 - \frac{V}{V_0}\right), \tag{3.53}$$

where the $(97\%)^4$ is a correction to I_0 for the reflection losses by the un-coated front window of our oven and the front of the cell. The resulting product of $I_0(97\%)^4$ is the light intensity the atoms in the cell see. The back windows do not need to be accounted for because their contribution is corrected for by the normalization to the 100% transmission value.

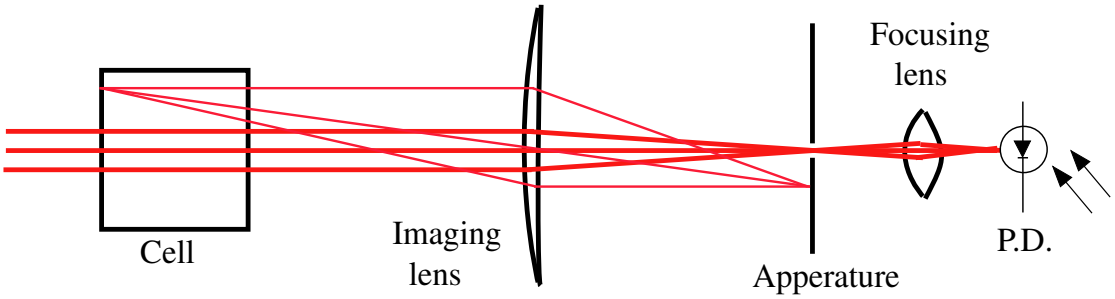

Fig. 3.30: Calibrated absorption apparatus.

For spherical cells, the product αA, where A is the cross sectional area of the cell in cm^2, is then multiplied by a geometric correction for the absorption of a uniform intensity beam passing through the spherical absorbing volume given numerically by,

$$\frac{1}{2z}\int_{-z}^{z}\sqrt{z^2+x^2+y^2}dz \simeq \frac{3}{2}. \tag{3.54}$$

Then we simply convert the intensity in W to photons using the convenient conversion factor for light at 795nm of 6×10^{19} photons = 15W to obtain the number of photons absorbed,

$$\Delta\phi = \frac{3}{2}I\alpha A\left(\frac{6\times10^{19}}{15}\right). \tag{3.55}$$

Chapter 4 gives a discussion and results of photon efficiency measurements using this calibrated absorption method.

4. HYBRID SPIN EXCHANGE OPTICAL PUMPING

4.1 Introduction

In this chapter we give a detailed description of a "hybrid" approach to realizing the higher efficiencies of K spin-exchange, which was first proposed by Happer and co-workers[Happer01] and was recently experimentally verified by our group[Babcock03]. Hybrid spin exchange optical pumping takes advantage of the increased spin-exchange efficiency of K atoms and combines it with the many experimental advantages of optically pumping Rb atoms. We optically pump a K-Rb vapor mixture, which can be predominantly K, using a standard Rb laser. Circularly polarized light from a 795nm laser optically pumps the Rb atoms, then spin-exchange collisions between the Rb and K atoms transfer the Rb polarization to the K atoms with little loss. K has a spin-exchange efficiency of 23% with ^{3}He, whereas the Rb efficiency is only 2% [Baranga98]. Thus if the K density greatly exceeds the Rb density, ^{3}He polarization is generated primarily by highly efficient collisions with K atoms, and only slightly via much less efficient collisions with Rb atoms. We present measurements two types of efficiencies, the spin-exchange efficiency, η_{SE}, and the photon efficiency, η_γ, for hybrid SEOP. η_{SE} is simply the ratio of angular momentum transferred in a Rb-^{3}He collision, while η_γ is the number of photons absorbed per polarized ^{3}He atom obtained. If the alkali-metal atoms polarize with 100% efficiency, as they are normally assumed to, these two efficiencies will be equal.

For both types of efficiencies, we find order-of-magnitude SEOP improvements for KRb-^{3}He as compared to Rb-^{3}He. However, we find $\eta_\gamma \ll \eta_{\rm SE}$ for both pure Rb and hybrid pumping. Our investigations show that small imperfections in the optical pumping process produce surprisingly large photon absorption. This chapter is broken into four parts. First we discuss the spin-exchange efficiency in 4.2, then we will consider the total photon efficiency in 4.3. Next a brief discussion of the experimental procedure is given in 4.4, and finally results and conclusions from both types of efficiency measurements will be summarized in 4.5.

4.2 HySEOP Spin Exchange Efficiency

Hybrid SEOP relies on rapid spin-transfer from the Rb to the K atoms. The ^{3}He polarization $P_{\rm He}$ is produced by collisions with both polarized K and polarized Rb, and is lost by the ^{3}He in other processes such as wall relaxation, He-He collisions and diffusion though magnetic field gradients at a combined rate of $\Gamma_{\rm He}$. The rate of gain of the ^{3}He polarization is given by

$$\frac{dP_{\rm He}}{dt} = \kappa_{\rm K}[{\rm K}](P_{\rm K} - P_{\rm He}) + \kappa_{\rm Rb}[{\rm Rb}](P_{\rm Rb} - P_{\rm He}) - \Gamma_{\rm He}P_{\rm He}. \tag{4.1}$$

Here $\kappa_{\rm K}$ and $\kappa_{\rm Rb}$ are the K and Rb spin-exchange rate coefficients and the factors in brackets are the alkali densities. The K-Rb spin-exchange cross section is extremely large, roughly 200 Å^2 [Happer72]. Therefore at typical densities of 10^{14} cm^{-3} or more, the K-Rb spin-exchange rate exceeds 10^5/s, which is much greater than the typical 500/s alkali spin-relaxation rates in ^{3}He spin-exchange cells. Thus the K and Rb atoms are in spin-temperature equilibrium [Anderson59, Happer72] and have equal electron spin-polarizations $P_{\rm A}$. With this simplification equation 4.1 becomes

$$\frac{dP_{\rm He}}{dt} = -\Gamma_{\rm He}P_{\rm He} + \Gamma_{\rm SE}(P_{\rm A} - P_{\rm He}), \tag{4.2}$$

where the total hybrid spin-exchange rate is $\Gamma_{\rm SE} = \kappa_{\rm K}[{\rm K}] + \kappa_{\rm Rb}[{\rm Rb}]$. The rate coefficients for K and Rb are similar in size, therefore the spin transfer rates are nearly proportional to the total alkali density.

In order to evaluate SEOP, we must also consider processes other than spin-exchange that remove angular momentum from the system. The alkali-metal atoms have spin relaxation rates on the order of a few hundred s^{-1} whereas the ^{3}He relaxation rates are on the order of $10^{-5}s^{-1}$. Thus the dominant collisional losses come from spin-relaxation of the alkali atoms.

The K atoms lose angular momentum by spin-exchange to ^{3}He, and also by spin-relaxation, in primarily K-K, K-Rb, and K-^{3}He collisions. (We estimate diffusion losses at the wall to be small.) The sum of the rate of change of the total angular momentum of the Rb and K atoms due to collisions, $\frac{{\rm dF_{Rb}}}{\rm dt}|_{\rm coll.}$ and $\frac{{\rm dF_K}}{\rm dt}|_{\rm coll.}$ respectively, can be written as

$$[{\rm Rb}]\frac{dF_{\rm Rb}}{dt}|_{\rm coll.} + [{\rm K}]\frac{dF_{\rm K}}{dt}|_{\rm coll.} = -[{\rm K}]\Gamma_{\rm K}S_{\rm K} - [{\rm Rb}]\Gamma_{\rm Rb}S_{\rm Rb} - [{\rm K}]\frac{q_{\rm KRb}}{2}[{\rm Rb}]S_{\rm K}$$

$$-[{\rm Rb}]\frac{q_{\rm KRb}}{2}[{\rm K}]S_{\rm Rb} + [{\rm K}]\kappa_{\rm K}[^3{\rm He}]\frac{P_{\rm He}}{2} + [{\rm Rb}]\kappa_{\rm Rb}[^3{\rm He}]\frac{P_{\rm He}}{2}, \qquad (4.3)$$

where $\Gamma_{\rm K}$ ($\Gamma_{\rm Rb}$) is the total K(Rb) spin relaxation rate from collisions with ^{3}He, N_2 and K (Rb). The spin relaxation rate coefficient for K-Rb collisions is $q_{\rm KRb}$. Once again using spin temperature, we have $S_{\rm K} = S_{\rm Rb} = P_{\rm A}/2$, and equation 4.3 becomes

$$\begin{aligned}
[{\rm Rb}]\frac{dF_{\rm Rb}}{dt}|_{\rm coll} + [{\rm K}]\frac{dF_{\rm K}}{dt}|_{\rm coll} &= \\
&= -([{\rm K}]\Gamma_{\rm K} + [{\rm Rb}]\Gamma_{\rm Rb} + [{\rm K}][{\rm Rb}]q_{\rm KRb})\frac{P_{\rm A}}{2} \\
&\quad +[^3{\rm He}](\kappa_{\rm K}[{\rm K}] + \kappa_{\rm Rb}[{\rm Rb}])\frac{P_{\rm He}}{2}, \\
&= -[{\rm Rb}]\Gamma'_{\rm Rb}\frac{P_{\rm A}}{2} + [^3{\rm He}](\kappa_{\rm K}[{\rm K}] + \kappa_{\rm Rb}[{\rm Rb}])\frac{P_{\rm He}}{2}, \qquad (4.4)
\end{aligned}$$

where we have replaced the individual alkali relaxation terms by the effective total Rb

relaxation rate. The total Rb relaxation rate is

$$\Gamma'_{\mathrm{Rb}} = \Gamma_{\mathrm{Rb}} + \mathcal{D}\Gamma_{\mathrm{K}} + q_{\mathrm{KRb}}[\mathrm{K}], \tag{4.5}$$

where $\mathcal{D} = [\mathrm{K}]/[\mathrm{Rb}]$ is the ratio of the alkali metal number densities. Under most conditions of interest the K-Rb loss rate $q_{\mathrm{KRb}}[\mathrm{K}]$ will be small.

We can now write the spin-exchange efficiency in hybrid spin-exchange optical pumping which we will define as the rate at which spin polarization is gained by the ^{3}He as compared to the rate at which it is lost by alkali relaxation, as

$$\eta_{\mathrm{SE}} = \frac{\Gamma_{\mathrm{SE}}[^3\mathrm{He}]}{[\mathrm{Rb}]\Gamma'_{\mathrm{Rb}}} = \frac{(\kappa_{\mathrm{Rb}} + \mathcal{D}\kappa_{\mathrm{K}})\,[^3\mathrm{He}]}{(\Gamma_{\mathrm{Rb}} + \mathcal{D}\Gamma_{\mathrm{K}} + q_{\mathrm{KRb}}[\mathrm{K}])}. \tag{4.6}$$

For large $\mathcal{D}$ the K-Rb spin-exchange efficiency is equal to the K-^{3}He spin-exchange efficiency $\kappa_{\mathrm{K}}[^3\mathrm{He}]/\Gamma_{\mathrm{K}}$.

Each of the quantities on the right hand side of equation 4.6 are directly measurable. Thus in order to fully evaluate the expected increase of efficiency for hybrid spin exchange we constructed a variety of hybrid spin-exchange cells with $\mathcal{D}$ from 1.5 up to 500. We were then able to measure measure η_{SE} as a function of $\mathcal{D}$; the results shown in figure 4.1 show good agreement with theory [Baranga98].

Our spin-exchange efficiency measurements are based on re-writing Eq. 4.6 in terms of measurable quantities. First we note that the measured "spin-up" time constant $\tau_{\mathrm{up}} = 1/\Gamma_{\mathrm{up}}$ is,

$$\frac{1}{\tau_{\mathrm{up}}} = \Gamma_{\mathrm{SE}} + \Gamma_{\mathrm{He}} \tag{4.7}$$

and the equilibrium helium polarization $P_{\mathrm{He}}^{\mathrm{eq}}$ is then

$$P_{\mathrm{He}}^{\mathrm{eq}} = P_A \frac{\Gamma_{\mathrm{SE}}}{\Gamma_{\mathrm{SE}} + \Gamma_{\mathrm{He}}}. \tag{4.8}$$

Combining these two relations we get that

$$\Gamma_{\mathrm{SE}} = \frac{P_{\mathrm{He}}^{\mathrm{eq}}/\tau_{\mathrm{up}}}{P_A}. \tag{4.9}$$

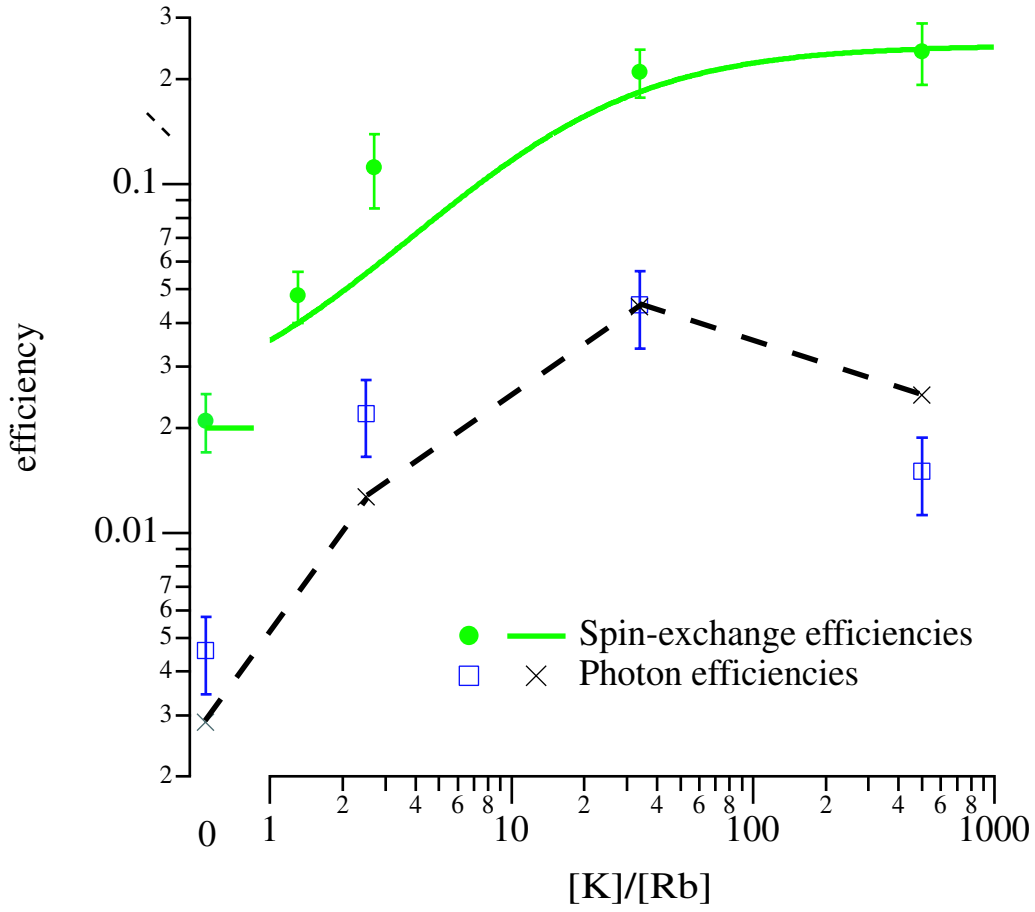

Fig. 4.1: $K - Rb - {}^3$He efficiencies, as a function of the K-Rb density ratio, at a temperature of 190°C. The filled circles are spin-exchange efficiency results, with the associated solid line being the expected values from previous Rb and K efficiency measurements (Ref.[Baranga98]). The hollow squares are photon efficiency measurements for broadband pumping, with the dashed line denoting the expected values corrected for imperfect optical pumping, using the results of Fig. 4.2.

Consequently the spin-exchange efficiency written in terms of measurable quantities becomes

$$\eta_{\mathrm{SE}} = \frac{[^3\mathrm{He}]P_{\mathrm{He}}^{\mathrm{eq}}/\tau_{\mathrm{up}}}{P_A[\mathrm{Rb}]\Gamma'_{\mathrm{Rb}}}. \tag{4.10}$$

4.3 HySEOP Photon Efficiency

The spin-exchange efficiency is the maximum possible efficiency for turning photons into polarized nuclei. If it is assumed that the photon absorption rate is $\Gamma'_{\mathrm{Rb}}[\mathrm{Rb}]P_{\mathrm{A}}$, meaning that polarized atoms do not absorb pump light, this would also be be the photon efficiency. However we know this is not the case for practical and fundamental perhaps reasons.

We define the photon efficiency of SEOP, η_γ, simply as the ratio of the ^{3}He polarization rate to the photon flux, $\delta\phi$, deposited in the volume V at low P_{He}, such that

$$\eta_\gamma = \frac{[^3\mathrm{He}]V dP_{\mathrm{He}}/dt}{\Delta\phi} = \frac{[^3\mathrm{He}]V P^{\mathrm{eq}}_{\mathrm{He}}/\tau_{\mathrm{up}}}{\Delta\phi}. \tag{4.11}$$

Comparison with Eq. 4.10 shows that the photon and spin-exchange efficiencies are equal when the deposited photon flux is the ideal value

$$\Delta\phi_i = \Gamma'_{\mathrm{Rb}} P_A[\mathrm{Rb}]V. \tag{4.12}$$

If the deposited photon flux exceeds $\Delta\phi_i$, the photon efficiency will be smaller than the spin-exchange efficiency.

In fig. 4.1 we present measured photon efficiencies, determined by measuring ^{3}He polarizations, spin-up time constants, and the absorbed photon flux, following the right-hand side of Eq. 4.11. The photon efficiencies for both pure Rb and hybrid cells are 5-20 times smaller than the spin-exchange efficiencies. Still, the efficiencies of the hybrid cells exceed that of pure Rb by as much as an order of magnitude.

A key experimental observation with the broadband source is that the alkali polarization, measured using EPR spectroscopy, saturates at a value that is less than 1, even for intense broadband pumping. We measured P_∞ for the cells at Amersham Health using the method described below. The results given in fig. 4.2 show that the

maximum polarization decreases with increasing $\mathcal{D}$, reaching 38% for the $\mathcal{D} = 500$ cell. We have found that one can achieve a Rb polarization $\sim 100\%$ using our narrow band source in pure Rb pumping and that even for the $\mathcal{D} = 500$, cell $P_\infty = 100\%$ when using intense narrow-band optical pumping. Due to circumstances at Amersham Health we were unable to further explore the differences between these two results.

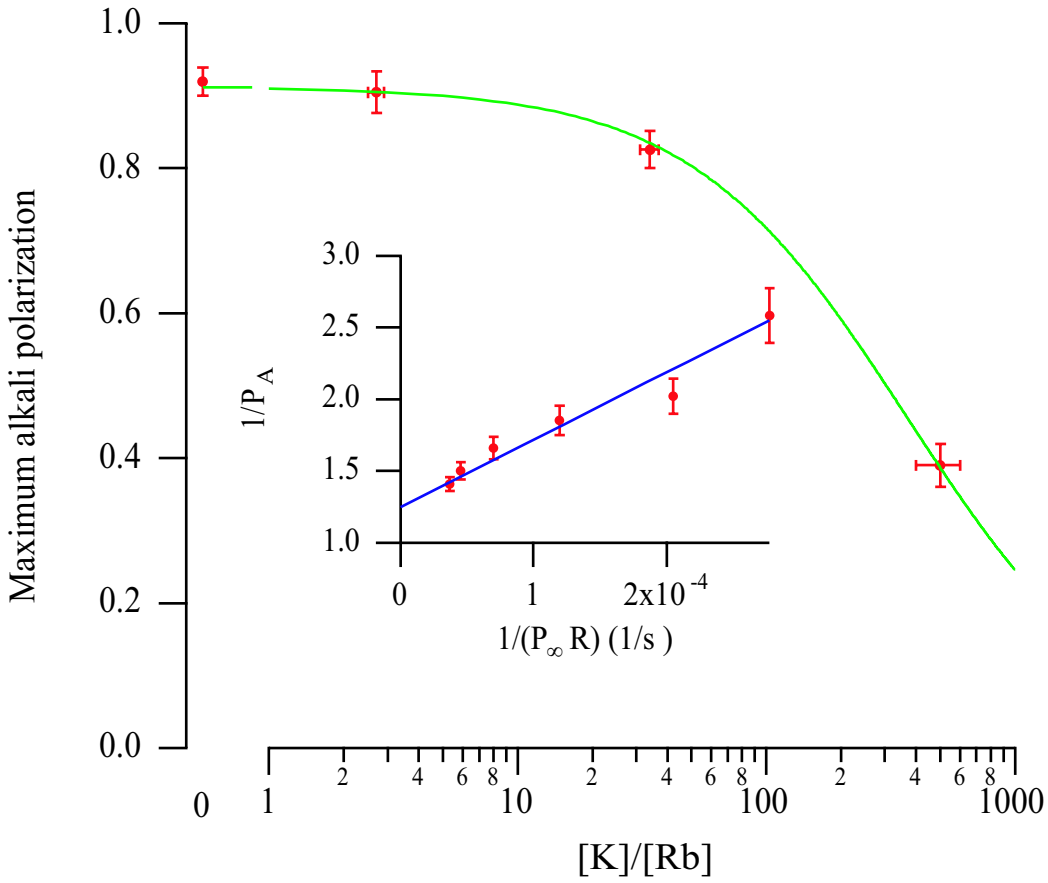

Fig. 4.2: Maximum attainable alkali polarization $P_A(\max)$ for the various 8 amagat cells pumped by broadband laser light. The solid line is the expectation assuming that the K atoms absorb the laser light at 0.27% of the Rb absorption rate, and assuming that in the absence of K atoms the Rb polarization is limited to $P_\infty = 0.91$. Inset: Determination of $P_A(\max)$ from polarization measurements as a function of the initial slope of optical pumping transients.

We postulate two effects to explain these alkali polarization limits for the broadband pumping. The strong dependence of the maximum polarization on $\mathcal{D}$ can be naturally explained by a small direct pumping rate (less than 1% that of Rb) for the K atoms, which would act to depolarize the K atoms. When $\mathcal{D}$ is large, the strong spin-exchange coupling of the two alkali species would then result in increased Rb light absorption as well. In addition, the observation of less-than-perfect Rb polarization, even under intense pumping conditions for pure Rb SEOP, implies a light-induced relaxation phenomenon of some type. We now present a phenomenological model to account for these observations.

We begin by reviewing the origin of Eq. 4.12. For ideal alkali D_1 optical pumping, assuming that the pressure broadening and/or laser linewidth greatly exceeds the hyperfine splitting (a condition well-satisfied here), the atoms absorb circularly polarized light at a rate per atom of $A = R(1 - P_A)$, where R is the optical pumping rate. The alkali atoms relax at a rate Γ_A, producing a polarization $P_A = R/(R+\Gamma_A)$, which then gives $A = \Gamma_A P_A$, from which Eq. 4.12 follows. A key assumption is that fully polarized atoms absorb no light. This may not hold in practice due to a variety of effects including: finite fine-structure splitting, off resonance D_2 pumping, and imperfect light propagation due to skew magnetic fields (section 7)[Chann02a]. Now we consider the nonideal case, where the highest attainable alkali polarization, P_∞, is less than 1. The rate of change of alkali polarization is given by

$$\frac{dP}{dt} = R(P_\infty - P_\mathrm{A}) - \Gamma_\mathrm{A} P_\mathrm{A}, \tag{4.13}$$

The resulting steady state alkali polarization is

$$P_\mathrm{A} = \frac{R P_\infty}{R_\mathrm{A} + \Gamma_\mathrm{A}}. \tag{4.14}$$

Given that the general form of the absorption of circularly-polarized light by a spin-1/2

atom is $A = R(1 - P_\infty P_A)$, the total absorption with $P_\infty \neq 100\%$ becomes

$$A = R(1 - \frac{R{P_\infty}^2}{R_\mathrm{A} + \Gamma_\mathrm{A}}) = \frac{\Gamma_\mathrm{A} P_\mathrm{A}}{P_\infty}(1 + \frac{R_\mathrm{A}}{\Gamma_\mathrm{A}}(1 - P_\infty^2)). \tag{4.15}$$

As a result, the ideal minimum amount of light absorbed given by Eq. 4.12 in this case is increased to

$$\Delta\phi = [\mathrm{Rb}]VA = [\mathrm{Rb}]V\Gamma_\mathrm{A}\frac{P_\mathrm{A}}{P_\infty}\left(1 + \frac{R}{\Gamma_\mathrm{A}}(1 - P_\infty^2)\right). \tag{4.16}$$

From Eq. 4.16, the deposited flux exceeds the ideal case by the factor $\Upsilon = 1/P_\infty + R(1 - P_\infty^2)/(\Gamma_A P_\infty)$. For the $\mathcal{D} = 500$ cell, typical alkali relaxation rates can easily be $3 \times 10^4 s^{-1}$, and $P_\infty = 0.38$, giving $\Upsilon = 13$. Consequently it is easy for the total SE efficiency to be an order of magnitude lower than the ideal value of Eq.4.6. Further, the above discussion is valid assuming that only the Rb atoms absorb the Rb D_1 pumping light.

Adding to these observations the possibility that the K atoms absorb 795 nm light at a modest rate changes equation 4.16 in two ways. First, a similar K absorption term must be added, with absorption rate R_K. Since the 795 nm laser light is far from the K resonances, the dichroism of the K atoms should be quite small. Second, the absorption of light by the K atoms acts as an additional relaxation mechanism for the Rb atoms that provide polarization to the K atoms by spin exchange.

The rate of change of the alkali polarization due to optical pumping of Rb and K by Rb D_1 light, with corresponding pumping rates R_{Rb} and R_K, is

$$[\mathrm{Rb}]\frac{dF_\mathrm{Rb}}{dt}_\mathrm{OP} + [\mathrm{K}]\frac{dF_K}{dt}_\mathrm{OP} = [\mathrm{Rb}]\frac{R_\mathrm{Rb}}{2}(P_{\infty\mathrm{Rb}} - P_\mathrm{A}) + [\mathrm{K}]\frac{R_\mathrm{K}}{2}(P_{\infty\mathrm{K}} - P_\mathrm{A}). \tag{4.17}$$

In steady state (with $P_\mathrm{He} = 0$),

$$0 = (R_\mathrm{Rb}(P_{\infty\mathrm{Rb}} - P_\mathrm{A}) - \Gamma_\mathrm{Rb}P_\mathrm{A} + \mathcal{D}(R_\mathrm{K}(P_{\infty\mathrm{K}} - P_\mathrm{A}) - \Gamma_\mathrm{K}P_\mathrm{A}. \tag{4.18}$$

Thus the alkali polarization becomes

$$P_{\mathrm{A}} = \frac{R_{\mathrm{Rb}} P_{\infty \mathrm{Rb}} + \mathcal{D} R_{\mathrm{K}} P_{\infty \mathrm{K}}}{R_{\mathrm{Rb}} + \Gamma_{\mathrm{Rb}} + \mathcal{D}(R_{\mathrm{K}} + \Gamma_{\mathrm{K}})}. \tag{4.19}$$

The K D_1 and D_2 resonances which occur at 770 nm and 766 nm respectively are over 25 nm away from the optically pumped D_1 resonance of Rb at 795 nm. The pumping rate, R_{K}, at large detuning, $\delta\nu$, is approximated by

$$R_{\mathrm{K}} \simeq 4R(\frac{\delta\nu}{\Lambda_{\mathrm{K}}})^{-2}, \tag{4.20}$$

where Λ_{K} is the pressure broadened linewidth which is on the order of 20 GHz/atmosphere, or $65 - 160GHz$ in our cells. Thus even for our $\mathcal{D} = 500:1$ cell, $\mathcal{D}R_{\mathrm{K}}/R < 0.3$, and since $P_{\infty \mathrm{K}}$ is also small, the product $\mathcal{D}R_{\mathrm{K}}P_{\infty \mathrm{K}}$ in the numerator of Eq. 4.19 can justifiably be neglected. Further comparison with Eq. 4.5, assuming the Rb-K spin loss term, q_{KRb}, is small, allows Eq. 4.19 to be rewritten as

$$P_{\mathrm{A}} = P_{\infty} \frac{R}{R + \mathcal{D}R_{\mathrm{K}} + \Gamma'_{\mathrm{Rb}}} \tag{4.21}$$

so that the maximum attainable alkali polarization is $P_A(\max) = P_{\infty}R/(R+\mathcal{D}R_{\mathrm{K}})$. As was noted earlier for the case of broadband pumping in the highest $\mathcal{D}$ cells, P_{∞} was less than 100%. The value of P_{∞} was obtained by measuring P_A, using EPR spectroscopy, as a function of $P_{\infty}R$, which is proportional to the laser intensity. In order to obtain the value of P_{∞}, Eq. 4.21 is inverted to give

$$\frac{1}{P_{\mathrm{A}}} = \frac{R + \mathcal{D}R_{\mathrm{K}} + \Gamma'_{\mathrm{Rb}}}{R P_{\infty \mathrm{Rb}}} = \frac{1}{P_{\infty \mathrm{Rb}}} + \frac{\Gamma'_{\mathrm{Rb}} + \mathcal{D}R_{\mathrm{K}}}{R P_{\infty \mathrm{Rb}}} \tag{4.22}$$

Assuming the $\mathcal{D}R_K$ term is small, a plot of $1/P_A$ vs $1/(P_{\infty}R)$ should be a straight line with slope Γ'_{Rb} and intercept $1/P_A(\max)$. We experimentally determine $P_{\infty}R$ from the slope $\mathcal{S} = dP_A/dt|_{P_A=0}$ of optical pumping transients that begin at $P_A = 0$; $P_{\infty}R = s\mathcal{S}$. An example of such a plot is shown as an inset of Fig. 4.2. Within errors (typically

15%), we find excellent agreement between Γ'_{Rb} determined from such plots and the independent measurement $\Gamma'_{\mathrm{Rb}} = s/\tau_A$. Values of $P_\infty = 0.91$ and $R_{\mathrm{K}}/R = 0.0027$ account well for our experimental observations, as shown in Fig. 4.2. We note however that this empirical value for R_{K}/R is a factor of 5 larger than expected from Eq. 4.20 and did not decrease with decreasing pressure as one would expect if it were caused by the pressure broadened lineshape.

Now we will explore the total spin-exchange efficiency. Taking into account the above described optical pumping effects, the absorbed photon flux $\Delta\phi$ for practical optical pumping follows from Eq. 4.17 and is

$$\Delta\phi = V([\mathrm{Rb}]R_{\mathrm{Rb}}(1 - P_{\infty\mathrm{Rb}}P) + [\mathrm{K}]R_{\mathrm{K}}(1 - P_{\infty\mathrm{K}}P_{\mathrm{A}})), \tag{4.23}$$

where V is the volume of the cell. The build up of polarization of ^{3}He atoms is

$$N_{\mathrm{He}}\frac{dP_{\mathrm{He}}}{dt} = (\kappa_{\mathrm{Rb}}[\mathrm{Rb}] + \kappa_{\mathrm{K}}[\mathrm{K}])P_{\mathrm{A}}[\mathrm{He}], \tag{4.24}$$

where N_{He} is the number of ^{3}He atoms in the cell.

Spin-exchange efficiency is, once again, the rate at which spin is accumulated in the ^{3}He atoms compared to the rate at which spin is lost by alkali spin relaxation. Also the efficiency for optical pumping, or "photon efficiency," is the ratio of the ideal absorbed photon flux, $[\mathrm{Rb}]\Gamma'_{\mathrm{Rb}}\mathrm{P_A V}$, to the practical absorbed photon flux $\Delta\phi$. Thus the total SEOP efficiency, η_{SEOP}, is the product of the spin-exchange efficiency η_{SE} and the optical pumping efficiency η_{OP}, or,

$$\eta_{SEOP} = \frac{(\kappa_{Rb}[Rb] + \kappa_K[K])}{[Rb]\Gamma'_{Rb}P_A}\frac{[Rb]\Gamma'_{Rb}P_A}{R_{Rb}[Rb](1 - P_{\infty\mathrm{Rb}}P_A) + [K]R_K(1 - P_{\infty\mathrm{K}}P_A)}, \tag{4.25}$$

where the optical pumping efficiency with some simplification is

$$\eta_{OP} = \frac{\Gamma'_{Rb}P_\infty R}{(R + \mathcal{D}R_K)^2 + \Gamma'_{Rb}(R + \mathcal{D}R_K) - P_\infty^2 R^2} \tag{4.26}$$

Using the measured values for each of the quantities in this equation, we show the deduced photon efficiencies in Fig. 4.1 and see that they account for the low values of the directly measured photon efficiencies.

The physical explanations for $P_\infty < 1$ and $R_K \neq 0$ are perhaps explained by D_2 pumping by D_1 resonant light. Using a narrowband, FNDAB, laser we can obtain $> 98\%$ alkali polarization, even for large $\mathcal{D}$ cells. Imperfect dichroism of the alkali-metal vapor could easily account for these observations. Our studies into this effect are discussed in a following chapter.

4.4 Experiment

Measurements were carried out at two locations. NH K-Rb and NH Rb were studied at the University of Wisconsin using the apparatus described in chapter 3. A 12-W frequency-narrowed diode array was used for the optical pumping. Amer2.5, Amer34, Amer500 and AmerRb were studied at Amersham Health using an 80 W unnarrowed diode array bar. Amer500 and AmerRb were also tested at Wisconsin.

The procedure for filling HySEOP cells with desirable proportions of K to Rb metal is given in section 3.4.1. We have studied 4 spherical hybrid cells, all made from GE180 glass: NH K-Rb, Amer2.5, Amer34, and Amer500 (table 3.2). NH K-Rb was a sealed 22.5 cm^3 cell, made at the University of New Hampshire [Pomeroy], that contained 3.3 amagat of ^{3}He. It has a room-temperature relaxation time of 92 hours and a density ratio of $\mathcal{D} = 1.5$. The other three cells were 187 cm^3, 7.9 amagat valved cells with 20, 65, and 55 hour relaxation times and $\mathcal{D} = 2.5$, 34, and 500 respectively. For relative comparisons, each cell had a nearly fraternal twin cell containing only Rb metal (NH Rb, and AmerRb).

First, for the measurement of spin exchange efficiency, we repeat the definition

of the spin exchange efficiency, derived earlier in terms of measurable quantities (eq. 4.10), to be

$$\eta_{\mathrm{SE}} = \frac{[^3\mathrm{He}]P_{\mathrm{He}}^{\mathrm{eq}}\Gamma_{\mathrm{He}}}{P_A[\mathrm{Rb}]\Gamma'_{\mathrm{Rb}}}. \tag{4.27}$$

For the photon efficiency, we repeat the earlier derived relation from equation 4.11, which is:

$$\eta_\gamma = \frac{[^3\mathrm{He}]VdP_{\mathrm{He}}/dt}{\Delta\phi} = \frac{[^3\mathrm{He}]VP_{\mathrm{He}}^{\mathrm{eq}}/\tau_{\mathrm{up}}}{\Delta\phi}. \tag{4.28}$$

The quantities in equations 4.27 and 4.28 are measured as follows. We deduce τ_{up} from the polarization build-up, detected via the time dependence of the amplitude of free-induction decay NMR (section 3.6.1). $P_{\mathrm{He}}^{\mathrm{eq}}$ is measured from the Rb (or K) EPR frequency shift (section 3.6.2),[Baranga98] and then extrapolated to infinite pumping time using the fit of the FID amplitudes. [Rb] and $\mathcal{D}$ is deduced from the fit of the wavelength dependance of the total Faraday rotation (section 3.5.2.1). The alkali polarization is measured using the method of EPR spectroscopy described in section 3.5.1,[Chann02b]. The absolute photon flux, $\Delta\phi$, is determined using the method described in section 3.8. Finally Γ'_{Rb} is measured by chopping the pump laser, and observing the longest time constant τ_A of decay of the alkali polarization with time (section 3.5.3),[Chann02b]. Or equivalently, Γ'_{Rb} is measured by the time constant of the repolarization signal (section 3.5.4). Note that $\Gamma'_{\mathrm{Rb}} = s/\tau_A$ where s is the slowing down factor [Chann02b].

The slowing down factors are 6 for pure K vapor and 10.8 for natural abundance Rb which we will label s_{K} and s_{Rb} respectively. In the case of hybrid pumping, the total observed relaxation of the alkali polarization is caused by the sum of the Rb and K relaxation with combined slowing down factor s, and can be written as

$$(s_{\mathrm{Rb}}[Rb] + s_K[K])\frac{dP_A}{dt} = -[Rb]\Gamma'_{\mathrm{Rb}}P_A = s\frac{dP_A}{dt}[Rb]. \tag{4.29}$$

Therefore the observed total decay of the alkali polarization over time is

$$\frac{dP_A}{dt} = -\frac{\Gamma'_{\mathrm{Rb}}[Rb]}{s} P_A, \tag{4.30}$$

where the value of s is given by the combined slowing down factor $s = s_{\mathrm{Rb}} + \mathcal{D}s_K$.

The EPR spectroscopy we used for observing P_{A} is actually a slight variation of that described in [Chann02b]. Since K has a much smaller hyperfine splitting than Rb, and therefore a larger quadratic Zeeman term, the separation between the rf resonances as he field is scanned is much larger for K, thus giving much higher resolution than either the ^{87}Rb or ^{85}Rb spectra [3.5.1]. Consequently we chose to measure the alkali polarization by driving the rf transitions of the ^{39}K($I = 3/2$), which occur at unshifted frequencies of 700kHz/G [Ramsey53]. In order to fully separate the $m_f = -2 \rightarrow -1$ and $m_f = -1 \rightarrow 0$ transitions of the K atoms from the corresponding transitions of the Rb^{87} (also with $I = 3/2$), we used a field of 34 gauss. A sample of the resulting spectra is shown in figure 4.3.

Due to the very low number density of Rb atoms in high $\mathcal{D}$ cells one must be careful not to saturate the rf transitions when measuring the EPR spectra, in order to obtain an accurate measurement. In practice EPR spectra are taken as a function of rf power, and the rf power is set to a level such that the measured polarization is constant with rf power.

Once all of these parameters are measured, η_{SE} and η_γ can be calculated using equations 4.27 and 4.28.

4.5 Conclusions

Using the data of Baranga *et al.* [Baranga98] for both Rb and K spin-exchange efficiencies, and using measured K and Rb spin-exchange rate coefficients reported in chapter 5 gives the curve shown in Fig. 4.1. Although modest density ratios of $\mathcal{D} \sim 1$

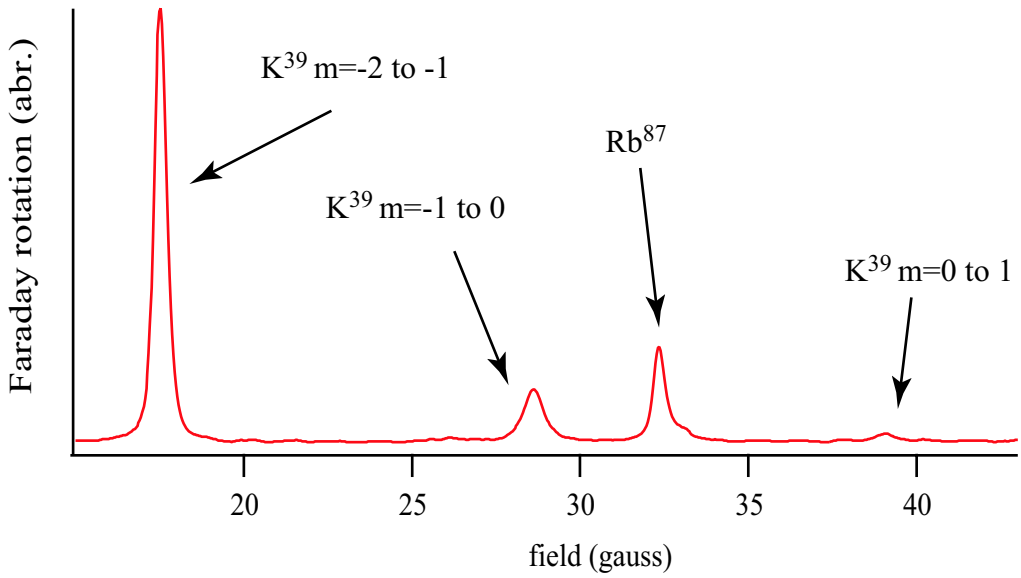

Fig. 4.3: Typical EPR spectrum showing the $I = 3/2$ isotopes. Note that for this figure the alkali polarization was less than 100% to show the resolution of the $m = -2 \rightarrow -1, m = -1 \rightarrow 0$, and the separation of ^{39}K from the ^{87}Rb resonances.

already promise substantial improvements, $\mathcal{D} \gg 10$ will be necessary to achieve the full promise of hybrid spin-exchange.

The polarizations and spin-up times achieved using narrow-band pumping of the $\mathcal{D} = 1.5$ sealed cell are shown in Fig. 4.4. The best performance was achieved at a temperature of 244°C, where the cell polarized to $P_{\mathrm{He}} = 0.73$ with $\tau_{\mathrm{up}} = 1.7$ hours. This is twice as fast as the twin Rb cell, as is expected for this density ratio. (Similar to our experience with Rb cells, the ^{3}He polarization does not achieve parity with the $> 95\%$ alkali polarization, even with extremely short spin-exchange times.)

These first studies of KRb hybrid spin-exchange optical pumping have confirmed the high spin-exchange efficiencies expected based on previous experiments on pure alkali vapors. The spin-exchange efficiency in K-Rb HySEOP can approach the expected 23% for a pure K spin-exchange with ^{3}He . Measurements of photon efficiencies derived from absolute polarimetry and photon absorption measurements also showed increased

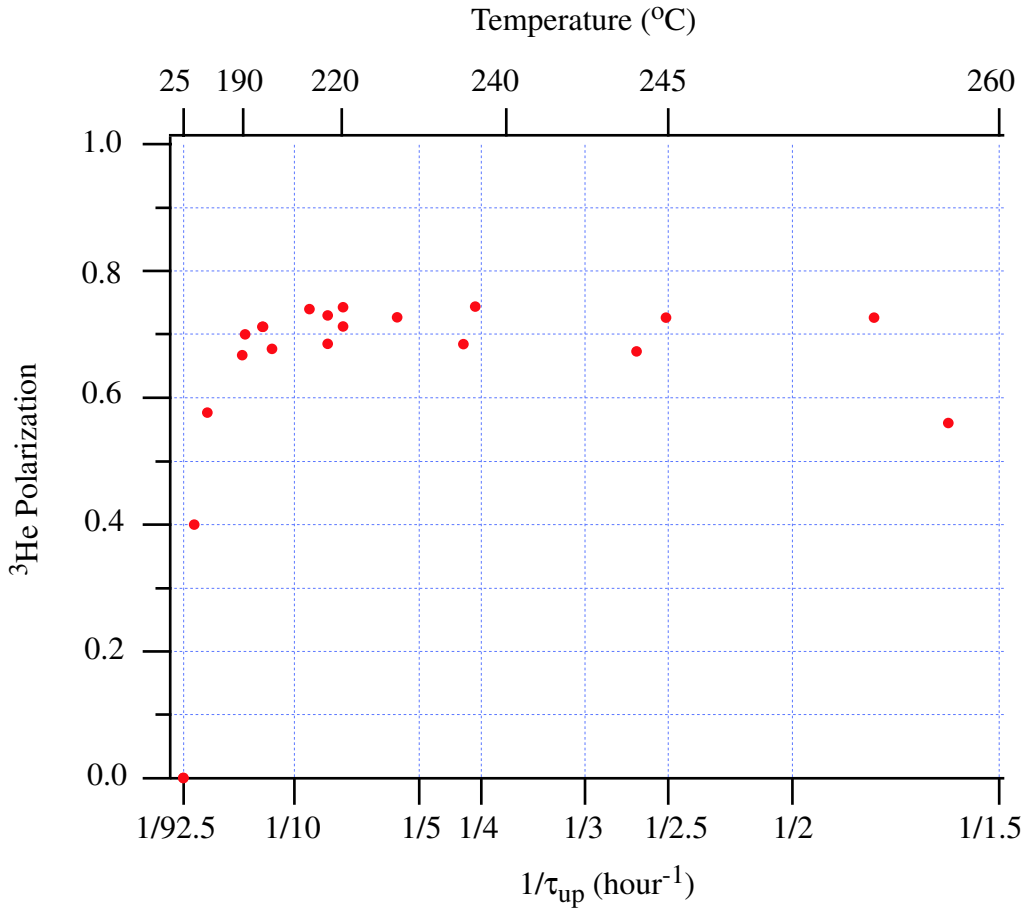

Fig. 4.4: Measured polarizations and spin-up times for a 25 cm^3, 3.3 amagat hybrid cell with $\mathcal{D} = 1.5$.

efficiency for hybrid pumping as compared to pure Rb pumping. We also show that imperfect optical pumping of the atoms significantly reduces the spin-exchange efficiency to roughly 10% of its maximum possible value for both the K-Rb and pure Rb cases. The possible sources of this experimental limit to the optical pumping are discussed further in chapter 7.

The increased spin-exchange rates achievable with hybrid pumping should be beneficial not only for polarizing large quantities of helium in a short time, as required for gas imaging or the large volumes for neutron spin-filters, but also for maintaining

polarization in the presence of depolarizing effects [Jones04]. We note that a Na-Rb hybrid could have virtually 100% efficiency [Borel03, Walker97], and might display much reduced Na pumping due to the much larger separation between the Na and Rb resonance wavelengths. Work is underway to extend this method to Na-Rb.

5. Rb-^{3}He AND K-^{3}He SPIN EXCHANGE RATE COEFFICIENTS

5.1 Introduction

Similar to the spin exchange efficiency, very few prior measurements of spin exchange rate coefficients have been made. Most of these measurements have been limited to Rb-^{3}He SEOP [Coulter88, Larson91, Baranga98]. Of these measurements, only the work of Baranga et. al [Baranga98] did not rely on assumptions about the ^{3}He wall relaxation, and Rb densities were not deduced saturated vapor pressure curves. These assumptions have has been determined to induce potential errors of as much as a factor of 2 [Borel02, Jau02]. Borel et al. used a method similar to Baranga et. al to measure the spin exchange rate coefficients for Na, by directly optically pumping an Na vapor with a dye laser. The measurements we present here were also obtained using the method that is a slight variation of ref. [Baranga98] as well as by using a new method that takes advantage of the additional diagnostics we have developed. Further, we extend both of these methods to application in HySEOP, namely K-Rb cells, which allows one to potentially measure the spin exchange rate coefficients for any alkali using a single HySEOP setup, which uses an inexpensive and readily available Rb SEOP pump laser (chapter 2).

The rate coefficient measurements, combined with spin exchange efficiency measurements described in chapter 4, allow us to determine both the spin exchange and spin loss terms of the alkali-metal-^{3}He Hamiltonian [1.8] and corresponding alkali-metal-^{3}He

cross sections. We obtained a value of $\kappa_{\mathrm{SE}}^{\mathrm{Rb}} = 6.76 \pm 0.1 \times 10^{-20} cm^3 s^{-1}$ for the average of the two methods for Rb-^{3}He and an average value of $\kappa_{\mathrm{SE}}^{\mathrm{K}} = 5.5 \pm 0.2 \times 10^{-20} cm^3 s^{-1}$ for K-^{3}He. The results for Rb are in excellent agreement with the prior measurement of [Baranga98].

5.2 Spin Exchange Rate Coefficients

Hybrid spin exchange cells provide a very convenient means to study the important spin-exchange parameters of alkalis other than Rb, without making significant changes to the basic apparatus or experimental technique. Our spin exchange rate coefficient measurements are a slight variation of the methods presented in references [Chann02b, Baranga98] for pure Rb with ^{3}He. The methods described make no assumptions regarding the nature of ^{3}He wall relaxation, or the equilibrium value of P_{He}.

First we consider the gain of polarization of ^{3}He in SEOP in terms of angular momentum. Here we will neglect the last term in the Hamiltonian (equation 1.8), the anisotropic spin exchange term, because experimental and theoretical evidence suggest it will be small [Walter98](chapter 8). Any changes or modifications induced by a non-negligible contribution from an anisotropic spin exchange term will be discussed below. The rate at which angular momentum is gained by the ^{3}He during Rb SEOP is given by

$$\frac{d\langle K_z\rangle}{dt} = \kappa_{\mathrm{SE}}^{\mathrm{Rb}}[\mathrm{Rb}](\langle S_z\rangle - \langle K_z\rangle) - \Gamma_{He}\langle K_z\rangle . \tag{5.1}$$

The two terms on the right hand side are well known and are responsible for alkali-^{3}He spin exchange and ^{3}He relaxation respectively [Walker97, Appelt98]. The spin-exchange occurs due to the short range Fermi contact hyperfine interaction, $\alpha K S$, between the ^{3}He with nuclear spin K, and the alkali, with electron spin S, with a rate coefficient

of $\kappa_{\mathrm{SE}}^{\mathrm{Rb}}$. K_z and S_z are the ^{3}He nuclear spin and the alkali electron spin in the z direction, which is the direction of the applied static holding field. Γ_{He} is the combined ^{3}He relaxation rate from all possible sources. These sources include ^{3}He-^{3}He dipole-dipole relaxation, ΔB relaxation, wall relaxation, and any possible extra sources of relaxation, which we have called the X-Factor and which will be discussed in chapter 8. The z components of K and S can be exchanged for polarizations with the relations $P_A = 2\langle S_z \rangle$ and $P_{\mathrm{He}} = 2\langle K_z \rangle$, respectively.

Our first method to measure the spin-exchange rate coefficient, which we call the rate balance method [Chann02b], is based on rewriting equation 5.1 in equilibrium (i.e. steady state) and solving for $\kappa_{\mathrm{SE}}^{\mathrm{Rb}}$. First we note that the measured "spin-up" time constant $\tau_{\mathrm{up}} = 1/\Gamma_{\mathrm{He}}$ is

$$\frac{1}{\tau_{\mathrm{up}}} = \kappa_{\mathrm{SE}}[\mathrm{Rb}] + \Gamma_{\mathrm{He}}. \tag{5.2}$$

Now the equilibrium helium polarization $P_{\mathrm{He}}^{\mathrm{eq}}$ is

$$P_{\mathrm{He}}^{\mathrm{eq}} = P_A \frac{\Gamma_{\mathrm{SE}}}{\Gamma_{\mathrm{SE}} + \Gamma_{\mathrm{He}}} = P_A \frac{\kappa_{\mathrm{SE}}[\mathrm{Rb}]}{\Gamma_{\mathrm{He}}}, \tag{5.3}$$

where $\Gamma_{\mathrm{SE}} = \kappa_{\mathrm{SE}}[Rb]$ is the spin exchange rate. Combining these two relations we find the rate balance Rb-^{3}He spin exchange rate coefficient to be

$$\kappa_{\mathrm{SE}}^{\mathrm{Rb}} = \frac{P_{\mathrm{He}}^{eq.}/\tau_{\mathrm{up}}}{P_{\mathrm{A}}[\mathrm{Rb}]}. \tag{5.4}$$

Were all of the parameters on the right hand side of 5.4 are measured, and therefore make no assumptions about the nature of ^{3}He wall relaxation.

We can now rewrite eq. 5.1 for a cell containing a mixture of alkali-metals, in this example K and Rb, where Rb is the species being optically pumped. In this case we obtain

$$\frac{d\langle K_z \rangle}{dt} = (\kappa_{\mathrm{SE}}^{\mathrm{Rb}}[\mathrm{Rb}] + \kappa_{\mathrm{SE}}^{\mathrm{K}}[\mathrm{K}])(\langle S_z \rangle - \langle K_z \rangle) - \Gamma_{\mathrm{He}} \langle K_z \rangle, \tag{5.5}$$

where $\kappa_{\mathrm{SE}}^{\mathrm{K}}$ and [K] are the K spin exchange rate coefficient and K density, respectively. Because of spin temperature S_z is equal for both alkalis. We use an identical analysis to that above, this time solving for $\kappa_{\mathrm{SE}}^{\mathrm{K}}$. Using this analysis one obtains

$$\kappa_{\mathrm{SE}}^{\mathrm{K}} = \frac{\Gamma_{\mathrm{He}} P_{\mathrm{He}}^{eq.} - \kappa_{\mathrm{SE}}^{\mathrm{Rb}}[\mathrm{Rb}] P_{\mathrm{A}}}{P_{\mathrm{A}}[\mathrm{K}]} \tag{5.6}$$

for the K spin-exchange rate coefficient. Using our previous measurement of $\kappa_{\mathrm{SE}}^{\mathrm{Rb}}$, we can then measure $\kappa_{\mathrm{SE}}^{\mathrm{K}}$. Note that in the limit where [K] $\gg$ [Rb], one obtains eq. 5.4 for K and therefore can directly measure the K spin-exchange rate coefficient directly.

The second method, which has been called the repolarization method [Chann02b, Baranga98], is in many ways completely complimentary to the rate balance method. The repolarization method is based on the transfer of angular momentum from polarized ^{3}He to the alkali-metal in the absence of optical pumping.

The total longitudinal spin $\left\langle F_z^{\mathrm{A}} \right\rangle^0 = \left\langle I_z^{\mathrm{A}} \right\rangle^0 + \langle S_z \rangle^0$, where the A is the alkali-metal species and the 0 superscript denotes the absence of optical pumping, is deposited in the alkali from the ^{3}He according to the following equation:

$$\frac{d\left\langle F_z^{\mathrm{Rb}} \right\rangle^0}{dt} = D\nabla^2 \left\langle F_z^{\mathrm{Rb}} \right\rangle^0 - \Gamma_{\mathrm{Rb}} \langle \mathrm{S}_z \rangle^0 + [^3\mathrm{He}] \left(\kappa_{\mathrm{SE}}^{\mathrm{Rb}}\right) (\langle K_z \rangle^0 - \langle S_z \rangle^0). \tag{5.7}$$

The first term is the spin loss due to diffusion. This term can be completely neglected due to the small diffusion constant D [Happer72, Appelt98]. The second term Γ_{Rb} is the measured Rb relaxation which is assumed to be solely from electron spin randomization [Happer72, Chann02b]. The last term is the spin transfer term between the polarized ^{3}He and the Rb. Thus we can see that the last two terms give us the exact same form as eq. 5.1. Replacing the longitudinal spins K_z and S_z with their equivalent polarizations and solving eq. 5.7 in steady state for the Rb spin exchange rate coefficient we obtain;

$$\kappa_{\mathrm{SE}}^{Rb} = \frac{\Gamma_{\mathrm{Rb}} P_{\mathrm{A}}^0}{[^3\mathrm{He}] P_{\mathrm{He}}^0}. \tag{5.8}$$

Here P_{A}^0 is the alkali re-polarization, or the value of alkali polarization that is induced by collisions with the polarized ^{3}He in the absence of optical pumping. P_{He}^0 is simply the value of the ^{3}He polarization at the time of the P_A^0 measurement. Once again in this case the measure alkali relaxation rates as "slowed down" because of spin exchange coupling with the alkali-metal nuclear spin. Therefore the measured relaxation rate, γ must be multiplied by the slowing down factor, $s = 10.8$ for natural abundance Rb, to obtain $\Gamma_{\mathrm{Rb}} = s\gamma$.

Now using the repolarization method to consider a cell containing a mixture of alkali-metals, we rewrite eq. 5.7 for a cell containing K and Rb. The new rate of transfer of angular momentum to both of the alkali-metal vapors, ignoring the diffusion term, is

$$[\mathrm{Rb}]\frac{d\left\langle F_z^{\mathrm{Rb}}\right\rangle^0}{dt} + [\mathrm{K}]\frac{d\left\langle F_z^{\mathrm{K}}\right\rangle^0}{dt} = \\ -\left([\mathrm{Rb}]\Gamma_{\mathrm{Rb}} + [\mathrm{K}]\Gamma_{\mathrm{K}} + [\mathrm{K}][\mathrm{Rb}]q_{\mathrm{KRb}}\right)\left\langle \mathrm{S}_z\right\rangle^0 \\ +[^3\mathrm{He}]\left(\kappa_{\mathrm{SE}}^{\mathrm{K}}[\mathrm{K}] + \kappa_{\mathrm{SE}}^{\mathrm{Rb}}[\mathrm{Rb}]\right)\left(\langle K_z\rangle^0 - \langle S_z\rangle^0\right) \quad (5.9)$$

The first term on the left hand side is the alkali-metal relaxation term for a HySEOP cell [Babcock03]. The second term on the left side is the spin transfer terms from the polarized ^{3}He both of the alkalis. We again note that K and Rb have equal electron spin due to spin temperature. The total observed alkali relaxation rate for HySEOP, Γ''_{Rb}, is

$$\Gamma''_{\mathrm{Rb}} = \left(\Gamma_{\mathrm{Rb}} + \mathcal{D}\Gamma_{\mathrm{K}} + [\mathrm{K}]q_{\mathrm{KRb}}\right), \quad (5.10)$$

where $\mathcal{D} = [\mathrm{K}]/[\mathrm{Rb}]$, which is the K to Rb density ratio, and q_{KRb} is the K-Rb collisional spin loss coefficient.

Equation 5.9 is then solved in the steady state, just as eq. 5.1 was. This equation

is then solved for the repolarization K spin-exchange rate coefficient to yield

$$\kappa_{\mathrm{SE}}^{\mathrm{K}} = \frac{\Gamma''_{\mathrm{Rb}} P_{\mathrm{A}}^{0}}{[^3\mathrm{He}]\mathcal{D} P_{\mathrm{He}}^{0}} - \frac{\kappa_{\mathrm{SE}}^{\mathrm{Rb}}}{\mathcal{D}}. \tag{5.11}$$

Once again we note that for the case where [K] $\gg$ [Rb], or $\mathcal{D}$ is large, the K spin exchange rate is directly measured.

We make an additional note here that about the effects on these methods of a non-negligible anisotropic spin exchange term. The anisotropic spin exchange would arise from the $\mathcal{B}_b \mathrm{K} \cdot (3\hat{\mathrm{R}}\hat{\mathrm{R}} - 1) \cdot \mathrm{S}$ term in the spin exchange Hamiltonian (eq. 1.8. This term results in a coupling of the spins of the alkali-metal electron and ^{3}He nucleus due to the long-range classical dipole-dipole interaction and 2^{nd} order spin-orbit interaction [Walter98]. Anisotropic spin exchange is usually ignored because its value is expected to be less than 3% of the $\mathcal{A}_b \mathrm{K} \cdot \mathrm{S}$ term for Rb-^{3}He, and less than 4% for K-^{3}He [Walter98]. However it is important to note that this process would polarize the ^{3}He in an opposite direction to that of the Fermi-contact, or spin exchange term, term. It can be shown that inclusion of the anisotropic term in the above analysis for both the rate balance and the repolarization methods would make the measured spin exchange rate, $\kappa_{\mathrm{SE}}^{meas.}$, become [Chann02b],

$$\kappa_{\mathrm{SE}}^{meas.} = \kappa_{\mathrm{SE}} - \frac{\kappa_{an.}}{2}, \tag{5.12}$$

where $\kappa_{an.}$ is the anisotropic spin exchange rate coefficient.

The methods for measuring many of these various terms were described earlier in chapter 3. Γ_{He} is the measured ^{3}He spin-up time constant as measured using small tip angle Free Induction Decay (FID) NMR, to sample the relative ^{3}He with minimal amounts of loss as a function of time. $P_{\mathrm{He}}^{eq.}$ is measured via the EPR frequency shifts of either the Rb or K [Romalis97, Babcock05] and extrapolated to the steady state value using the FID spin up data. [Rb] and [K] are measured with the polarization dependent Faraday rotation of our probe beam. P_{A} is measured using EPR spectroscopy

[Chann02b], usually on the ^{39}K atoms in HySEOP cells or ^{85}Rb in standard Rb SEOP cells. P_{A}^{0} is measured by "chopping" the alkali polarization by pulsing a rf coil tuned to the Rb or K EPR resonance frequency, at low field, to temporarily depolarize the alkali atoms. This allows us to find θ^{0}, which is the amplitude of the polarization Faraday rotation signal from the repolarization of the alkali by the ^{3}He. The alkali-metal polarization induced by spin exchange with the ^{3}He will be on the order of the efficiency for the particular alkali-metal-^{3}He pair. Consequently, values of these rotations can often be on the order of 1 degree or less for Rb, thus for this measurement we use a half wave plate holder with a micrometer actuator with a resolution of 1 minute. The value of this rotation is then divided by θ, the value of polarization Faraday rotation for a 100% polarized cell from equation 3.22, at the same density and probe laser wavelength to obtain P_{A}^{0}.

5.3 Results

The value we determined for the effective spin-exchange rate coefficient for K-^{3}He using these methods is given in table 5.1. Our average result, $\kappa_{\mathrm{K}} = 5.5 \pm 0.4 \times 10^{-20}$ cm^{3}s^{-1}, is 18% less than the Rb-^{3}He value of $6.8 \pm 0.2 \times 10^{-20}$ cm^{3}s^{-1} and similar to the value of the spin-exchange rate coefficient for Na-^{3}He obtained by Borel et. al. [Borel03].

Tab. 5.1: Results spin exchange rate coefficient measurements for Rb and K using the repolarization method (repol.), and the rate balance method (rate).

Alkali-metal	κ_{SE} (rate) ($\mathrm{cm^3 s^{-1}}$)	κ_{SE} (repol.) ($\mathrm{cm^3 s^{-1}}$)	Average κ_{SE} ($\mathrm{cm^3 s^{-1}}$)
Rb	$6.67 \pm 0.14 \times 10^{-20}$	$6.86 \pm 0.14 \times 10^{-20}$	$6.76 \pm 0.1 \times 10^{-20}$
Rb[a]		$6.7 \pm 0.06 \times 10^{-20}$	
K	$5.6 \pm 0.2 \times 10^{-20}$	$5.4 \pm 0.3 \times 10^{-20}$	$5.5 \pm 0.2 \times 10^{-20}$

Here we point our that if we take the square root of the product of our two methods for measuring κ_{SE} for pure Rb for example, we obtain

$$\sqrt{\kappa_{\mathrm{SE}}^{rate}\kappa_{\mathrm{SE}}^{repol.}} = \sqrt{\frac{\Gamma_{\mathrm{He}}P_{\mathrm{A}}^{0}\Gamma_{\mathrm{Rb}}P_{\mathrm{He}}^{eq.}}{P_{\mathrm{A}}[\mathrm{Rb}][\mathrm{He}]P_{\mathrm{He}}^{0}}}. \tag{5.13}$$

Here the product $P_{\mathrm{A}}[\mathrm{Rb}]$ is simply the value of the polarization Faraday rotation signal, P_{A}^{0} is the ratio of the polarization Faraday rotation signal in the absence of optical pumping, θ^{0}, to polarization Faraday rotation signal with $P_{\mathrm{A}} = 100\%$, or $\theta^{P=100\%}$, and the ratio $P_{\mathrm{He}}^{eq.}/P_{\mathrm{He}}^{0}$ is simply a normalization constant from the NMR FID. Therefore all the possible systematic errors reduce to $\sqrt{1/([\mathrm{He}]\theta^{P=100\%})}$. Under most circumstances [He] is determined to a high accuracy. In addition, the alkali polarization is fully saturated at $P_{\mathrm{A}} = 1$ over a larger range of alkali-metal densities when using our high-power FNDAB, but when it is not it can be normalized by direct measurement of P_{A} using EPR spectroscopy. Consequently we feel the rate coefficient averaged in this way is very insensitive to the most common systematic sources of error in SEOP which are absolute Helium polarization and alkali-metal density.

[0] [a]Reference [Baranga98]

The methods presented here could easily be extended to measure the ^{3}He spin exchange rate for any alkali-metal, Rb would be used for the optical pumping alkali and the second alkali would be measured. The only caveat is that an additional probe laser would be needed to probe the density of the secondary alkali. For example this process would be ideal for Na because directly pumping Na would require the use of a high-power dye laser.

6. EPR FREQUENCY SHIFT ENHANCEMENT FACTORS FOR Na, K AND Rb

6.1 Introduction

In this chapter we present temperature dependent measurements of the EPR frequency shift enhancement factors, κ_0, for K-^{3}He and Na-^{3}He. Additionally, we greatly extend the measured temperature range of κ_0 for Rb-^{3}He. Our approach, which stems from the idea of HySEOP, is to use cells containing mixtures of Rb and another alkali. In these cells the κ_0 of the secondary alkali, K or Na, is determined directly from the measurable ratios of its frequency shifts to that of Rb-^{3}He, which is known to high accuracy for temperatures from 120°C to 175°C [Romalis98]. The values we obtained are $\kappa_0^{Rb} = 6.39 + 0.00914[T - 200(^\circ C)]$, $\kappa_0^K = 5.99 + 0.0086[T - 200(^\circ C)]$, and $\kappa_0^{Na} = 4.84 + 0.00914[T - 200(^\circ C)]$, for Rb, K and Na respectively. The values of κ_0 presented here are of critical importance to further study of HySEOP and SEOP with alkali-metals other than Rb. The theory of the EPR frequency shifts was described previously in 3.6.2.1. Section 6.2 describes this experiment and section 6.3 summarizes our results.

6.2 Experiment

Our basic apparatus has been described in section 3.6.2. Spherical hybrid Na-Rb or K-Rb cells, with nearly equal proportions of Na or K to Rb in the vapor phase, are

pumped using a diode laser tuned to the Rb D_1 line. Rapid spin-exchange among all of the alkali atoms (regardless of species) ensures spin-temperature equilibrium and therefore equal polarizations. The spin-polarization of the alkali atoms is monitored using either transmission of the pumping light through the cell or by Faraday rotation of a weak diode laser (<5mW) tuned slightly off the Rb D_2 line. We note that this procedure is insensitive to both absolute ^{3}He polarization and density, eliminating many sources of systematic error. We also note that the Na-Rb and K-Rb amalgams used for HySEOP have lowered vapor pressure curves as given by Raoult's law [CRC], and higher photon efficiency. Both of these effects allow us to maintain a highly polarized Rb vapor, and to measure κ_0^{Rb}, at significantly higher temperatures than in a pure Rb optical pumping cell.

EPR spectra are obtained by driving the K/Na and Rb resonances with a transverse rf magnetic field, which is generated by a coil that is purposely operated far from any coil resonances (ensuring constant rf amplitude as a function of rf frequency), and by sweeping the rf frequency. As the frequency becomes resonant with any one of the atomic resonances, the alkali becomes slightly depolarized, the transmission of the pumping light lessens, and the plane of polarization of the probe light changes. An example spectrum is shown in Fig. 6.1. Equivalently, one could obtain the spectra by holding the EPR frequency constant and sweeping the magnetic field. There is a tremendous amount of information in these spectra, but in this section we focus on the dependence of the resonance frequencies on the nuclear spin-polarization of the ^{3}He atoms.

The frequency shift of the alkali-metal $m = -F \rightarrow m' = -F + 1$ EPR line due the polarized ^{3}He in a cell of spherical geometry, is [Romalis98] (eq. 3.40),

$$\Delta\nu_0 = \frac{8\pi}{3}\frac{g_s\mu_B}{(2I+1)h}\left(1+\epsilon\right)\kappa_0\mu_K[\mathrm{He}]P_{\mathrm{He}}, \tag{6.1}$$

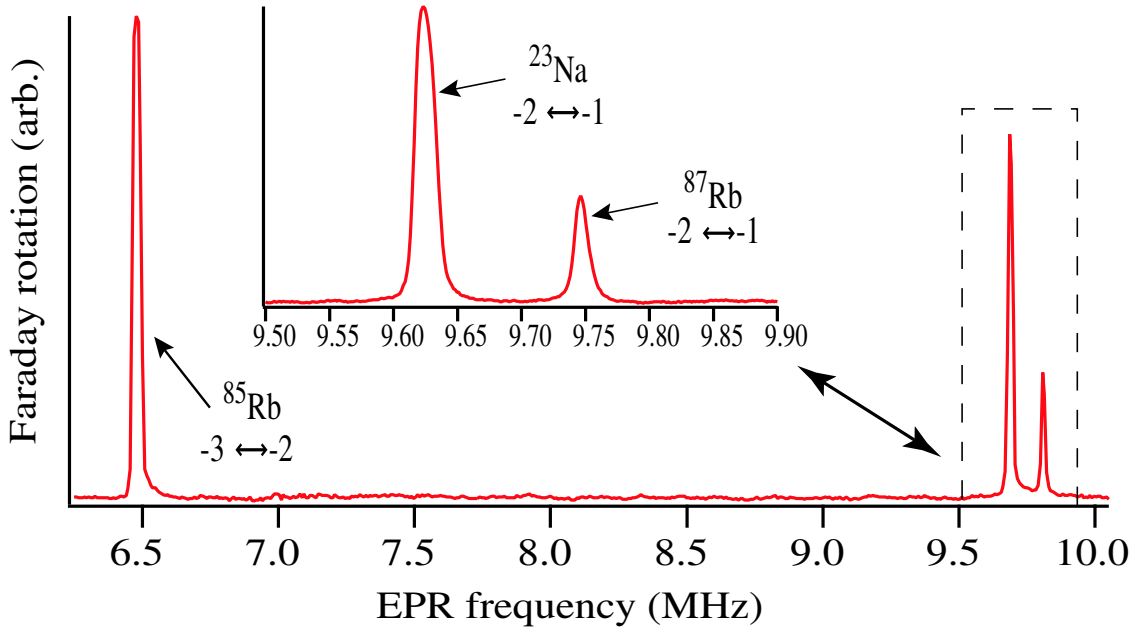

Fig. 6.1: EPR spectrum of ^{23}Na, and ^{87}Rb, the notation $-2 \leftrightarrow -1$ stands for the m $= -2$ to m$' = -1$ transition. Note that if the alkali were not fully polarized the m $= -\mathrm{F}+1 \leftrightarrow \mathrm{m}' = -\mathrm{F}+2$ peaks would be visible. A full description of this is given in [Chann02a].

where ϵ is the magnetic moment correction factor, to be discussed further below, $\mu_K/h = 1.6215$ kHz/G is the magnetic moment of ^{3}He, κ_0 is the frequency shift enhancement factor, μ_B is the Bohr magneton, g_s is the electron g-factor, [He] is the ^{3}He density, $\mathrm{P_{He}}$ is the ^{3}He polarization, and I is the nuclear spin (5/2 for ^{85}Rb and 3/2 for ^{23}Na, ^{39}K or ^{87}Rb). Romalis and Cates [Romalis98] measured the Rb-^{3}He frequency shift enhancement factor, from 120°C to 175°C, to be $\kappa_0 = 6.39 + 0.00934(T - 200°\mathrm{C})$ with a precision of 1.5% for Rb, and Baranga *et al.* [Baranga98] measured the ratios of the K/Rb shifts to be $\kappa_0^K = 0.94\kappa_0^{Rb}$ with a precision of 1%.

The magnetic moment correction factor ϵ arises from the non-linear Zeeman effect. At low fields (<50G) and for the m=-F to m'=-F+1 state used in this work, it is well

approximated by

$$\epsilon = \frac{d\nu/dB|_B}{d\nu/dB|_0} - 1 = \frac{4I\Omega}{(2I+1)\delta\nu_{\rm hfs}} + \frac{6I(2I-1)\Omega^2}{(2I+1)^2\delta\nu_{\rm hfs}^2}, \tag{6.2}$$

where $\Omega = g_s\mu_B B/h$ and $\delta\nu_{\rm hfs}$ is the alkali hyperfine splitting (462 MHz for ^{39}K, 1772 MHz for ^{23}Na, and 6835 MHz for ^{87}Rb; see appendix C). In the experiments described here, we find it necessary to work at a sufficiently high magnetic field that the EPR spectra of the $I = 3/2$ isotopes of Na, K and Rb are well resolved. This necessitates inclusion of the second term of equation 6.2 for accurate polarimetry. Figure 6.2 shows a plot of ϵ verses applied rf frequency. By numerical coincidence, if one keeps the rf frequency constant (i.e. changes B by $F_{^{23}\rm Na}/F_{^{85}\rm Rb} = 2/3$), the correction factors for ^{85}Rb and ^{23}Na are the same to within less than 0.1%. Consequently the ratio of the κ_0's for ^{85}Rb and ^{23}Na can be measured directly without correcting for the magnetic moment.

The Na-Rb cell was 7cm in diameter and made of GE180 glass. It was filled with 2 bar of ^{3}He and 50 torr of N_2, as measured at room temperature. We estimate that approximately 500 mg Na was distilled into it, followed by a trace of Rb, to obtain about a 1:1 Na/Rb ratio in the vapor phase. The procedure for obtaining experimentally desirable alkali ratios in the vapor phase is described in [Babcock03]. Although Na reactions with the glass formed an opaque brown coating in this cell after a few weeks, we were still able to polarize the alkali sufficiently to get ^{3}He polarizations on the order of $40 - 50\%$. The K-Rb cell was 3.5cm in diameter, also constructed of GE180 glass. It was filled with 3.3 bar ^{3}He, 80 torr of N_2, as measured at room temperature, and had roughly a 10:1, K:Rb ratio in the metal phase to obtain approximately a 1.5:1 K:Rb ratio in the vapor phase. In this cell we could obtain as high as $75 - 80\%$ ^{3}He polarization. We also had a twin 3.5cm diameter pure Rb cell that we used for additional Rb frequency shift measurements at temperatures below 200°C.

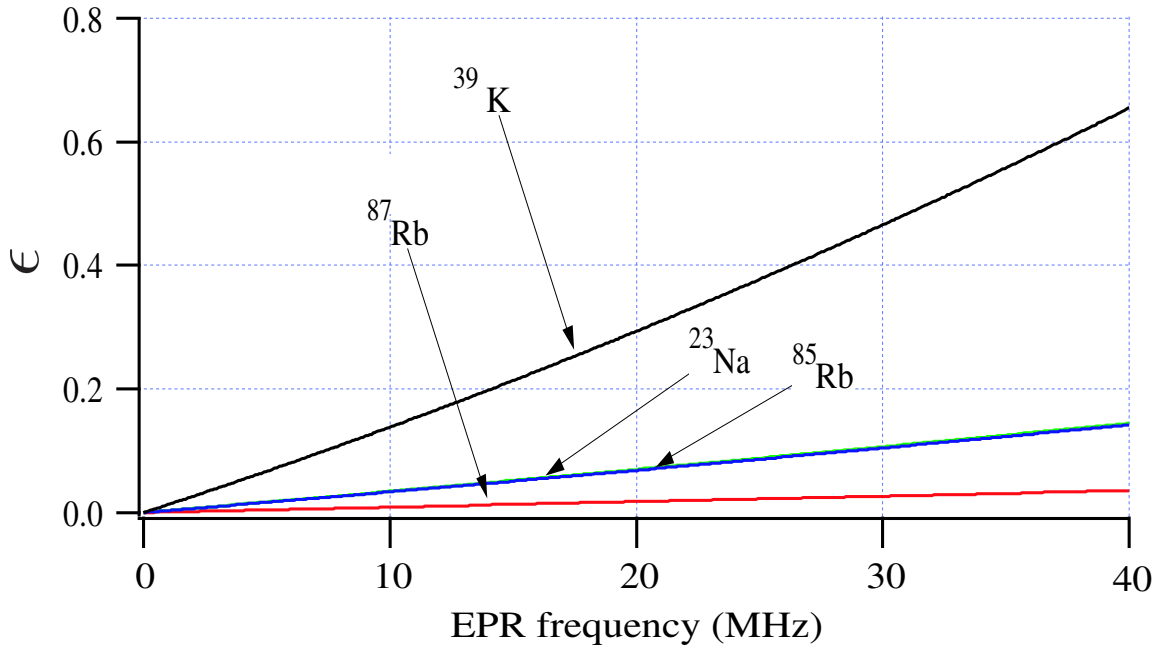

Fig. 6.2: Plot of the magnetic moment correction factor for the various alkali isotopes as a function of the EPR frequency, note that for the special case of ^{85}Rb and ^{23}Na the correction factors follow each other to less than 0.1%.

The procedure for measuring the EPR frequency shifts was given earlier in section 3.6.2.3. The spectra of both alkalis (Na/Rb or K/Rb) were taken in rapid succession for each temperature ,with FID data taken in between. A sample frequency shift data set for ^{85}Rb and ^{41}K is given in figure 6.3. The values of $\Delta\nu_0$ were then normalized using the FID amplitudes taken directly before the respective EPR scan. A sample of the data is shown in figure 6.4.

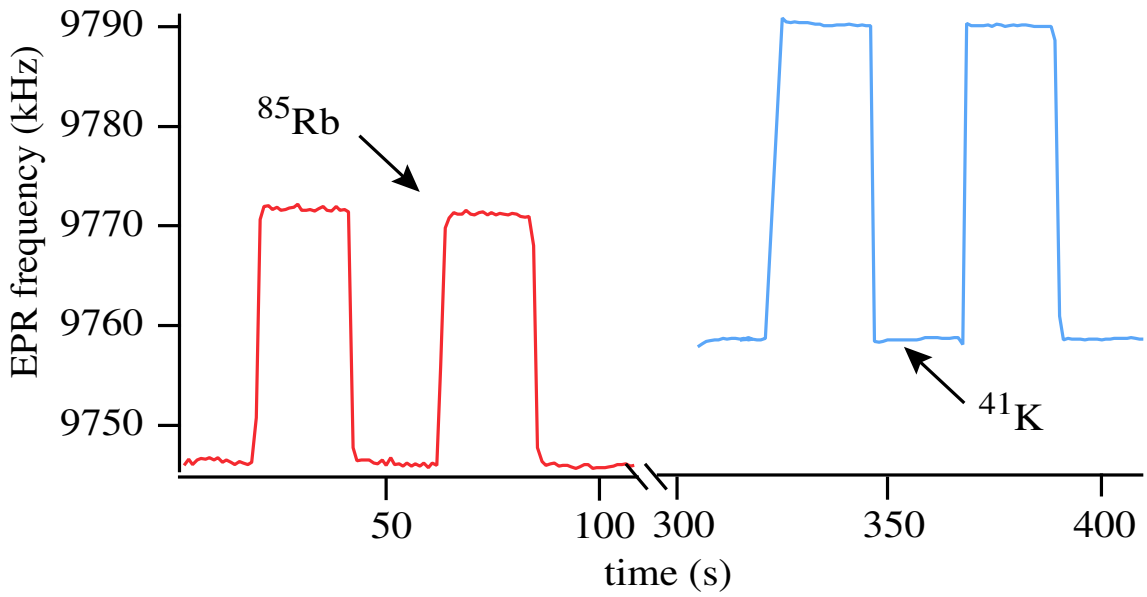

Fig. 6.3: Typical EPR frequency data for a series of four AFP reversals for ^{85}Rb followed by ^{41}K. The break in the graph indicates the pause to take FID data and to change the field from 21G for the Rb data to 14G for the K data.

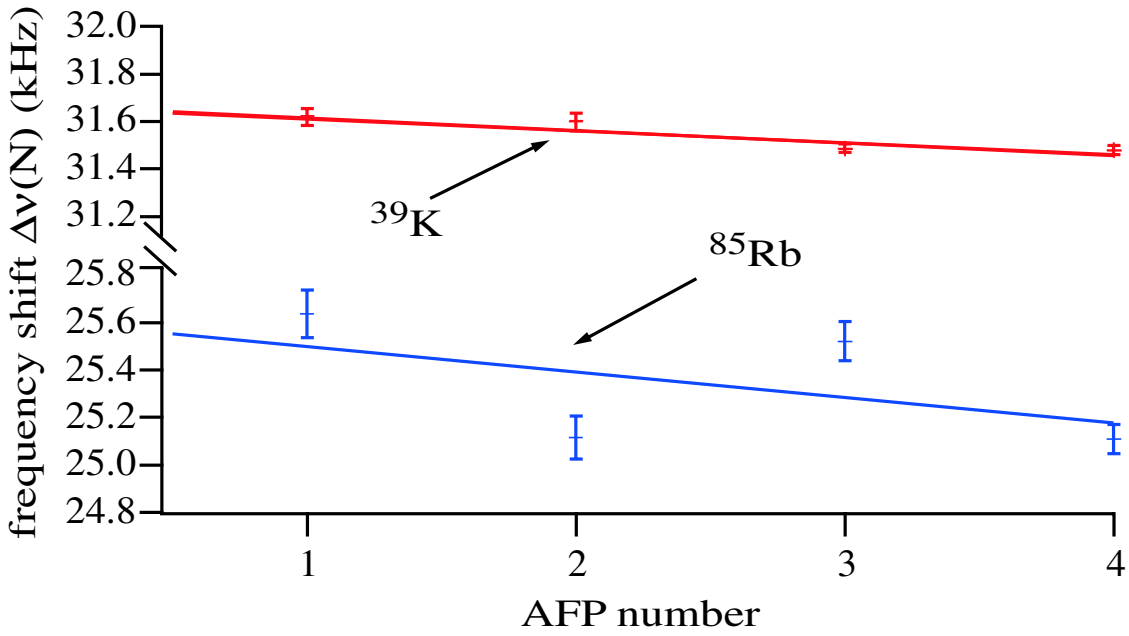

Fig. 6.4: Difference of the adjacent EPR frequencies of the AFP reversals shown in Fig. 6.3 with fits to determine the initial value of the frequency shift $\Delta\nu$. Note that the scatter in the data is caused by field fluctuations.

Tab. 6.1: Ratios of the experimental and theoretical ^{3}He frequency shift enhancement factors. The $100°C$ experimental values are extrapolated from the measured temperature dependance.

	temperature	$\kappa_0^{Na}/\kappa_0^{Rb}$	$\kappa_0^{K}/\kappa_0^{Rb}$
Walker[a] (theory)	$100°C$	0.74	0.97
This work	$100°C$	0.696 ± 0.016	0.938 ± 0.024
This work	$200°C$	0.739 ± 0.007	0.937 ± 0.005
Baranga et al.[b]	$200°C$		0.94 ± 0.01

1 2

Typical values of the measured frequency shifts, $\Delta\nu(N)$, ranged from around 12kHz for the ^{23}Na and 16kHz for the ^{87}Rb in the Na-Rb cell, and 30-60kHz for the ^{39}K and ^{87}Rb in the K-Rb cell. We chose a field high enough that the differential Zeeman splitting of the $I = 3/2$ isotopes was greater than the EPR shifts, and high enough to give adequate resolution of the spectra ($>$ 100kHz). We found a field of 14G, corresponding to an unshifted EPR frequency of 9.8MHz, to be more than adequate. Figure 6.1 shows a typical EPR spectrum for our Na-Rb cell.

In order to measure the temperature dependence of κ_0 for Rb, we first verified that the polarization measurement via the NMR FID amplitude was a temperature independent reference. We placed a high Q FID pickup coil outside of our oven, approximately 2 cm away from the cell, and cooled it so that its temperature remained constant. We then looked for any cell temperature dependance by quickly changing the temperature

1 [a]Reference[Walker89].

2 [b]Reference[Baranga98].

of the cell from 350°C down to 150°C and back up to 350°C in 50°C steps and observing the FID amplitude at each step. This process took a total time of less than 1.5 hours. Note the Na-Rb cell used for this measurement had a ^{3}He wall relaxation time constant of 254 hours, so by polarizing the ^{3}He in this cell to its maximum value and maintaining constant alkali polarization by optical pumping (as monitored via rf spectroscopy), we were able to ensure the ^{3}He polarization did not vary significantly during this measurement. The initial and final FID amplitudes at 350°C were equal within the statistical errors. We determined the FID amplitudes to have a temperature coefficient of $0.0\% \pm 0.5\%$ from $150°C$ to $350°C$, limited by the uncertainty in the NMR pulses themselves.

The absolute temperature of the cell was measured directly with a calibrated optical pyrometer 20 cm above the cell. The optical pyrometer (Exergen model no. Irt/c.10) was calibrated with an Omega WT-J thermocouple, which was temporarily placed on the cell under the same conditions as during optical pumping for the calibration. The thermocouple was removed for the actual optical pumping.

After completing the data set with each cell, we normalized the Rb frequency shifts to the FID amplitudes and fit the result as a function of temperature. We then used the well tested value of κ_0^{Rb} given by [Romalis98] to scale the value of our fit at $170°C$. We note that this calibration automatically compensates for any errors in the ^{3}He polarization introduced by the uncertainty in the ^{3}He density, by solving for the product of all of the constants in equation 6.1.

6.3 Results

Once the Rb frequency shifts were determined over our entire temperature range, we then solved for the frequency shifts for Na and K. We did this by normalizing the Na

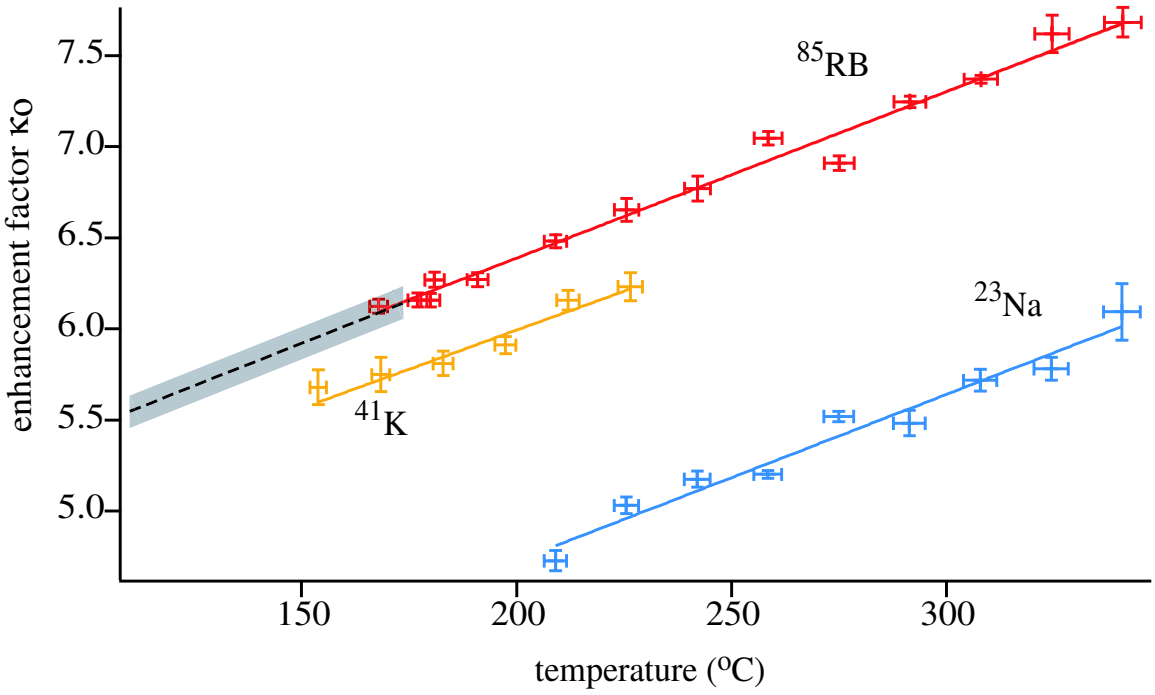

Fig. 6.5: Experimental results for the determination of κ_0 as a function of temperature. The upper line is ^{85}Rb, the middle line is ^{39}K, and the lower line is ^{23}Na. The Dotted line with error (shaded region) is the previous measurement of κ_0 for lower temperatures by Romalis and Cates [Romalis98].

and K shifts to the FID amplitudes, correcting for ϵ and I, and taking the ratios of these shifts to those of the normalized Rb shifts at the same temperature. The data from these measurements are shown in figure 6.5. The fit values for Rb, K and Na from this work are given below.

$$\kappa_0^{Rb} = 6.39 + 0.00914[\mathrm{T} - 200(^\circ\mathrm{C})] \tag{6.3}$$

$$\kappa_0^{K} = 5.99 + 0.0086[\mathrm{T} - 200(^\circ\mathrm{C})] \tag{6.4}$$

$$\kappa_0^{Na} = 4.84 + 0.00914[\mathrm{T} - 200(^\circ\mathrm{C})] \tag{6.5}$$

The fit of the Rb data indicates that the temperature coefficient for κ_0^{Rb} is consistent with the value of [Romalis98] up to $350^\circ C$. Also we note that the values of the ratios

of κ_0^{Na} and κ_0^K to κ_0^{Rb} given in table 6.1 agree very well with the theoretical predictions of [Walker89] at $100°C$, and with prior measurements of [Baranga98] under optical pumping conditions. The values of the EPR frequency shifts for several of the alkali-noble gas pairs have been previously measured [Stoner02, Scheafer89, Romalis98] with results summarized in table 6.2.

Tab. 6.2: Known experimental values of κ_0 and known temperature coefficients, κ_0', with theoretical calculations of Walker [Walker89] at $100°C$. Here the κ_0 for a particular temperature is given by $\kappa_0(\mathrm{T}) = \kappa_0(\mathrm{T_{ref}}) + \kappa_0' \cdot (\mathrm{T} - \mathrm{T_{ref}})$, where the reference temperature of the measurement, $\mathrm{T_{ref}}$, is given in parentheses.

Pair	κ_0	κ_0'	Theory[a]
NaHe[b]	$4.72 \pm 0.09(200°C)$	0.00914 ± 0.00056	6.5
KHe[c]	$6.01 \pm 0.11(200°C)$		8.5
KHe[b]	$5.99 \pm 0.11(200°C)$	0.0086 ± 0.0020	8.5
RbHe[d]	$6.15 \pm 0.09(175°C)$	0.00934 ± 0.00014	8.8
RbHe[b]		0.00916 ± 0.00026	8.8
RbNe[e]	$32.0 \pm 2.9(128°C)$		38
RbKr[f]	$270 \pm 95(90°C)$		280
RbXe[f]	$644 \pm 269(80°C)$		730

3 4 5 6 7

The statistical errors for the values of the κ_0's at 200°C are 1% for ^{23}Na and 0.5% for ^{39}K. The statistical errors in the temperature coefficients, κ_0', are 6% for ^{23}Na, 15% for ^{39}K and 2% for ^{85}Rb. The fractional errors in the temperature dependence are

3 [a]Reference [Walker89].

3 [b]This work.

4 [c]Reference [Baranga98].

5 [d]Reference [Romalis98].

6 [e]Reference [Stoner02].

7 [f]Reference [Scheafer89].

larger for ^{23}Na and ^{39}K for statistical reasons, but since the temperature dependance represents only a small fractional correction to κ_0, the error induced by using these values of κ_0 over the measured temperature range is dominated by the errors in the κ_0's themselves. The errors in the temperature coefficients are provided in order to allow one to estimate the error that would be introduced if one were to extrapolate far beyond the measured temperature range.

The sources of random error are: FID statistical error (0.5%), repeatability of the optical pyrometer (1%) and frequency shift statistical error (1%) which resulted mainly from field fluctuations. Possible systematic errors include the temperature calibration with the thermocouple (0.75%), error in the temperature dependence of the NMR FID amplitudes (0.5%) and calibration to the previous κ_0^{Rb} measurement (1.5%) for a total of 1.8%. An important point about the methods used here is that the absolute ^{3}He polarization and density cancel out in the κ_0 ratio measurements, so no uncertainty arises from these sources.

The cells used in this work were nearly spherical, and κ' was taken to be zero. The diameters of the cells were measured to vary by less than 1mm, thus for the K/Rb cell if one assumed it to be an ellipsoid of revolution the maximum error induced in the measurement of P_{He} would be 1.6%. For the Na/Rb cell this error would be 0.6%. Since our method relies on the measurement of the ratios of the frequency shifts for Na or K to those of Rb in the same cell, the systematic error induced in the measured value of κ_0 by $\kappa' \neq 0$ is suppressed by $(1 - R)\kappa'$ where R is the ratio of κ_0^{K} or κ_0^{Na} to κ_0^{Rb}. Since $R \approx 0.75$ for Na/Rb and $R \approx 0.95$ for K/Rb the induced error in κ_0 from this source becomes negligible.

An additional correction to κ' could also result from the volume of the cell's stem. For both of our cells the volume of the stem was small $< 1\mathrm{cm}^3$ for the Na/Rb cell and $< 0.1\mathrm{cm}^3$ for the K/Rb cell. Approximating the field from the polarized ^{3}He atoms in

the stem as a dipole we obtained an additional correction to $\kappa' \ll 1\%$.

With the increasing interest in alkalis other than Rb for SEOP [Babcock03, Baranga98, Wang03, Borel03], having precision EPR polarimetry will be very important for future developments. In addition, the method used here should be extendable to the important case of ^{129}Xe, where κ_0 and its molecular counterpart κ_1 are only known to 50% accuracy [Scheafer89].

7. LIMITS TO PHOTON EFFICIENCY, LIGHT ABSORPTION IN OPTICAL PUMPING

During the course of these studies on SEOP we have determined that the spin exchange efficiency is limited by imperfect optical pumping [Babcock03] These sources include skewed light, [Chann02a] and off resonant pumping possibly due to absorption by Rb-^{3}He molecules (D_2 pumping). Skewed light is an effect wherein if the axis of the optical pumping light is not exactly collinear with the magnetic holding field, fully polarized alkali-metal vapors will continue to absorb light. This extra absorption is is shown to exceed the ideal case by a factor of $1 + (R/\Gamma)\sin^2\theta$ where R is the optical pumping rate, Γ is the alkali-metal relaxation rate and θ is the angel between the holding field and the axis of the pumping light. Off resonant pumping is an effect caused by the Rb-^{3}He molecular potential, which will be shown to be $P_{3/2}$-like, being resonant with light around the $P_{1/2}$ resonance, causing an effective relaxation. This potential causes off resonant pumping light to be absorbed by Rb-^{3}He pairs effectively relaxing the alkali-metal spin. This effect is observed by a significant narrowing of the resonance of the circular dichroism of the alkali-metal vapor. This effect causes the maximum achievable polarization to decrease to only 90% for a pump laser linewidth of approximately 2 nm, which is the typical specification for un-narrowed diode array bars. On resonance, with a finite pump laser linewidth, this effect can significantly increase the light absorption in an optical pumping cell.

7.1 Skewed Light Effects in Optical Pumping of Dense Atomic Vapors

During optical pumping, circularly polarized light propagating parallel to an applied magnetic field can penetrate deeply through alkali-metal vapors over 100 optical depths thick [Baskar79]. This is possible because the alkali-metal atoms are optically pumped into states that are nearly transparent (i.e. states that cannot absorb light until relaxed by some other mechanism). Imperfect circular polarization of the light is even rapidly attenuated at the front of the cell by the circular dichroism of the alkali-metal vapor.

However, if the light is not perfectly collinear with the magnetic field the alkali-metal electron spins will begin to rapidly precess about magnetic field just like ^{3}He does when its magnetic moment is tipped out of the plane of the applied field. This precession of the Rb spins about the magnetic field causes the time average Rb polarization to be reduced, casing the vapor to continually absorb light even without any relaxation. Even for small propagation angles with respect to the magnetic field, large decreases in the cell transparency can occur.

The propagation of plane light waves through an anisotropic vapor with electric field amplitude $\mathbf{E}$ and propagation vector $\mathbf{k}$ with susceptibility tensor $\overleftrightarrow{\chi}$ is given by,

$$(k^2 - \mathbf{kk}\cdot)\mathbf{E} = k_0^2(1 + 4\pi \overleftrightarrow{\chi} \cdot)\mathbf{E}. \tag{7.1}$$

Where $k_0 = \omega/c$. Since the vapor is dilute (ie. $4\pi\chi \ll 1$) the electric field is transverse. Writing the electric field as the superposition,

$$\mathbf{E} = E_a\hat{a} + E_b\hat{b} \tag{7.2}$$

where $\hat{a} = \hat{z} \times \hat{k}/\sin\theta$ and $\hat{b} = \hat{k} \times \hat{a}$ are the the unit base vectors orthogonal to $\vec{k}$ and θ is the angle between the quantization axis and the propagation vector.

For the conditions in an optically pumped vapor, with alkali-metal polarization P,

the alkali-metal susceptibility can be written as [Happer72, Appelt98],

$$\overleftrightarrow{\chi} = \chi_0(1 - iP\hat{z}\times). \tag{7.3}$$

Using this relation and taking the matrix elements to be,

$$\begin{aligned} \hat{a}\cdot \overleftrightarrow{\chi} \cdot\hat{a} = \hat{b}\cdot \overleftrightarrow{\chi} \cdot\hat{b} = \chi_0, \\ \hat{b}\cdot \overleftrightarrow{\chi} \cdot\hat{a} = -iP\chi_0 \cos\theta. \end{aligned} \tag{7.4}$$

Consequently we find the eigenvectors and eigenvalues of χ are

$$\begin{aligned} \mathbf{e}_\pm &= \frac{\hat{a} \pm i\hat{b}}{\sqrt{2}}, \\ \chi_\pm &= \chi_0(1 \mp P\cos\theta). \end{aligned} \tag{7.5}$$

For a highly polarized vapor $P \simeq 1$, the $\mathbf{e}_-$ mode is rapidly attenuated at the entrance to the cell [Baskar79]. The interior of the cell is primarily in the $\mathbf{e}_+$ mode. We note however that the transparency of this mode is not perfect even for $P = 1$ due the $\cos\theta$ dependance. The attenuation of light will obey,

$$\frac{d\Phi_\theta(\nu)}{d\zeta} = -n\sigma(\nu)\Phi_\theta(\nu)(1 - P\cos\theta). \tag{7.6}$$

Here Φ_θ is the photon spectral flux density (photons/ s cm Hz), ζ is the position along the propagation direction of the light, n is the alkali number density and $\sigma(\nu)$ is the absorption cross section. For $\theta = 0$ one would obtain the propagation condition for the ideal case where absorption goes to 0 in the absence of relaxation.

We now consider how the optical pumping is further affected due to the imperfect polarization of the light along the magnetic field direction. The $\mathbf{e}_+$ light can be resolved into σ^+, π, and σ^- polarization components with respective fractions of light flux given by,

$$f_+ = \cos^4(\theta/2),$$

$$\begin{aligned} f_\pi &= 2\cos^2(\theta/2)\sin^2(\theta/2), \\ f_- &= \sin^4(\theta/2). \end{aligned} \tag{7.7}$$

In steady state the rate at which angular momentum is added to the alkali-metal atoms by depopulation pumping from the $m_s = -1/2$ state must be balanced by the rate at which angular momentum is removed by depopulation pumping from the $m_s = 1/2$ state and by spin relaxation giving,

$$R\left(\frac{f_\pi}{2} + f_+\right)\left(\frac{1}{2} - \frac{P}{2}\right) = R\left(\frac{f_\pi}{2} + f_-\right)\left(\frac{1}{2} + \frac{P}{2}\right) + \frac{\Gamma P}{2}. \tag{7.8}$$

Where $R = \int d\nu\sigma(\nu)\Phi_0(\nu)$ is the pumping rate and Γ is the relaxation rate. Solving for P gives,

$$P = \frac{R(f_+ - f_-)}{R + \Gamma} = \frac{R\cos\theta}{R + \Gamma} \tag{7.9}$$

where we note for the case $\theta = 0$ this gives the expected relation for the alkali polarization given earlier in equation 1.4. Combining this relation with equation 7.6 we obtain

$$\frac{d\Phi_\theta}{d\zeta} = -n\left(\frac{R(R\sin^2\theta + \Gamma)}{R + \Gamma}\right) \tag{7.10}$$

for the propagation of "skewed" light along ζ. Taking the ratio of this relation to the equivalent relation for $\theta = 0$ we find that the extra absorption caused by skewed light is larger than the ideal case by a factor of

$$\Upsilon = 1 + \frac{R\sin^2\theta}{\Gamma}. \tag{7.11}$$

The extra absorption can become significant surprisingly quickly. The pumping rate for a standard 50 W diode array bar, with a 1 THz linewidth for a cell area is can be calculated to be on the order of $R \sim 4.4 \times 10^4$ (see equation 2.3) and a typical relaxation rate for Rb SEOP can be on the order of 500 s^{-1}. This implies $R/\Gamma = 90$, consequently for a skew angle of only 0.11 rad, the light absorption rate at the cell

entrance doubles. Stray fields, improper light collimation, or alignment could easily give skew angles of this size.

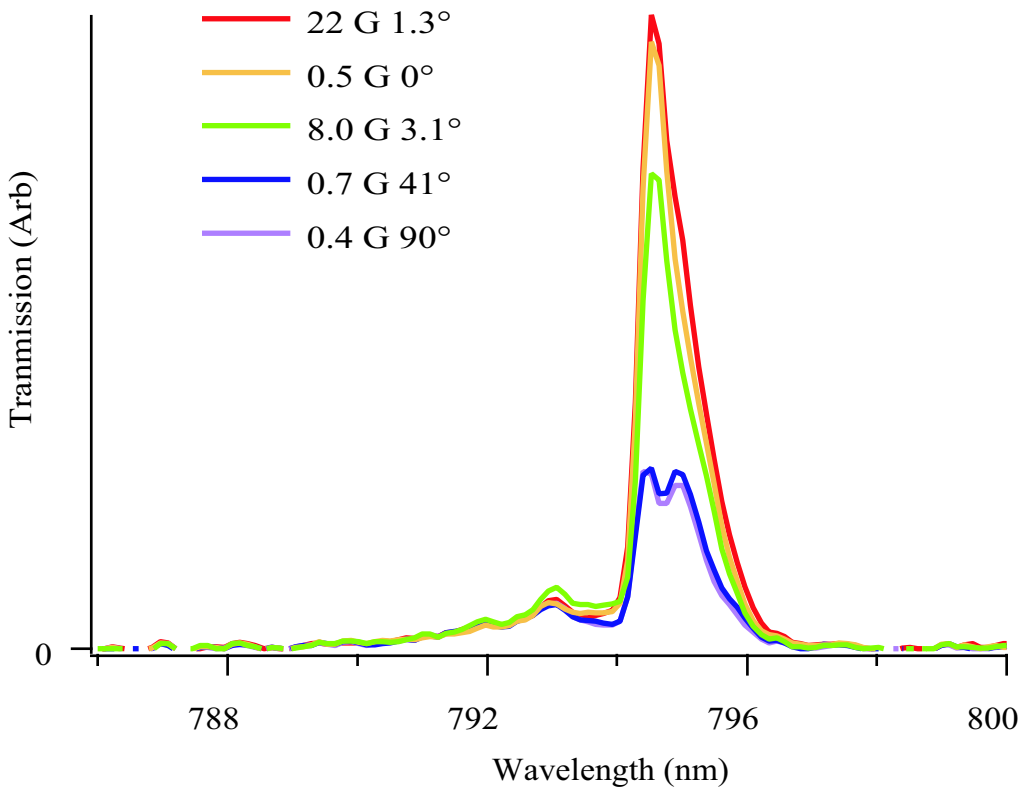

Fig. 7.1: Measured X-factors for a large number of Rb-SEOP cells as a function of 1/ [^{3}He] X[N_2] is plotted vs. 1/ [^{3}He] showing a very slight [^{3}He] dependance.

Another way to look at this effect is to look at the minimum flux density required to polarize a cell of length l which is $\Phi_{0min} = n\Gamma l$. The skew angle increases this amount of light by a factor of Υ, to $nl\Upsilon\Gamma \approx nlR\sin^2\theta \sim nl\sigma\Phi_{0min}\sin^2\theta$. Therefore the absorption doubles at an angle of roughly $1/\sqrt{nl\sigma}$, which can be quite small for a very optically thick sample.

We experimentally illustrate this effect in two ways. First we used a 15 W frequency narrowed diode array bar (linewidth≈ 120 GHz) collimated and sent through the axis of Betty, a 4.9 cm long 4.5 cm diameter cylindrical Rb SEOP cell with flat, optical

windows. The cell was heated to 185°C to give and unpolarized optical depth of $\sim$ 600. We used a low resolution Ocean Optics Inc S2000 spectrometer to record the spectrum of the light transmitted through the cell under various magnetic field conditions. When the magnetic field was was parallel to the propagation direction, we observed high transmission of light which varied little as the field was varied from 0.5 G to 20 G. When the magnetic field angle was rotated by a mere 3.1°, nearly half of the light was attenuated, for larger angles the attenuation became even more severe. Figure 7.1 shows the transmission spectra for a variety of magnetic filed directions from 0° to 90° with respect to the propagation direction of the light.

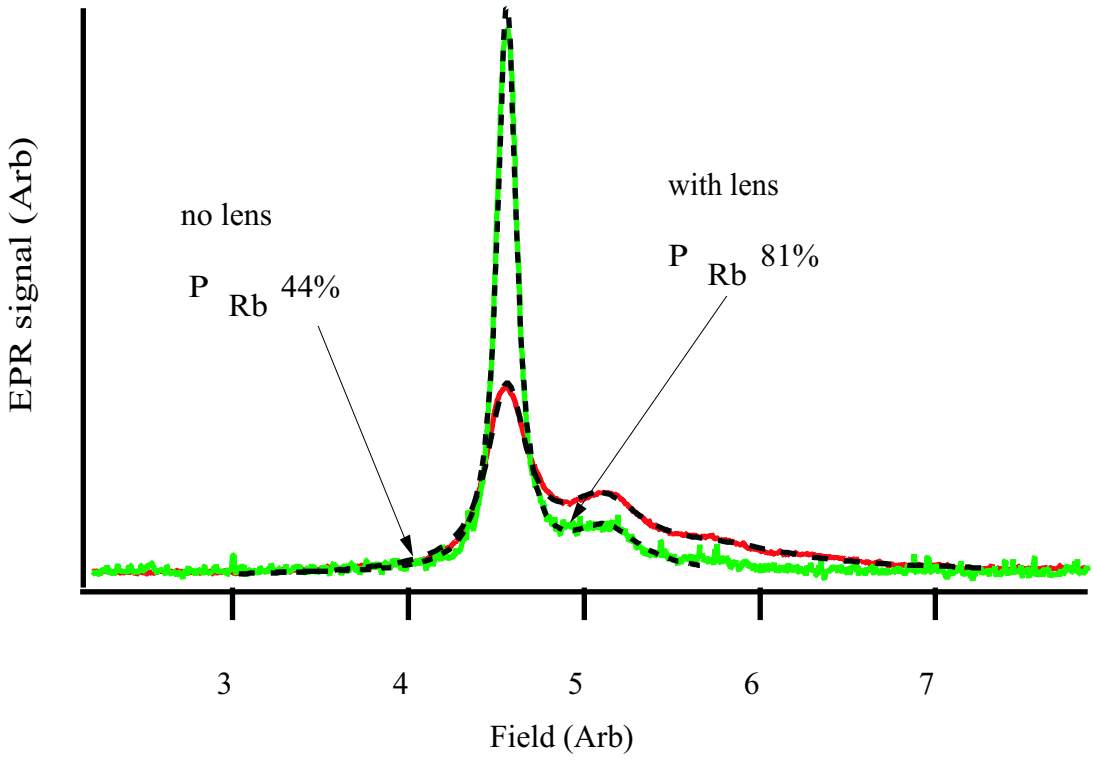

Fig. 7.2: Measured X-factors for a large number of Rb-SEOP cells as a function of S/V. X[^{3}He] [N_2] vs. S/V

For the second illustration of the effect, we show in figure 7.2 how the Rb polarization changes between collimated and un-collimated light. The cell was heated to 200°C,

with an optical depth of over 1000, which nearly fully depleted the 17 W output of the frequency narrowed diode array bar. Using light with a radius of curvature of 75 cm at the front face of the cell gave a Rb polarization of about 45% as deduced using EPR spectroscopy [3.5.1]. The simple addition of a collimating lens increased the measured polarization to 80%.

These results show the importance of careful alignment, and collimation of the optical pumping laser and compensation for stray magnetic fields. Even if the light is properly coupled to the cell, stray fields on the order of the earth's field are capable of significantly increasing the absorption, especially as Γ becomes large at high alkali densities, thus significantly lowering the implied photon efficiency.

7.2 D_2 Pumping and Circular Dichroism of Alkali-Metal-^{3}He Pairs

Even when we have been careful to eliminate skew light effects there is still a large discrepancy between the observed light absorption and the theoretical minimum absorption expected for ideal $P_{1/2}$ optical pumping. This effect was evident in the observed photon efficiencies shown in figure 4.1 for Rb which were a factor 10 lower than the efficiencies predicted for the ideal case, implying an order of magnitude deficit from the expected 100% for the ideal case. Two effects were observed. One, that the maximum attainable alkali-metal polarization for a pure Rb cell was only 91% when using an optical pumping source with a linewidth of 1 THz, whereas for narrower laser sources with linewidths of 0.5 THz or less Rb polarizations of 100% have been obtained, implying a light induced source of relaxation caused by light near the $P_{1/2}$ resonance. Two, the presence of K atoms further decreased the maximum attainable alkali-metal polarization for broadband pumping. The implied light induced relaxation rate was only a factor of three larger than what would be expected from an impact broadened

line shape, but it showed no ^{3}He pressure dependance. This implies the light induced relaxation is not caused merely by mixing of the fine structure from collisional broadening. Results presented here show that in fact absorption to $P_{3/2}$ like Rb-^{3}He molecular potentials can account for this previously observed relaxation.

We begin our analysis by for the moment ignoring $P_{3/2}$ and reviewing the relation for pure $P_{1/2}$ optical pumping which is given by,

$$\left.\frac{d\left\langle F_z\right\rangle}{d\mathrm{t}}\right|_1 = \frac{\mathrm{R}_1}{2}(1 - 2\left\langle S_z\right\rangle) - \Gamma\left\langle S_z\right\rangle . \tag{7.12}$$

Here S_z and F_z are the projections of the electron and nuclear spin along the quantization axis, Γ is the alkali-metal relaxation rate an the 1 subscripts denote D_1 ($P_{1/2}$) pumping with pumping rate R_1. Only the spin-down ground state can be excited by a photon and there is a 50% chance of the atom relaxing back to either spin up or spin down ground states, thus each photon with angular momentum $\hbar$, deposits on average $\hbar/2$ units of angular momentum. The pumping rate is given as [Happer72, Walker97, Appelt98],

$$R_1 = \int_0^\infty \Phi(\nu)\sigma(\nu)d\nu, \tag{7.13}$$

where $\Phi(\nu) = \mathcal{I}(\nu)/h\nu$ is the photon flux density (photons cm^{-2}s^{-1}) and the pressure broadened cross section, σ is will obey,

$$\int d\nu\sigma(\nu) = \pi r_e f c. \tag{7.14}$$

If we assume a pressure broadened Lorentzian line shape with FWHM γ then the cross section becomes,

$$\sigma = \frac{2r_e f c/\gamma}{1 + 4\Delta^2/\gamma^2}, \tag{7.15}$$

where $\Delta = \nu - \nu_0$ and γ has been measured to be 18.7 GHz/amagat with a very slight asymmetry [Romalis97], and the oscillator strength of the D_1 line is 1/3.

Pumping on a D_2 or $P_{3/2}$ line, however, depopulates both spin up and spin down ground state sublevels. The resulting relation for the accumulation of spin due to D_2 pumping, with pumping rate R_2, is given by

$$\left.\frac{d\langle F_z\rangle}{d\mathrm{t}}\right|_2 = \frac{\mathrm{R}_2}{4}\left(\frac{1}{2} - \langle S_z\rangle\right) - \frac{3\mathrm{R}_2}{4}\left(\frac{1}{2} + \langle S_z\rangle\right). \tag{7.16}$$

The total rate of change of F_z by combining equations 7.12 and 7.16 is,

$$\frac{d\langle F_z\rangle}{d\mathrm{t}} = \frac{R_1}{2} - \frac{R_2}{4} - (\Gamma + R_1 + R_2)\langle S_z\rangle. \tag{7.17}$$

This shows that absorption of light by the D_2 line both increases the relaxation rate and reduces the pumping rate. Thus the steady state spin polarization, P, becomes

$$P = 2\langle S_z\rangle = \frac{R_1 - R_2/2}{\Gamma + R_1 + R_2}. \tag{7.18}$$

For pumping light concentrated about the D_1, and obviously detuned from the D_2 line by the fine-structure splitting, using equation 7.15 we find R_2 can be approximated by,

$$R_2 \approx \frac{2r_e f c\gamma}{4\Delta}\Phi, \tag{7.19}$$

which will have a value of,

$$[^3\mathrm{He}]\Phi 9.19 \times 10^{-19}(\mathrm{cm}^2), \tag{7.20}$$

where the ^{3}He pressure, $[^3\mathrm{He}]$ is in atmospheres. Writing this relation as a rate coefficient in terms of the laser intensity in Wcm^{-2} using $R_2 = \kappa_2[^3\mathrm{He}]$ we find,

$$\kappa_2 = \mathcal{I} \times 1.36 \times 10^{-19}\mathrm{cm}^3\mathrm{s}^{-1}. \tag{7.21}$$

Compairing this to the Rb-^{3}He spin relaxation rate coefficient, $\kappa_{SR} = 2.3 \times 10^{-18}$ $\mathrm{cm}^2\mathrm{s}^{-1}$ [Baranga98] we find that for this simple view of D_2 pumping the effect will be negligible for $\mathcal{I} \ll 17\mathrm{Wcm}^{-1}$.

The above assumption of a Lorentzian line shape for the far wings is almost certainly not correct, the far wings being described by a quasistatic lineshape. We make an estimate of the far wing absorption process as a collision and calculating the rate coefficient for excitation in collisions with ^{3}He atoms. If we assume that the absorption occurs at a single interatomic separation, $R(\nu)$, and that the excitation probability is accurately described using standard Landau-Zener theory, we obtain the rate coefficient,

$$\kappa_2 = \frac{8\pi R^2 \hbar \epsilon^2}{|d\delta V/dR|} e^{-V_g(R)/T} \tag{7.22}$$

where $\epsilon = \langle e|e\mathbf{r}\cdot\mathbf{E}|g\rangle/\hbar$ is the Rabi frequency describing the coupling between the light and the colliding atoms, and $\Delta V = V_e - V_g = h\nu$ is the difference of the ground and excited state potential curves at the Condon point. This calculation requires the Born-Oppenheimer approximation which likely fails for He collisions, but is a good starting point.

Using data from Pascale et. al [Pascale76] we obtained the potential curves shown in figure 7.4. Also shown on the plot is the ground state energy, $G_{1/2}$ shifted up by a $S_{1/2} \rightarrow P_{1/2}$ photon energy. We assume here that excitation will primarily occur when an excited state curve crosses the shifted ground state curve. From the potential curves it would appear that the $A_{3/2}$ potential will give the largest contribution to the D_2 pumping rate.

Now we show that the circular dichroism for optical pumping to the A states shows pure $P_{3/2}$ character. In order to calculate dichroism of the Rb-^{3}He molecular potential we need to add the effects the fine structure of the $5P$ state to the potentials of the molecular σ and π states to find the effective Hamiltonian given by

$$\mathcal{H} = \zeta \mathbf{L}\cdot\mathbf{S} + V_\pi L_{z'}^2 - V_\sigma (L_{z'}^2 - 1) \tag{7.23}$$

H mixes states of different J, same m_j in the molecular frame, but for $m_j = 3/2$

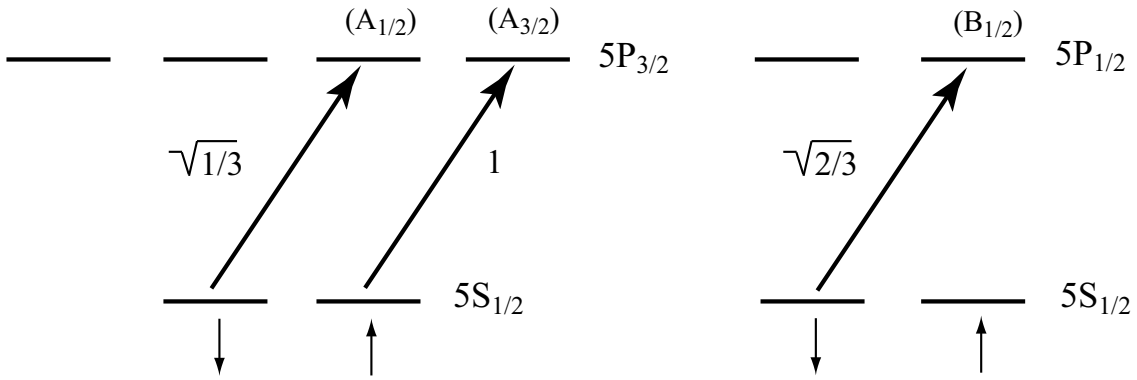

Fig. 7.3: Atomic matrix elements for absorption of σ^+ light by Rb

there is only one matrix element,

$$\langle 3/2, 3/2|\mathcal{H}|1/2, 3/2\rangle = E_{3/2} + V_\pi \tag{7.24}$$

which has pure $P_{3/2}$ character. The $m_j = 1/2$ matrix elements are, using $\Delta = V_\pi - V_\sigma$,

$$\begin{aligned}
\langle 3/2, 1/2|\mathcal{H}_m|1/2, 1/2\rangle &= +\frac{\sqrt{2}}{3}\Delta & (7.25)\\
\langle 3/2, 1/2|\mathcal{H}_m|3/2, 1/2\rangle &= +\frac{-1}{3}\Delta + \frac{2}{3}V_\pi + \frac{1}{3}V_\sigma & (7.26)\\
\langle 1/2, 1/2|\mathcal{H}_m|1/2, 1/2\rangle &= \frac{2}{3}V_\pi + \frac{1}{3}V_\sigma & (7.27)
\end{aligned}$$

giving

$$\mathcal{H}_m = \frac{1}{3}(2V_\pi + V_\sigma) + \begin{pmatrix} E_{3/2} - \frac{1}{3}\Delta & \frac{\sqrt{2}}{3}\Delta \\ \frac{\sqrt{2}}{3}\Delta & E_{1/2} \end{pmatrix}. \tag{7.28}$$

Including the fine structure gives,

$$H = \frac{1}{3}(2V_\pi + V_\sigma) + \frac{E_{3/2} + E_{1/2}}{2} - \frac{\Delta}{6} + \begin{pmatrix} \frac{E_{3/2}-E_{1/2}}{2} - \frac{\Delta}{6} & \frac{\sqrt{2}}{3}\Delta \\ \frac{\sqrt{2}}{3}\Delta & -\left(\frac{E_{3/2}-E_{1/2}}{2}\right) + \frac{\Delta}{6} \end{pmatrix} \tag{7.29}$$

for the full Hamiltonian. Defining $s = E_{3/2} - E_{1/2}$, the eigenvalues of the matrix in 7.29 are

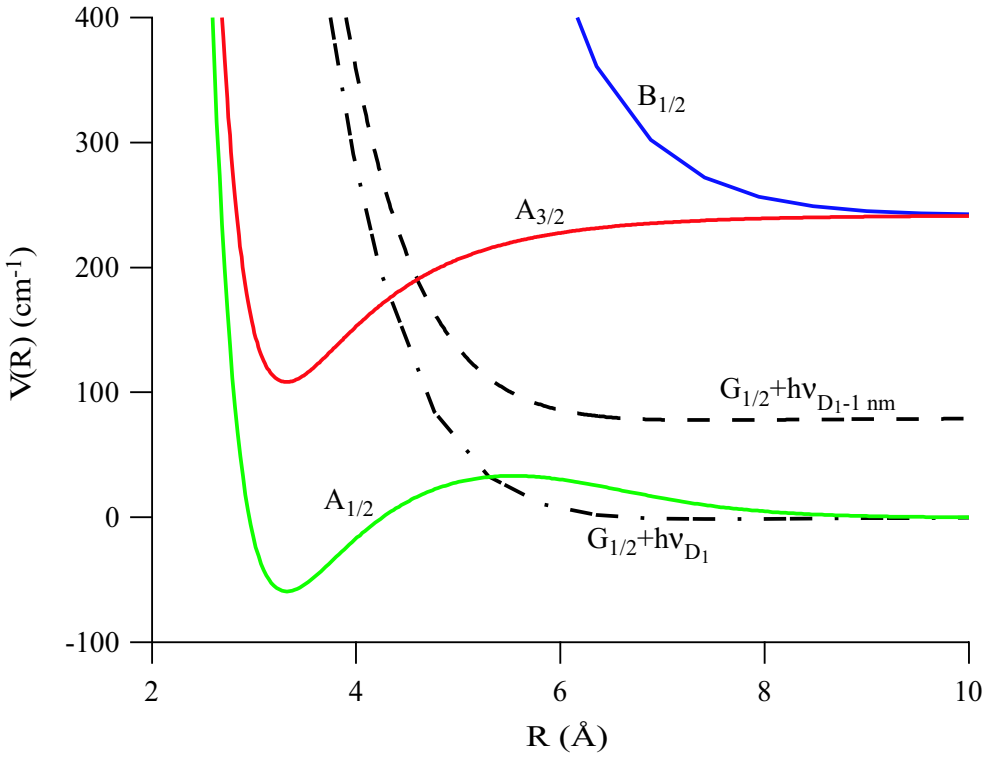

Fig. 7.4: Rb-He potential curves int he fine structure mixing region. The dashed lines are ground potentials ($G_{1/2}$). The upper line has been shifted by a 794 nm photon, the lower one by a 795 nm, $S_{1/2} \rightarrow P_{1/2}$ resonance, photon energy.

$$\lambda = \pm\sqrt{\left(\frac{3}{2} - \frac{\Delta}{6}\right)^2 + \frac{2}{9}\Delta^2}. \tag{7.30}$$

then we get,

$$\Psi_+ = \cos\frac{\alpha}{2}|3/2, 1/2\rangle + \sin\frac{\alpha}{2}|1/2, 1/2\rangle \tag{7.31}$$

and

$$\Psi_- = \cos\frac{\alpha}{2}|1/2, 1/2\rangle + \sin\frac{\alpha}{2}|3/2, 1/2\rangle. \tag{7.32}$$

For $m = -1/2$

$$\langle 3/2, -1/2|\mathcal{H}_m|1/2, -1/2\rangle = -\frac{\sqrt{2}}{3}\Delta \tag{7.33}$$

therefore,

$$\Psi_+ = \cos\frac{\alpha}{2}|3/2,-1/2\rangle - \sin\frac{\alpha}{2}|1/2,-1/2\rangle \tag{7.34}$$

and

$$\Psi_- = \cos\frac{\alpha}{2}|1/2,-1/2\rangle + \sin\frac{\alpha}{2}|3/2,-1/2\rangle. \tag{7.35}$$

Now we look at absorption of σ^+ light to these states. Beginning with the A states where prime denotes molecular frame, for the $\uparrow$ ground state

$$\begin{aligned}\left|\left\langle \frac{3}{2},\frac{3'}{2}\,|r_{+1}|\uparrow\right\rangle\right|^2 &= \left|\left\langle \frac{3}{2},\frac{3'}{2}|\frac{3}{2},\frac{3}{2}\right\rangle\right|^2\left|\left\langle \frac{3}{2}\,|r_{+1}|\uparrow\right\rangle\right|^2 \\ &= \left|D^{\frac{3}{2}}_{\frac{3}{2},\frac{3}{2}}\right|^2\cdot 1 = \cos^6\frac{\theta}{2} \qquad (7.36)\\ \left|\left\langle \frac{3}{2},-\frac{3'}{2}\,|r_{+1}|\uparrow\right\rangle\right|^2 &= \left|D^{\frac{3}{2}}_{\frac{3}{2},-\frac{3}{2}}\right|^2\cdot 1 = \sin^6\frac{\theta}{2} \qquad (7.37)\end{aligned}$$

Therefore the excitation rate out of $\uparrow$ is (taking the angular average),

$$\left\langle \cos^6\frac{\theta}{2}+\sin^6\frac{\theta}{2}\right\rangle = \frac{1}{2}. \tag{7.38}$$

In a similar way for the $\downarrow$ state,

$$\begin{aligned}\left|\left\langle \frac{3}{2},\frac{3'}{2}\,|r_{+1}|\downarrow\right\rangle\right|^2 &= \left|D^{\frac{3}{2}}_{\frac{1}{2},\frac{3}{2}}\right|^2\cdot\left|\left\langle \frac{3}{2},\frac{1'}{2}\,|r_{+1}|\downarrow\right\rangle\right|^2 \\ &= 3\sin^2\frac{\theta}{2}\cos^4\frac{\theta}{2}\cdot\frac{1}{3} \\ \left|\left\langle \frac{3}{2},-\frac{3'}{2}\,|r_{+1}|\downarrow\right\rangle\right|^2 &= 3\sin^4\frac{\theta}{2}\cos^2\frac{\theta}{2}\cdot\frac{1}{3} \qquad (7.39)\end{aligned}$$

so the excitation rate out of $\downarrow$ is,

$$\frac{1}{3}\left\langle 3\sin^2\frac{\theta}{2}\cos^4\frac{\theta}{2}+3\cos^2\frac{\theta}{2}\sin^4\frac{\theta}{2}\right\rangle = \frac{1}{3}\cdot\frac{1}{2}=\frac{1}{6}. \tag{7.40}$$

Consequently these states have the same form for the circular dichroism as a $P_{3/2}$ state, where the pumping rate out of the $\downarrow$ state is given by,

$$R\downarrow = \frac{1}{3}R\uparrow \Rightarrow P_\infty = \frac{R_\downarrow - R_\uparrow}{R\downarrow + R\uparrow} = -\frac{1}{2}. \tag{7.41}$$

This result tells us that we should expect to a higher pumping rate to the collisionally mixed D_2 line than one would expect for pure atomic dichroism.

7.2.1 Experiment

As was shown above, in equation 7.18, absorption to a D_2 potential will both increase the relaxation rate and and decrease the pumping rate. With the resulting alkali polarization given by

$$P = 2\langle S_z \rangle = \frac{R_1 - R_2/2}{\Gamma + R_1 + R_2}. \tag{7.42}$$

were we can replace $R_1 + R_2$ by the new effective pumping rate, R_eff. The maximum achievable alkali polarization for infinite pumping power, P_∞, is

$$P_\infty = \frac{(R - R'/2)}{R_{\text{eff}}}. \tag{7.43}$$

As a result the new build up of polarization and corresponding absorption becomes,

$$\frac{d(sP)}{dt} = R_{\text{eff}}(P_\infty - P) \tag{7.44}$$

$$A = R_{\text{eff}}(1 - P_\infty P) \tag{7.45}$$

So the general case of optical pumping with circularly polarized light can be parameterized in terms of numbers R_{eff} and P_∞. Adding alkali-metal relaxation to this relation we get the expected relation,

$$P = P_\infty \frac{R_{\text{eff}}}{R_{\text{eff}} + \Gamma}. \tag{7.46}$$

This equation is the basis for our measurements of the circular dichroism. We will simply measure P_∞ as a function of wavelength. We adjust the temperature on our oven to approximately $190°C$, corresponding to an alkali-metal density $\sim 6 \times 10^{14}\text{cm}^{-3}$. We then measure the polarization Faraday rotation with our FNDAB tuned to the D_1 resonance where we achieve 100% alkali polarization as verified by EPR spectroscopy. We then detune the laser from resonance and measure the value of the polarization faraday rotation, while chopping the pump beam with a Unabliz VS014 shutter. This gives data qualitatively very similar to that of the standard relaxation data described

in section 3.5.3, however, the amplitude of the signal, calibrated to the voltage for the $P_A = 100\%$ signal on resonance, gives us the value of P_A. Further we can obtain both the initial pumping rate, R_{eff} from the initial slope of the pump up transients when the light is chopped on, and Γ from the exponential decay when the pump light is chopped off. Knowing these three values allows up to calculate P_∞ for that particular pump wavelength.

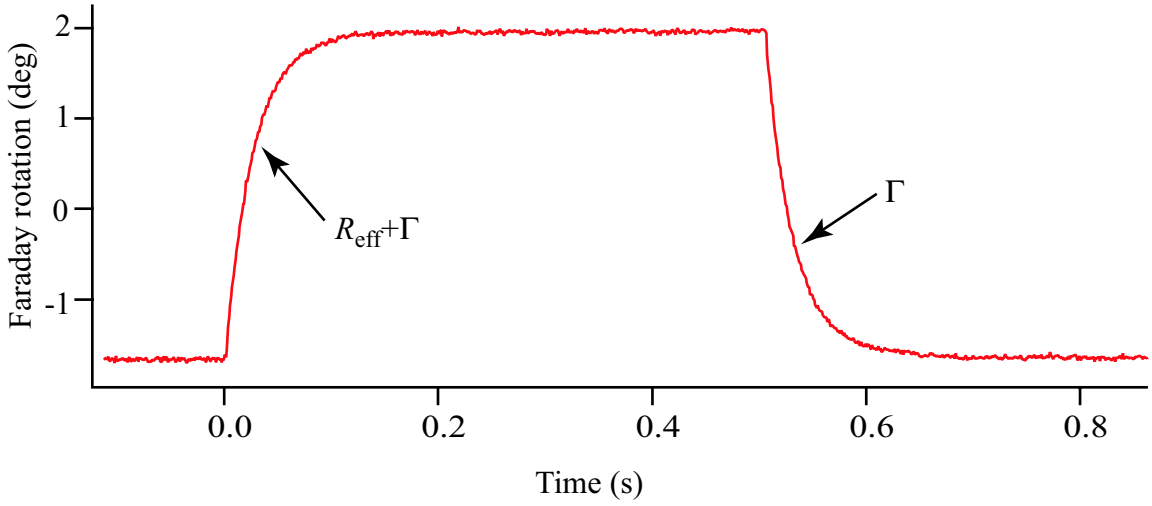

Fig. 7.5: Transients for determining P_A, R_{eff}, and Γ

.

We take data using two separate conductively cooled FNDAB's, one with a free running wavelength of 794 nm at room temperature and another with a free running wavelength of 800 nm at room temperature. With these two DAB's narrowed by our FNDAB cavity, we are able to access wavelengths from 782 nm to 810 nm by temperature control from $-20°C$ to $45°C$ using a water cooled TEC DAB mount and recirculating chiller. A sample of the pumping/relaxation transients is shown in figure 7.5 Since for the measured rates, γ, will be $\Gamma = \gamma s$ where Γ is the true relaxation rate, and s is the slowing down factor which is a non-linear function of polarization we only fit to the data were $P_A \ll 5\%$ and is therefore represented well by a constant s=10.8

for natural abundance Rb [Kadlecek00].

Results of this data are shown in figure 7.6. The dotted line represents the calculated $P_\infty(\lambda)$ for pure D_1 pumping, and the solid line is a fit accounting for the D_2 pumping effects. Given the width of the data in this fit, it easily accounts for the observed $P_A = 91\%$ when using a 2 nm wide broadband laser source. This data clearly demonstrates the gains to be achieved by using FNDAB's for which the linewidth can be as low as 0.14 nm.

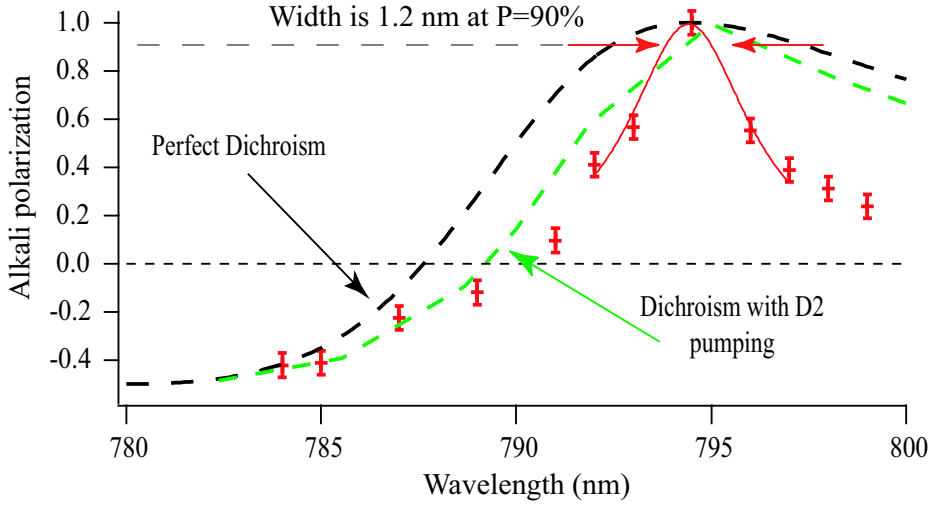

Fig. 7.6: P_∞ as a function of pump laser wavelength. The dotted line is the what one would expect for perfect circular dichroism without D_2 pumping, the smooth line is a fit including excess absorption.

8. LIMITS TO OBSERVED ^{3}He POLARIZATION, THE X-FACTOR

8.1 Introduction

In all SEOP cells we (and other groups) have tested the ^{3}He polarization saturates at a value of 20% to 50% below that of the measured alkali-metal polarization. In all respects this limit to the ^{3}He relaxation behaves as if there exists an additional strongly temperature dependent source of ^{3}He relaxation. In all cases the measured P_{He} is equal to the spin exchange rate (κ_{SE}[Rb]) divided by the measured spin-relaxation rate at the same alkali-metal density to within errors of typically a few percent. This is precisely what we would expect from a standard rate balance argument, however the source of the extra relaxation was unknown. We have studied this apparent extra source of ^{3}He relaxation at great length and have found the relaxation to vary from 10% to over 100% of the spin exchange rate depending on the cell tested. We postulate three possible sources of the extra relaxation mechanism. If the extra relaxation were simply caused by strongly temperature dependant interactions with the walls of the SEOP cells, then one would expect the relaxation to be proportional to the surface to volume ratio of the cell. Second, if the extra relaxation is a bulk effect, the extra relaxation should be independent of the cell parameters, but show dependance on gas/vapor composition. Third and lastly if the extra relaxation is a fundamental property of the ^{3}He -Rb interactions, such as anisotropic spin exchange [Walter98], it would be independent of all of these parameters, but depend on the alkali metal used. In this paper we explore

each of these possibilities. We present evidence from studies to show that the extra relaxation is dependant on S/V but also the N_2 and ^{3}He pressure in the cell.

8.2 Theory

In SEOP spin angular momentum is first deposited into the valence electrons of an alkali atom, usually Rb through optical pumping. Through binary collisions with ^{3}He the spin polarized electrons then transfer angular momentum to the nuclei of the ^{3}He. The gain of polarization of the ^{3}He, P_{He}, in SEOP follows a simple rate balance equation given by,

$$\frac{dP_{He}}{dt} = \kappa_{se}[\mathrm{Rb}](P_{\mathrm{Rb}} - P_{He}) - \Gamma_{\mathrm{He}}P_{He}. \tag{8.1}$$

Here [Rb] is the Rb density, P_{Rb} is the Rb polarization, Γ_{He} is the combined ^{3}He relaxation induced by the wall of the SEOP cell and possible magnetic field gradients at room temperature ([Rb] $\simeq 0$), and κ_{SE} is the spin exchange rate coefficient. If we solve the above relation in the steady state for the achieved P_{He} we obtain,

$$P_{\mathrm{He}} = \frac{\kappa_{se}[\mathrm{Rb}]}{1/\tau_{up}} \langle P_{\mathrm{Rb}} \rangle \tag{8.2}$$

where $\langle P_{\mathrm{Rb}} \rangle$, is the volume averaged Rb polarization, and $1/\tau_{up}$ is the total ^{3}He relaxation rate which is $T1$, the time constant for the gain of ^{3}He polarization during SEOP given by,

$$\frac{1}{\tau_{up}} = \kappa_{\mathrm{SE}}[\mathrm{Rb}] + \Gamma_{\mathrm{He}}. \tag{8.3}$$

κ_{SE} has been measured to be $6.8(\pm 0.1) \times 10^{-20}$, and we have measured $\langle P_{\mathrm{Rb}} \rangle$ and found it to be 1 under nearly all conditions for this experiment. Γ_{He} is the sum of wall relaxation, magnetic field gradient relaxation and relaxation caused by the ^{3}He self relaxation.

For the limit of cells with $\Gamma_{\mathrm{He}} \ll \kappa_{SE}[\mathrm{Rb}]$ one would expect P_{He} to reach parity with P_{Rb}. We experimentally find this not to be the case. P_{He} is always less than P_{Rb} by some factor. But if we simply take the ratio of the measured quantities in equation 8.2 we find that the relation given is correct and accurately predicts the achievable P_{He} for a given cell. P_{He} can then be verified by measuring the absolute P_{He} using the EPR frequency shifts of the Rb resonance due to the polarizied ^{3}He (section 3.6). The measured P_{He} agrees with the predicted polarization within the combined errors (typically less than 5%) of the [Rb], τup and P_{He} measurements themselves. By all properties this unknown factor acts as an extra source of ^{3}He relaxation that scales in some way with cell temperature much as [Rb]. Consequently, will define this extra relaxation source, χ, with the same units as κ_{SE} such that it can be added onto the κ_{SE} in the denominator of eq. 8.2 to obtain,

$$\kappa_{se}(1+\chi) = \frac{d\Gamma_{\mathrm{He}}}{d[\mathrm{Rb}]}. \tag{8.4}$$

With this modification Eq. 8.3 becomes,

$$\frac{1}{\tau_{up}} = \Gamma_{\mathrm{He}} + \kappa_{se}[\mathrm{Rb}] + \int \kappa_{se}\chi d[\mathrm{Rb}]. \tag{8.5}$$

Now the resulting maximum P_{He} attainable in the limit where Γ_{He} becomes negligible will be,

$$P_{\mathrm{He}} = \frac{1}{1+\frac{1}{[\mathrm{Rb}]}\int \chi d[\mathrm{Rb}]} = \frac{1}{1+\mathrm{X}}, \tag{8.6}$$

where we have replaced the quantity $\frac{1}{[\mathrm{Rb}]}\int \chi d[\mathrm{Rb}]$ by X for convenience.

The source of this extra ^{3}He relaxation could conceivably take three possible forms. These are: an additional temperature or Rb density dependant wall relaxation mechanism, an additional gas phase collisional ^{3}He relaxation process perhaps involving molecular interactions, or an anisotropic spin-exchange [Walter98] rate much larger than theoretically expected. However the anisotropic spin exchange hypothesis appears to be precluded because of several observations to be disused latter.

The relations above give two methods to measure the X factor. One method is to simply measure τ_{up} as a function of Rb density. By inspection of equations 8.4 and 8.5, one can see that this method should immediately provide both the value of χ and its functional dependance given that κ_{se} is known from independent methods [Baranga98, Chann02b].

Another method is to measure X is to measure P_{He} as a function of Rb density. By taking the inverse of the relation for P_{He} we obtain,

$$\frac{1}{P_{\mathrm{He}}} = 1 + X + \frac{\Gamma_{\mathrm{He}}}{\kappa_{se}[\mathrm{Rb}],} \tag{8.7}$$

where all of the quantities other than X as defined in equation 8.6 are either directly measurable or known.

Given the large statistical variations in the wall relaxation times of even good SEOP cells and that Γ_{He} in these cells can change by application of high magnetic fields [Jacob04], it is apparent that surface interactions with the SEOP cell walls play a large role in ^{3}He relaxation. A temperature dependant ^{3}He -cell surface interaction could account for the observed X-factor. Therefore we began by analyzing the X-factor for a large number of widely varied cells (listed in table 3.2) as a function of the cell's surface to volume ratio or S/V. Figure 8.1 shows the measured X-factors for all of the cells we have tested. While the trend in this data is not immediately apparent, we point out that the only control variable in this graph is S/V, all the other parameters including cell construction/preparation technique, ^{3}He and N_2 density are widely varied from one cell to the next. The data does seems to suggest an S/V dependance but does not preclude the possibility of the dependance on other parameters. Further, given the large statistical variations in Γ_{He} caused by differing surface effects from one cell to the next, it is reasonable to expect a similar degree of scatter in possible temperature dependant surface interactions. Therefore we began to postulate and explore other

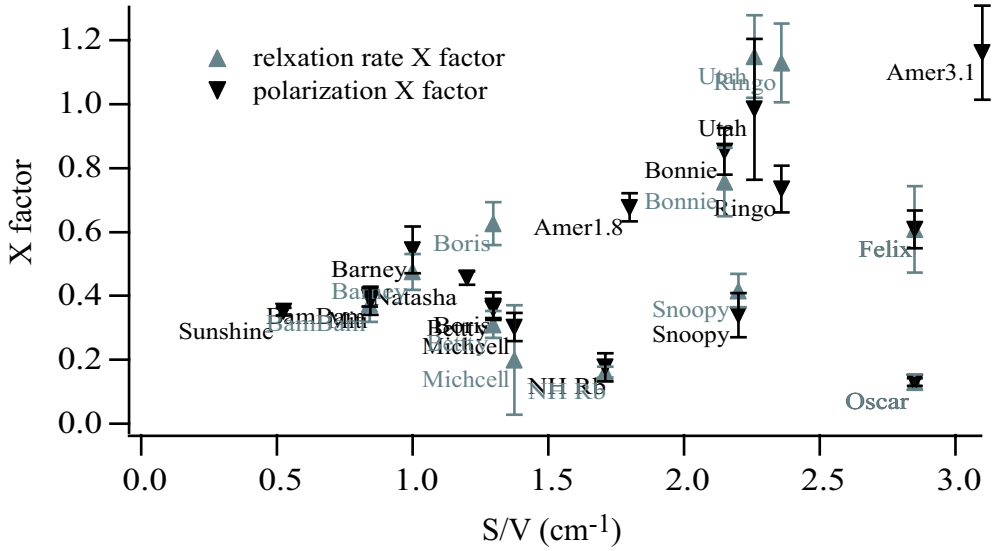

Fig. 8.1: Measured X-factors for a large number of Rb-SEOP cells as a function of S/V. Upward pointing triangles are the data from the relaxation method and downward pointing triangles are data from the polarization method.

functional dependencies.

If X were in part caused by additional non-binary collisional relaxation mechanisms it should show dependance on the gas pressure or composition. It has been shown that Rb_2 molecules can exist at much higher buffer gas pressures than expected [Chann03b, Kadlecek00]. Since a Rb triplet molecule is unpolarized, interactions with ^{3}He would cause nuclear spin relaxation of the ^{3}He with a characteristic [Rb]^2 dependance. However if Rb molecules, or other molecular ^{3}He relaxation processes, did exist in SEOP cells under optical pumping conditions they should be broken up through third body collisions with buffer gas. Plots of X vs. $1/[N_2]$ or $1/[^3He\ ]$ would show a characteristic dependance.

Here we note that higher gas pressures will shorten the achievable wall relaxation time constants due to increasing binary relaxation rates. The contribution to Γ_{wall} from intrinsic dipole-dipole limited ^{3}He -^{3}He relaxation is (744h/amagat) [Newbury93]

and the N_2-^{3}He is expected to be similar order of magnitude due to the nuclear spin of N. Further, direct measurements in our lab can put a lower limit of ~ 200 (h/amagat) on the N_2-^{3}He relaxation based on the room temperature relaxation rate measured for the cell named Lion. Consequently, to achieve any possible gains in ^{3}He by lowering X in this way, one would have to compensate for the higher ^{3}He wall relaxation rates by using higher spin exchange rates (ie. use higher alkali-metal density while maintaining $P_{\mathrm{A}} = 1$).

Lastly, the X-factor could in part originate from anisotropic spin-exchange, however as we have discussed previously this contribution should be small [Walter98]. But if some of this extra relaxation did come from anisotropic spin exchange it would add differently in the numerator and denominator of eq. 8.2. Our measured κ_{SE} using either the rate balance or the repolarization methods (described in chapter 5) would be,

$$\kappa_{\mathrm{SE}}^{meas.} = \kappa_{\mathrm{SE}} - \frac{\kappa_{an.}}{2} \tag{8.8}$$

where $\kappa_{an.}$ is the anisotropic spin exchange rate, which polarizes the ^{3}He atoms in the opposite direction to the spin exchange term κ_{SE}. Whereas the total relaxation rate, Γ_{He}, becomes,

$$\frac{1}{\tau_{up}} = (\kappa_{\mathrm{SE}} + \kappa_{an.})[\mathrm{Rb}] + \Gamma_{\mathrm{He}} = \left(\kappa_{\mathrm{SE}}^{\mathrm{meas.}} + \frac{3}{2}\kappa_{\mathrm{an.}}\right)[\mathrm{Rb}] + \Gamma_{\mathrm{He}} \tag{8.9}$$

Substituting these relations into eq. 8.2 and taking the limit as $\Gamma_{wall} \to 0$ we obtain,

$$P_{\mathrm{He}} = \frac{\kappa_{\mathrm{SE}}^{meas.}}{\kappa_{\mathrm{SE}}^{meas.} + \frac{3}{2}\kappa_{an.}}. \tag{8.10}$$

Therefore $\frac{3}{2}\kappa_{an.}$ would be the measured value of X. However a X-factor entirely from this source would show no dependence on cell parameters. However we point out that if X were a combination of any of the above described possibilities, the intercepts of the X-factor vs. any dependant parameter would give the value of $\kappa_{an.}$.

8.3 Measurements

Initially, to find clues into the origin of the X-factor, we looked for a S/V wall relaxation dependence. Thus we measured the X-factor in the two ways described above for as many different cells as possible. Initially we were very concerned about the functional dependance of the alkali metal density on X. Therefore we measured the ^{3}He relaxation rate as a function of alkali-metal density for a large number of points with the cell named Betty.

The first method to measure the X-factor, which we call the "relaxation rate method," is based on rewriting equation 8.4 in terms of X, which we have determined is linear with [Rb], as,

$$\frac{1}{\tau_{up}} = (\kappa_{\mathrm{SE}} + X)[\mathrm{Rb}] + \Gamma_{\mathrm{He}}. \tag{8.11}$$

Each of these quantities was measured as follows: τ_{up} was measured using the time rate of increase of our NMR FID signal during optical pumping, the Rb density was measured using polarization Faraday rotation, and the alkali-metal polarization was monitored using EPR spectroscopy. Each of these methods were described previously in section 3.5. We measured all of the cells listed in table 3.2 using this technique. For the cell Betty we performed additional more extensive tests. Points were taken with both frequency narrowed diode array bars and with un-narrowed DAB sources to confirm there was no dependence on the pump laser spectral properties. As a further check some points were taken "in the dark" by measuring the Γ_{He} again using NMR FID with the pump laser off. For these points [Rb] was measured using the field Faraday rotation technique (section 3.5). This resulted in the linear [Rb] dependance shown in figure 8.2.

Next we deduced X using the method given by equation 8.7. for all of our cells for which we had accurate ^{3}He polarization data. We call this method the "polarization

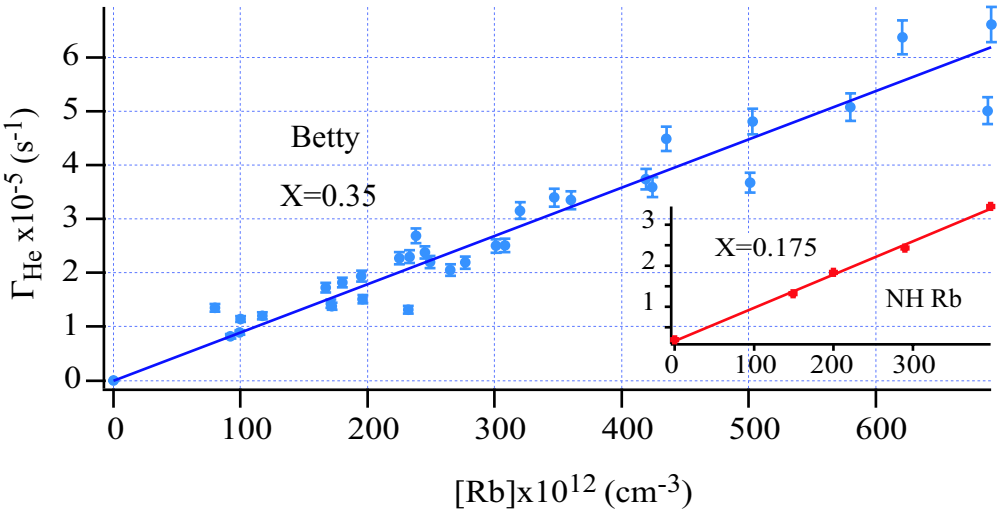

Fig. 8.2: Γ_{He} as a function of [Rb] for an extensive number of points for Betty. The Dependance for this cell, as with all others measured, was linear to within error bars of typically 5% or less. The inset is data for NH Rb showing a typical data set for the remainder of the cells we tested.

X-factor method". Here, P_{He} was measured using the EPR frequency shift method described in section 3.6 and [Rb] was again measured using polarization Faraday rotation and Rb EPR polarimetry (section 3.5). $1/P_{He}$ was plotted vs. $1/[Rb]$, the y-intercept of a linear fit then gives $1 + X$, note the slope can be held to $\Gamma_{wall}/\kappa_{SE}$. Typical data for this method for the "NH Rb" cell is shown in figure 8.7. For some cells we did not have P_{He} data for multiple data points so for these cells we simply used equation 8.7 to calculate X.

Again figure 8.1 shows the data for all of the cells we measured using both of these methods, showing good agreement between the two methods. We initially searched for pre-existing SEOP cells with extreme parameters from our good friends at NIST, University of Utah, and University of New Hampshire to further explore the X-factor. Many of the cells tested were in the S/V= $1 \rightarrow 2$ range, thus Amersham Health was kind enough to construct a set of cells to allow us to explore the X-factor at very high

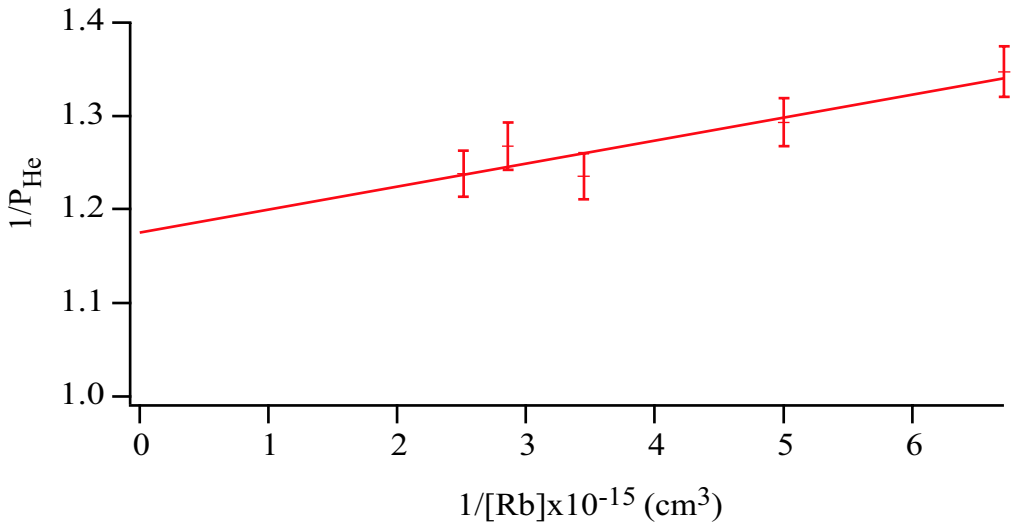

Fig. 8.3: Sample of data to determine the X-factor using the polarization method. The data from this method agrees very well with data obtained using the relaxation rate method. The data shown is for the cell NH Rb which had one of the lower X-factors of the cells we tested. X=0.17 for both methods.

and intermediate S/V. S/V was 3.1 cm^{-1} and 1.8 cm^{-1} respectively for these cells (named Amer1.8 and Amer3.1) with all other parameters such as ^{3}He and N_2 density, construction and filling techniques held constant. Further intuitions derived from the differences observed in X for certain cells from New Hampshire (named NH Rb) and NIST (cells named Oscar and Felix) lead us to explore the X-factor dependance on the gas composition. NIST was gracious enough to construct 3 special cells (named Scarecrow, Lion, and Tin Man) for us to allow exploration of gas composition dependance. These cells were again all constructed and prepared in the same way, at the same time, with the same glass and S/V. Each of these cells was then filled with approximately 0.5 amagats of ^{3}He and N_2 pressures of 50 torr, 150 torr and 300 torr for Scarecrow, Lion and Tin Man respectively. These cells allowed us to obtain much needed data at relatively low ^{3}He pressure, as well as to systematically explore a hypothesis of a large

N_2 pressure dependance because of results of low X-factors for NH Rb, with 98 torr of N_2, and Oscar with 175 torr N_2 which was higher than the more commonly used 50 torr of N_2.

We first note here that cells with flat optical windows attached to a cylindrical body such as Betty, BamBam, Amer3.1 and Amer1.8 seemed to follow slightly different trends and will be analyzed separately. First we consider our vast number of cells which were made out of one piece blown GE180 glass bodies.

We plotted all of our data assuming possible dependencies on S/V, $1/N_2$, and $1/^3$He by normalizing the measured X factors to two of these parameters at a time, and plotting the normalized result against the third variable. The following graphs of $X[^3\text{He}][N_2]$ vs S/V, $X[^3\text{He}]/(S/V)$ vs $[N_2]$, and $X[N_2]/(S/V)$ vs $[^3\text{He}]$ show our results for blown GE180 glass cells.

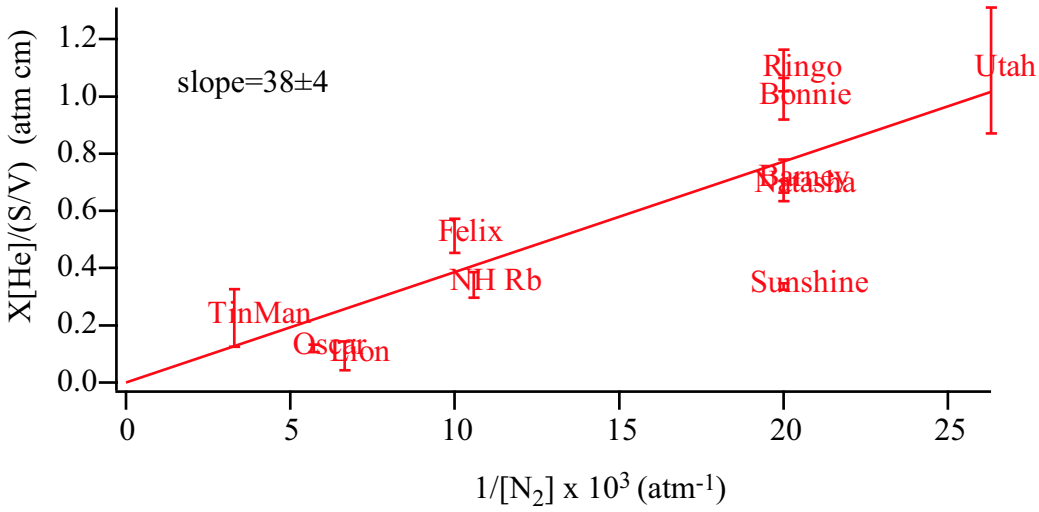

Fig. 8.4: Measured X-factors for a large number of Rb-SEOP cells as a function of $1/[N_2]$. $X[^3\text{He}](S/V)$ is plotted vs. $1/[N_2]$ showing a stong $[N_2]$ dependance.

Figures 8.4, 8.5, and 8.6 show X is dependant on all three of these parameters. Further if we normalize X by all three of these by taking, $X[^3\text{He}][N_2]/(S/V)$, we get

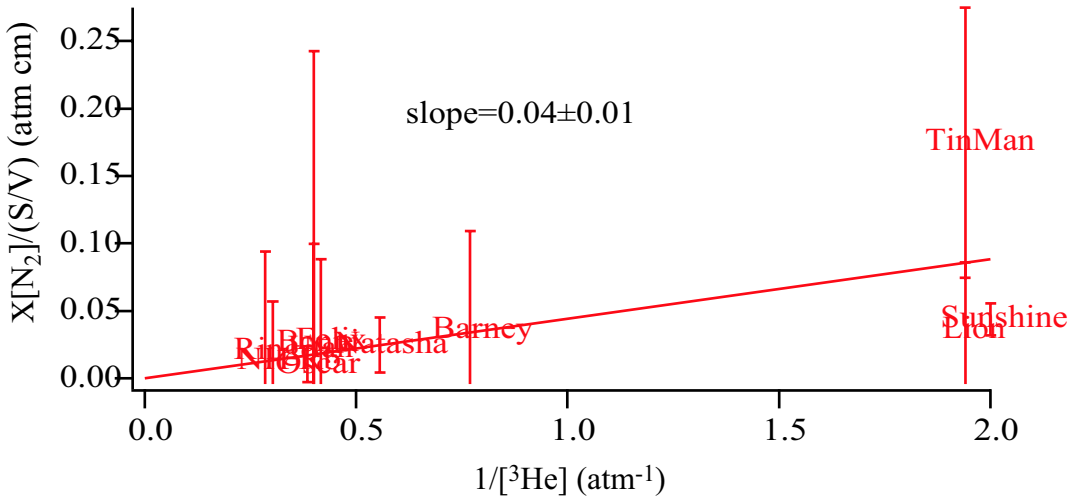

Fig. 8.5: Measured X-factors for a large number of Rb-SEOP cells as a function of 1/ [^{3}He] X[N_2] is plotted vs. 1/ [^{3}He] showing a very slight [^{3}He] dependance.

an average value of 0.05 ± 0.01.

Now we look at the data for flat windowed cells. Due to the constraints of Flat windowed cells, all of them had similar ^{3}He pressures, and we only had cells with either 50 torr N_2 or 6 torr N_2 thus making any conclusions about the coefficients of the [^{3}He] or [N_2] dependance impossible to obtain to any certainty. Further all of these cells except for the two Amersham cells and BamBam were nearly identical. Thus we only show data for the X-factor for flat windowed cells as a function of S/V. We do note that the two Amersham cells, for which all parameters other than S/V were constant, showed a nearly exact S/V dependance.

8.4 Conclusions

We have studied the X-factor in Rb SEOP cells at great length and we feel further systematic studies are warranted in order optimize the achievable P_{He}. In all cases the data shows a linear surface to volume ratio dependance on the observed X-factor,

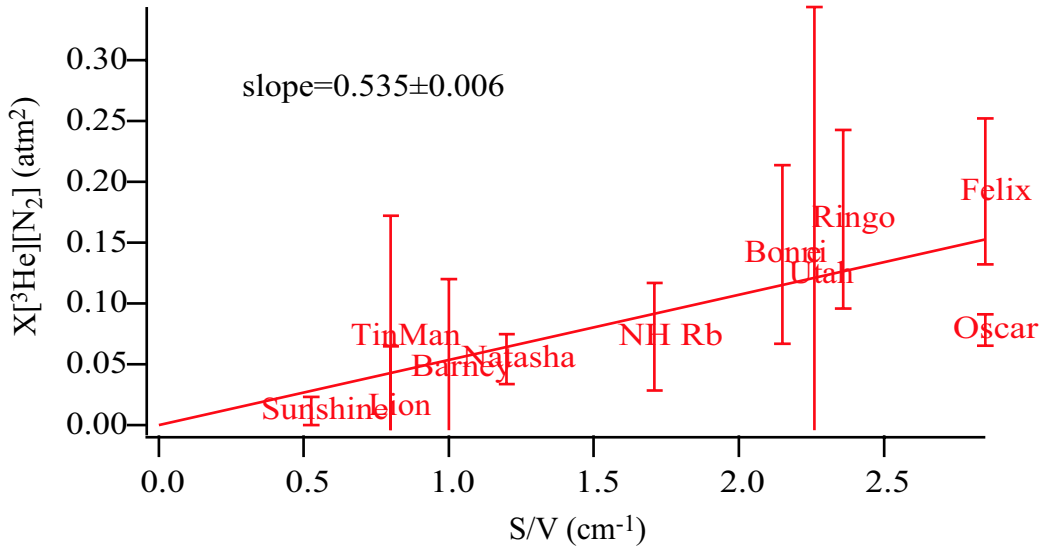

Fig. 8.6: Measured X-factors for a large number of Rb-SEOP cells as a function of S/V. X[^{3}He] [N_2] vs. S/V

thus implying X is dominantly a surface interaction effect, suggesting it is desirable to move to larger cells. Larger cells are normally desirable for neutron spin filter applications due to the large diameter ($\sim$ 5") of typical neutron beams, and large volume is typically desirable for high polarization production rates which would be of great use for medical applications. Previously it was difficult to fully polarize the alkali in large diameter cells due the the pump light intensity required, but our FNDAB has helped remove much of this concern. Further, our data suggests going to higher buffer gas pressures will provide additional gains, by allowing X to be minimized. Careful study of the [N_2] and [^{3}He] dependance should allow X to be minimized, and the polarization to be maximized. Experimentally, given the constraints of the mechanical properties of the cells to withstand higher pressures, and dependance of the Γ_{He} on ^{3}He pressure [Newbury93], and N_2 pressure, maximizing P_{He} will involve a balance

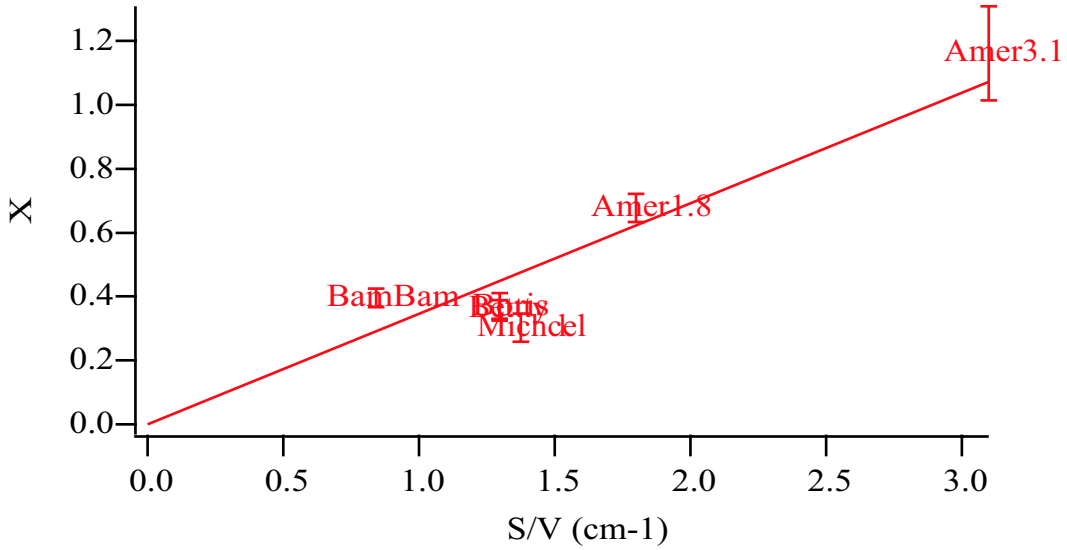

Fig. 8.7: Measured X-factors for our flat windowed cells as a function of S/V.

between lowering X, and increasing Γ_{He}. Given the data presented here, we should be able to experimentally achieve $P_{\mathrm{He}} \sim 90\%$. In the course of these studies, without this optimization, we have already obtained the highest ^{3}He polarizations, $\sim 80\%$, ever reported in a high pressure cell (1 atmosphere or higher). This record is inclusive of using either SEOP, or the competing MEOP (metastability exchange optical pumping) method.

9. CONCLUSIONS

In this dissertation I have described a series of measurements and discoveries with respect to long standing mysteries in the SEOP processes. Here I summarize the advances we have made as well as the remaining topics yet to be explored as a direct consequence of this work.

9.1 Summary

For the first time anywhere we have developed and implemented a complete set of diagnostics, capable of measuring all fundamental parameters involved in SEOP. Our FNDAB has allowed us to explore areas of SEOP previously unexplored. The FNDAB and our diagnostics have already allowed us to optimize the practical spin exchange optical pumping of ^{3}He enabling us to produce the highest ^{3}He polarizations, highest efficiency, and fastest spin exchange rates ever obtained. We have determined the ^{3}He spin exchange rate coefficients for Rb and K, and measured their fundamental efficiencies. Further we have shown that non-ideal spatial and frequency modes of the optical pumping source can greatly limit the expected overall efficiency of optical pumping. Improper light collimation causes rapid attenuation of on resonant pumping light, and D_2 pumping caused by ^{3}He -alkali-metal molecular potentials places much more stringent demands on the spectral profile of the pumping laser than previously thought. Lastly our extensive studies of the additional ^{3}He relaxation, the X-Factor, are finally beginning to show clues that will hopefully allow the X-factor to minimized

if not eliminated.

9.2 Implications

Our proof-of-principle work with HySEOP, has opened up many new possibilities for the exploration of optical pumping with the alkali-metal species other than Rb. Further the spin exchange rate coefficient measurements we presented, first photon efficiency measurements, and determination of the EPR frequency shift enhancement factors will help lay the groundwork for future investigations. HySEOP should prove to be an extremely valuable analytical and practical tool for future fundamental studies of SEOP in other alkali-metals. The methods and results already presented with HySEOP have created great interest in its use for the practical application of high efficiency, rapid production of ^{3}He samples. Much work is left to fully optimize HySEOP for use in ^{3}He production.

9.3 Future Work

Immediate investigations should continue to explore the development of HySEOP for Na-Rb mixtures. Another direct, perhaps technologically less demanding direct extension of HySEOP would be to explore Cs-Rb-^{129}Xe, which could possibly demonstrate gains similar to those obtained with K-Rb-^{3}He [Walker97]. Further systemic studies of the X-factor dependance on gas pressure need to be made, because they could prove to be a critical point to help understand ^{3}He- cell wall inteactions.

APPENDIX

A. ABSORPTION IN OPTICAL PUMPING

A.1 Excess absorption in optical pumping

Excess absorbtion greatly limits the photon efficiency in optical pumping. We will assume that all hyperfine levels, i.e the D1 and D2 of each alkali can potentially be polarized by a given circularly polarized laser. This absorbtion can lead to optical pumping and polarization in the desired direction or $P_{1/2}$ pumping, optical pumping in the opposite direction forming an effective ralaxation or $P_{3/2}$ pumping, and general absorbtion without dichroism.

A.1.1 General Optical Pumping and Absorbtion

For typical $P_{1/2}$ or D1 optical pumping and absorbtion, the observed build up of polarization, $d(sP)/dt$ where s is the slowing down factor is given by,

$$\frac{d(sP)}{dt} = R(1-P) \tag{A.1}$$

$$A = R(1-P) \tag{A.2}$$

here P is the alkali polarization, R is the (D1 by D1 light) pumping rate and A is absorbtion.

For $P_{3/2}$ or D2 optical pumping and absorbion:

$$\frac{d(sP)}{dt} = R'(-1/2-P) \tag{A.3}$$

$$A = R'(1+P/2) \tag{A.4}$$

where R' is the D2 pumping rate produced by the wings of the D1 light or by fine structure mixing in the alkali.

Finally for general pumping and absorbtion without any dichroism in other words simple absorbtion by far off resonant light incapeable of producing polarization,

$$\frac{d(sP)}{dt} = -R''P \tag{A.5}$$

$$A = R'' \tag{A.6}$$

If we assume that all types of pumping are possible for a given alkali or mixture of alkalis the sum of the three types of pumping we qet an effective pumping rate,

$$R_{\text{eff}} = R + R' + R'' \tag{A.7}$$

and the maximum achievable alkali polarization for infinite pumping power, P_∞,

$$P_\infty = \frac{(R - R'/2)}{R_{\text{eff}}} \tag{A.8}$$

as a result the new build up of polarization and corresponding absorbtion becomes,

$$\frac{d(sP)}{dt} = R_{\text{eff}}(P_\infty - P) \tag{A.9}$$

$$A = R_{\text{eff}}(1 - P_\infty P) \tag{A.10}$$

So the general case of optical pumping with cirularly polarizied light can be parameterized in terms of numbers R_{eff} and P_∞.

Adding alkil relaxation to this relation we get the expected relation,

$$P = P_\infty \frac{R_{\text{eff}}}{R_{\text{eff}} + \Gamma} \tag{A.11}$$

but the absobtion rate is,

$$A = R_{\text{eff}}(1 - PP_\infty) = \frac{R_{\text{eff}}\Gamma}{R_{\text{eff}} + \Gamma}\left(1 + \frac{R_{\text{eff}}}{\Gamma}(1 - P_\infty^2)\right) \tag{A.12}$$

which shows that there is an excess absorption of roughly

$$1 + \Upsilon = 1 + \frac{R_{\text{eff}}}{\Gamma}(1 - P_\infty^2) \tag{A.13}$$

For a rough estimate based on broadband pumping results under typical conditions, if we take $P_\infty = 0.9$, $\Gamma = 350/\text{s}$, $R_{\text{eff}} = 24000/\text{s}$. Then $\Upsilon = 13$!

Not only does this effect cause one to observe additional absorption under pumping condition, but it can be observed in the optical pumping transients. The initial slope of the optical pumping transient is $\mathcal{S} = R_{\text{eff}} P_\infty / s$, where s is the slowing down factor. The polarization as a function of pumping rate should be

$$\frac{1}{P} = \frac{1}{P_\infty} + \frac{\Gamma}{\mathcal{S}} \tag{A.14}$$

as a result a graph of $1/P$ vs $1/S$ should have a slope of Γ and an intercept of $1/P_\infty$. The results of these mesurments agree with direct measurments of the alkali polarization under conditions of intence optical pumping.

A.1.2 Extension to Hybrid Pumping

Now we will extend this discussion to include the terms arrising from a second alkali whose resonances are far away from those of the optically pumped species resonance. If we assume that the potassium has no dichroism at 795 nm, then the rate equation for hybrid pumping with K:Rb density ratio $\mathcal{D}$ is

$$\frac{dsP}{dt} = R_{\text{eff}}(P_\infty - P) - \Gamma_{\text{Rb}} P + \mathcal{D}(-\Gamma_{\text{K}} - R''_{\text{K}})P \tag{A.15}$$

Here R_{eff} and P_∞ are still the rubidium effective pumping rate and maximum polarization. The relaxation rates for Rb and K are conveniently lumped into the effective rate $\Gamma_{\text{RbK}} = \Gamma_{\text{Rb}} + r\Gamma_{\text{K}}$. The initial slope is still $\mathcal{S} = R_{\text{eff}} P_\infty / s$ keeping in mind that s

has changed to $s_{eff} = s_{Rb} + \mathcal{D}s_K$ due to the presence of the potassium, the equilibrium polarization is therefore

$$P = P_\infty \left(\frac{R_{\text{eff}}}{R_{\text{eff}} + \Gamma_{\text{RbK}} + R''_{\text{K}}} \right) \tag{A.16}$$

so that

$$\frac{1}{P} = \frac{1}{P_\infty} \left(1 + \frac{R''_{\text{K}}}{R_{\text{eff}}} \right) + \frac{\Gamma_{\text{RbK}}}{\mathcal{S}} \tag{A.17}$$

allows one to back out the extra effect of the potassium pumping.

A.1.3 Light Propagation

Because of the excess absorption, it is obvious that the light will be more rapidly attenuated as it travels through the cell. Assuming narrow-band pumping, the pumping rate obeys

$$\frac{dR_{\text{eff}}}{dz} = -[Rb]\sigma \frac{R_{\text{eff}}\Gamma}{R_{\text{eff}} + \Gamma} \left(1 + \frac{R_{\text{eff}}}{\Gamma}(1 - P_\infty^2) \right) \tag{A.18}$$

In the limit $R_{\text{eff}} \gg \Gamma$, and letting $q = 1 - P_\infty^2$,

$$\frac{dR_{\text{eff}}}{dz} = -[Rb]\sigma\Gamma \left(1 + q\frac{R_{\text{eff}}}{\Gamma} \right) \tag{A.19}$$

so that the attenuation behaves as if the spin-relaxation rate has been increased by the factor $1 + \Upsilon$. The solution to this equation is

$$R_{\text{eff}}(z) = R_{\text{eff}}(0)e^{-qz/l} - \Gamma \left(\frac{1 - e^{-qz/l}}{q} \right) \tag{A.20}$$

where the characteristic absorption length $l = 1/([Rb]\sigma)$. A plot is shown below, for $R_{\text{eff}}(0)/\Gamma = 68$, $q = 0.1$ (corresponding to 95% P_∞).

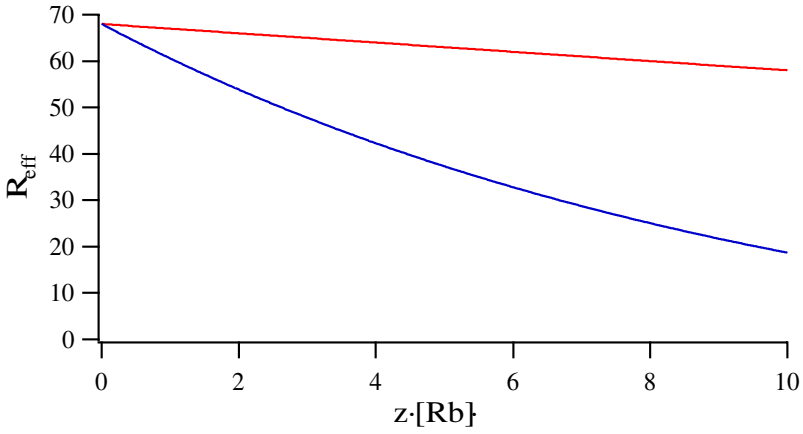

Fig. A.1: Comparison of light attentuation with and without the excess absorption effect.

B. SPIN EXCHANGE, SPIN TEMPERATURE AND THE NUCLEAR SLOWING DOWN FACTOR

This appendix summarizes important properties of spin exchange for both pure alkali-metals and HySEOP mixtures. These explanations and derivations are largely found in references [Happer72, Anderson60]. The work with HySEOP relies heavily on the concepts described here.

B.1 Electron-Electron Spin Exchange

The spin exchange between any two alkali-metal atoms, regardless, can be written as,

$$A(\uparrow) + B(\downarrow) \rightarrow A(\downarrow) + B(\uparrow), \tag{B.1}$$

where the arrows indicate the orientation of the valence spin. This interaction can be though of as the precession of the individual electron spins around the singlet coupled state. We expect spin exchange whenever,

$$\int \frac{dt}{\hbar} V_S(r(t)) \gg 1 \tag{B.2}$$

where the integral is over the collision trajectory and V_S is the singlet potential.

Using this relation we can obtain electron-electron spin exchange cross sections very similar to the experimentally observed value of ~ 200Åfor K, Rb and Cs [Happer72]. Additionally because this precession is much faster than any laboratory magnetic field, we do not expect this to be decoupled.

Given these cross sections for an alkali-metal vapor with 10^{15} atoms cm^{-3}, the electron-electron spin exchange rate will exceed 10^5s^{-1}. Since this process is faster than any relaxation mechanism in our SEOP cells.

Electron spin-exchange causes atomic coherences, such as hyperfine precession, to decay. A full mathematical treatment which includes the effects of spin exchange collisions on the atomic density matrix can be found in [Appelt98, Happer72].

B.2 Hyperfine Interaction

The hyperfine interaction is another method that distributes spin among the alkali-metal in SEOP, this time between the alkali-metal valence electron and its nucleus. This process is also very rapid. However noting that the alkali hyperfine interaction can be decoupled by a ∼kG magnetic field, Walker and Anderson have shown tht the rate od polarization exchange between electrons and nuclei is slowed down approximately as $1(1+x^2)$ where $x = g_S\mu_B B/\Delta E_{fhs}$ is the Breit-Rabi parameter [Ramsey53].

B.3 Spin Temperature

If the previous two processes proceed at a rate much higher than any spin relaxation or optical pumping rate, the system remains in equilibrium with respect to spin exchange even when it is taken out of its global equilibrium with respect to spin relaxation. This the system is said to be in spin temperature [Anderson60]. However we quickly note here that this breaks down for initial optical pumping transients in our experiment because the initial optical pumping rate can be calculated to be over $\sim 10^6$ for some instances in our work. Once the light alkali-metal has been allowed to reach steady state with respect to the light field, or when the pumping rate has be deliberately lowered, these properties will hold.

The characterization of the alkali-metal electron and nuclear spin in terms of spin temperature simplifies analysis considerably because the populations of all of electron and nuclear Zeeman levels can be written in terms of one parameter, the inverse spin temperature β. The following derivation is a special case of the more general work in [Anderson60].

In spin temperature, the electron and nuclear Zeeman poplations are in equilibrium with respect to an exchange process therefore,

$$(m_S + 1, m_I) \leftrightarrow (m_S, m_I + 1). \tag{B.3}$$

In equilibrium the forward and backward processes must proceed at the same rate, therefore the probabilities of being in the m_S, m_I states are related by,

$$P(m_S + 1)P(m_i) = P(m_S)P(m_I + 1) \tag{B.4}$$

for each $m_I = -1...I - 1$. These $2I$ equations along with $\sum P(m_S) = \sum P(m_I) = 1$, allow us to eliminate all but one of the probabilities. It is convenient to parameterize all the probabilities in terms of the inverse spin temperature parameter such that,

$$e^{-\beta} = \frac{P(m_{1/2})}{P(m_(- 1/2))}. \tag{B.5}$$

β is analogous to $\beta = 1/kT$ because $\beta = 0$ is a maximally disordered, or unpolarized, state and $\beta = \pm\infty$ corresponds to the most ordered, or polarized, states. In terms of β, the solutions to equation B.4 are;

$$\begin{aligned} P(m_S) &= e^{\beta m_S} \frac{2}{\cosh(\beta/2)}, \\ P(m_I) &= e^{\beta m_I} \frac{\sinh(\beta/2)}{\sinh(\beta(I + 1/2))}. \end{aligned} \tag{B.6}$$

Here we note that the probability of being in a spin state with z projection m_F is proportional to $e^{\beta m_F}$ which is a general feature of a system in spin temperature equilibrium.

B.4 Nuclear Slowing Down Factors

The exchange of spin between the valance electron and nucleus causes the measured valence electron relaxation rate to be lower than the true relation by a factor of the nuclear slowing down factor. From equation B.6 we can calculate the expectation values of the electron and nuclear spin respectively to be,

$$\begin{aligned} \langle S_z \rangle &= \sum P(m_S) m_s = (1/2)\tanh(\beta/2), \\ \langle I_z \rangle &= \sum P(m_I) m_I = ((2I+1)/2)\mathrm{ctch}((2I+1)\beta/2) - (1/2)\mathrm{ctnh}(\beta/2). \end{aligned} \quad \text{(B.7)}$$

In general, the fraction of polarization in the electron spin will be a nonlinear function in β making analysis of the relaxation difficult. When measuring and electron spin relaxation process, the measured relaxation will be slower than the true relaxation rate by a factor of $1 + \langle I_z \rangle / \langle S_z \rangle$, and for a nuclear relaxation process by a factor of $1 + \langle S_z \rangle / \langle I_z \rangle$ due to the polarization transfer between the the electron and the nucleus.

For the instances used in this work we minimize this problem by only taking relaxation measurements in the limit where the polarization is low. In this limit, the factor of $\langle I_z \rangle / \langle S_z \rangle$ becomes,

$$\langle I_z \rangle / \langle S_z \rangle \rightarrow \epsilon \quad \text{(B.8)}$$

where,

$$\epsilon = \frac{4}{3} I(I+1). \quad \text{(B.9)}$$

Thus in this limit the measured and true relaxation rates are related by a constant slowing down factor. This factor, $s = 1/(1+\epsilon)$ for processes acting on the electron and $\epsilon/(1+\epsilon)$ for processes acting on the nucleus , is commonly referred to as the "slowing down factor." Using this approximation has been determined to lead to negligible error as long as the polarization is kept $< 5\%$. The appropriate nuclear slowing down factor

Tab. B.1: Slowing down factor for electron relaxation. The observed relaxation rate times $1+\epsilon$ is the true relaxation rate.

Alkali-metal	$1+\epsilon$
Na	6
K	6
^{85}Rb	38/3
^{87}Rb	6
Rb (nat.)	10.8
Cs	22

for electron relaxation are given in ref. [Happer72]. The slowing down factors for nuclear relaxation are listed in table B.1.

In a HySEOP cell we must solve for the combined slowing down factor due to the multiple isotopes. In a HySEOP cell, with alkali-metals, A and B, the observed alkali-metal relaxation will be the sum of the relaxation of the individual alkali metal species weighted by the ratio of their densities, $\mathcal{D} = [B]/[A]$. Now the combined HySEOP slowing down factor becomes,

$$s = s_A + \mathcal{D} s_B \tag{B.10}$$

where s_A and s_B are the individual slowing down factors for alkali A and B respectively.

C. PHYSICAL AND OPTICAL PROPERTIES OF THE ALKALI-METALS

C.1 Vapor Pressure

Tab. C.1: The coefficients for determining the vapor pressures of the alkali-metals [CRC].

	A	B
Cs	4.165	3830
Rb	4.312	4040
K	4.402	4453
Na	4.704	5377
Li	5.055	8310

In order to produce HySEOP cells with desirable vapor pressure ratios of the secondary alkali to that of Rb. For a quantitative estimate, we assume that the vapor densities approximately obey Raoult's law [CRC], $[\mathrm{Rb}] \approx f_{\mathrm{Rb}}[\mathrm{Rb}]_0$, where f_{Rb} is the mole fraction of Rb in the metal and $[\mathrm{Rb}]_0$ is the saturated vapor density for pure Rb metal. Quantitative estimates of the pressures of the alkali metals are given by $\log_1 0(P) = A - BT^{-1}$ where P in in atmospheres and T is in $^\circ K$. Table C.1 lists the A and B coefficients for all of the alkali-metals. Plots of the resulting alkali-metal number densities, are shown in figure C.1. We note that the number densities for studies of SEOP can not be derived from temperature sensor readings of SEOP cells using these curves.

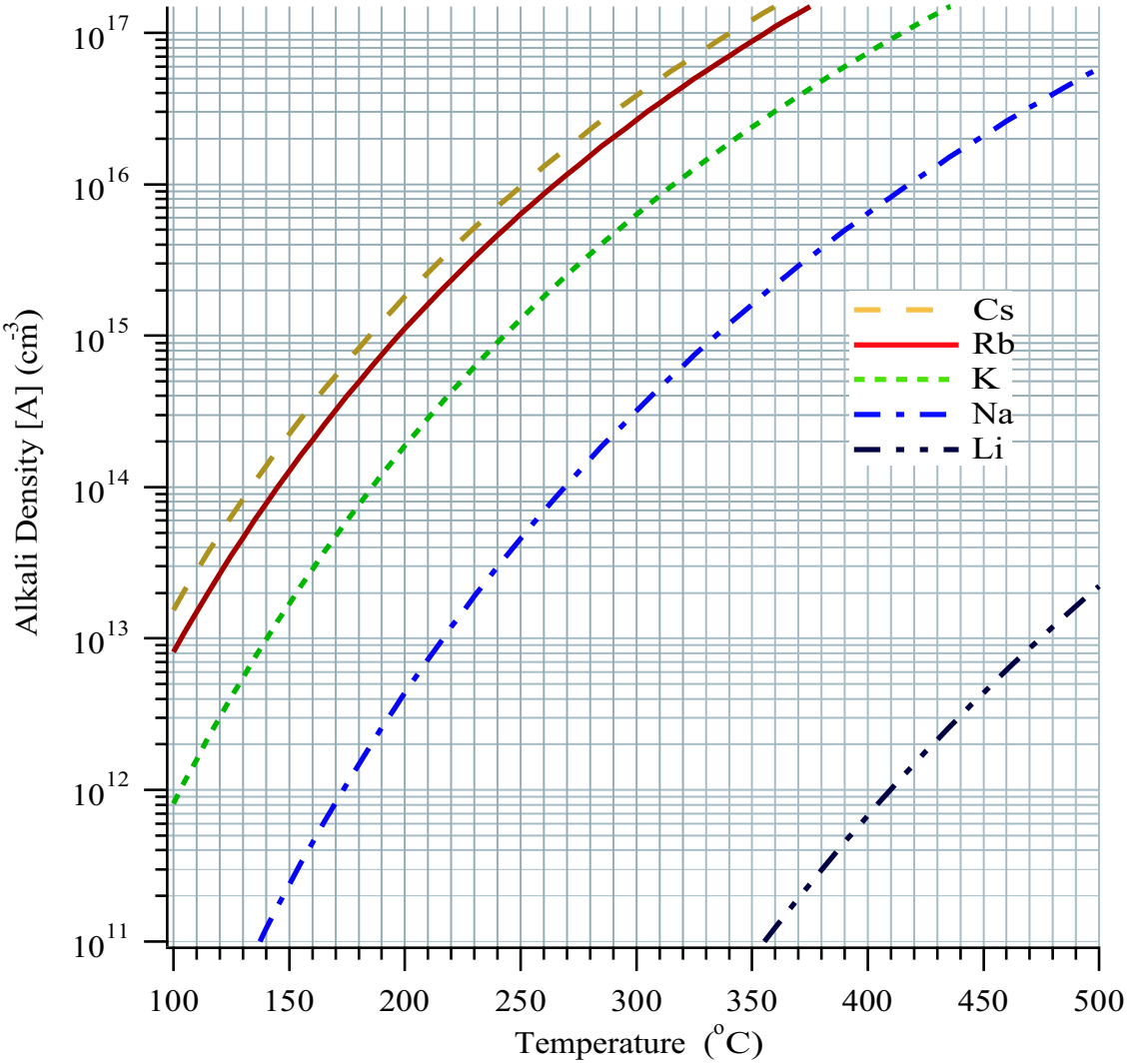

Fig. C.1: Vapor pressure for the alkali-metals Cs, Rb, K, Na and Li. Numeber densities are given by $[A] = 7.336 \times 10^{21} T^{-1} (10^{A+BT^{-1}})$ where T in in Kevin and [A] will be cm^{-3} where the A and B coefficients are listed in table C.1

Tab. C.2: Basic Atomic Parameters of the Alkali-Metals. The 1 and 2 subscripts denote the D_1 and D_2 lines respectively. More extensive properties are listed in ref. [Happer72]

	Natural abundance (%)	I	$\Delta\nu_{hfs}$ (MHz)	λ_1 (Å)	λ_2 (Å)	f_1	f_2	μ_I (μ_N)
^{6}Li	7.5	1	228.2	6708	6708	0.25	0.50	0.8220
^{7}Li	92.5	3/2	803.5					3.2564
^{23}Na	100	3/2	1771.6	5896	5890	0.33	0.65	2.2176
^{39}K	93.2	3/2	461.7	7699	7665	0.34	0.68	0.3914
^{41}K	6.8	3/2	254					0.2148
^{85}Rb	72.2	5/2	3035.7	7948	7800	0.35	0.70	1.3527
^{87}Rb	27.8	3/2						2.7506
^{133}Cs	100	7/2	9192.6	8944	8521	0.33	0.66	2.579

C.2 Basic Parameters of the Alkali-Metal Atoms

Here we list many of the basic optical pumping and spin exchange parameters of the alkali-metals. Table C.2 list many of the important parameters for the alkali D_1 and D_2 transitions. Reference [Happer72] gives a more complete listing including Einstein A and B coefficients and the excited state lifetimes.

BIBLIOGRAPHY

[Abragam61] A. Abragam. **The principles of nuclear magnetism**, Oxford: Clarendon Press. (1961).

[Albert94] M.S. Albert, G.D. Cates, B. Driehuys, W. Happer, B. Saam, C.S. Springer, and A. Wishnia. Biological magnetic resonance imaging using laser-polarized ^{129}Xe, **Nature, 370**, 199-201, (1994).

[Allred02] J.C. Allred, R.N. Lyman, T.W. Kornack and M.V. Romalis. High-sensitivity atomic magnetometer unafected by spin-exchange relaxation. **Phys. Rev. Lett., 89**, 130801(4), (2002).

[Anderson59] L. W. Anderson, F. M. Pipkin and J. C. Baird. N14-N15 Hyperfine Anomaly. **Phys. Rev., 116**, 87, (1959).

[Anderson60] L.W. Anderson, F.M. Pipkin and J.C. Baird. Hyperfine Structure of Hydrogen, Deuterium and Tritium. **Phys. Rev., 120**, 1279, (1960).

[Appelt99] S. Appelt, A. Ben-Amar Baranga, A. R. Young and W. Happer. Light narrowing of rubidium magnetic resonance lines in high-pressure optical pumping cells. **Phys. Rev. A, 59**, 2078, (1999).

[Appelt98] S. Appelt, A. Ben-Amar Baranga, C.J. Erickson, M.V. Romalis, A.R. Young and W. Happer. Theory of spin-exchange optical pumping of ^{3}He and ^{129}Xe. **Phys. Rev. A, 58**, 1412-39, (1998).

[Babcock03] E. Babcock, I.A. Nelson, S. Kadlececk, Bastiaan Driehuys, L.W. Anderson, F.W. Hersman, T.G. Walker. Hybrid spin-exchange optical pumping of ^{3}He. **Phys. Rev. Lett., 91**, 123003(4), (2003).

[Babcock05] E.Babcock, I.A. Nelson, S. Kadlecek, T.G. Walker. ^{3}He polarization dependant EPR frequency shifts of alkali-^{3}He pairs. **Phys. Rev. A, 71**, 013414(5), (2005).

[Babcock05b] E.Babcock, B. Chann, I.A. Nelson and T.G. Walker. Frequency narroewed diode array bar. **Applied Optics**, (Accepted), (2005).

[Baranga98] A. Ben-Amar Baranga, S. Appelt, C. Erickson, A. Young, and W. Happer. Polarization of ^{3}He by spin exchange with optically pumped Rb and K vapors. **Phys. Rev, A., 58**, 2281-4, (1998).

[Barton94] A.S. Barton, N.R. Newbury, G.D. Cates, B. Driehuys, H. Middleton and B. Saam. Self-calibrating measurement of polarization-dependent frequency shifts from Rb-^{3}He collisions. **Phys. Rev. A, 49**, 2766 (1994).

[Baskar79] N.D. Bhaskar, M. Hou, B. Suleman, and W. Happer. Propagating, Optical-pumping wave fronts. **Phys. Rev. Lett. 43**, 519, (1979).

[Bayram] S.B. Bayram and T.E. Chupp. Operation of a single mode external-cavity laser diode array near 780 nm. **Rev. Sci. Instrum., 73**, 4169-71, (2002).

[Bear00] D. Bear, R.E. Stoner, R.L. Walsworth, V.A. Kostelecky and C.D. Lane. Limit on Lorentz and CPT violation of the neutron using a two-species noble-gas maser.**Phys. Rev. Lett. 85**, 5038-41, (2000).

[Borel02] P.I. Borel, C.J. Erickson, and D.K. Walter, Magnetic decoupling of Rb spin relaxation in H_2 buffer gas. **Phys. Rev. A, 66**, 063410 (2002).

[Borel03] P.I. Borel, L.V. Sogaard, W.E. Svendsen and N. Andersen. Spin-exchange and spin-destruction rates for the ^{3}He- Na system. **Phys. Rev. A., 67**, 62705, (2003).

[Bouchiat60] M.A. Bouchiat, T.R. Carver, and C.M. Varnum, Nuclear polarization in ^{3}He gas induced by optical pumping and dipolar exchange. **Phys. Rev. Lett., 5**, 373 (1960).

[Cates88] G.D. Cates, S.R. Schaefer and W. Happer. Relaxation of spins due to field inhomogeneities in gaseous samples at low magnetic fields and low pressures. **Phys. Rev. A, 37**, 2877 (1988).

[Chann00] B.Chann, I.Nelson, and T.G. Walker. Frequency-narrowed external-cavity diode-laser-array bar. **Opt. Lett., 25**, 1352-54, (2000).

[Chann02a] B.Chann, E.Babcock, L.W.Anderson and T.G.Walker. Skew light propagation in optically thick optical pumping cells. **Phys. Rev. A, 66**, 033406(3), (2002).

[Chann02b] B. Chann, E. Babcock, L.W. Anderson and T.G. Walker. Measurements of ^{3}He spin-exchange rates. **Phys. Rev. A, 66**, 033406(9), (2002).

[Chann03] B. Chann, E. Babcock, L.W. Anderson, T.G. Walker, W.C. Chenn, T.B. Smith, A.K. Thompson and T.R. Gentile. Production of highly polarized ^{3}He uning spectrally narrowed diode lase array bars. **J. of Applied Phys., 94**, 6908-14, (2003).

[Chann03b] B. Chann. Ph.D. thesis. University of Wisconsin, Madison. (2003).

[Chen03] W. C. Chen, C. Bailey, J.A. Borchers, R.F.C. Farrow, T.R. Gentile, D. Hussey, C.F. Majkrzak, K.V. O'Donovan, N. Remmes, W.M. Snow and A.K. Thompson. Polarized ^{3}He analyzers for neutron reflectometry. **Physica B., 335**, 196-200, (2003).

[Chupp00] J.N. Zerger, M.J. Lim, K.P. Coulter and T.E. Chupp. Polarization of ^{129}Xe with high power external-cavity laser diode arrays. **Applied Phys. Lett., 76**, 1798-1800, (2000).

[Coulter88] K.P. Coulter, A.B. McDonald, W. Happer, T.E. Chupp and M.E. Wagshul. Neutron polarization with polarized ^{3}He . **Nucl. Instrum. Methods Phys. Res. A, 270**, 90(4), (1988).

[CRC] D. Lide. Handbook of Chemistry and Physics 85^{th} ed. (2004)

[Driehuys96] B. Driehuys, G.D. Cates, E. Miron, K, Sauer, D.K. Walter and W. Happer. High-volume production of laser-polarized ^{1}29Xe. **Applied Phys. Lett., 69**, 1668-70, (1996).

[Franzen59] W. Franzen. Spin Relaxation of Optically Aligned Rubidium Vapor. **Phys. Rev., 115**, 850 (1959).

[Gallagher95] J.A. Neuman, P. Wang and A. Gallagher. Robust high-temperature sapphire cell for metal vapors. **Rev. Sci. Instrum., 66**, 3021-3, (1995).

[Happer72] W. Happer. Optical pumping. **Rev. Mod. Phys., 44**, 169-249, (1972).

[Happer77] W. Happer, A.C. Tam. Effect of rapid spin exchange on the magnetic-resonance spectrum of alkali vapors. **Phys. Rev. A, 16**, 1877-91, (1977)

[Happer87] W. Happer amd W.A. Van Wijmgaarden. An optical puming primer. **Hyperfine Interactions, 38**, 435-470, (1987)

[Happer01] W. Happer, G.D. Cates, M.V. Romalis and C.J. Erikson. US Patent No. 6,318,092. (2001).

[Heil99] W. Heil, J. Dreyer, D. Hofmann, H. Humblot, E. Lelievre-Berna and F. Tasset. ^{3}He neutron spin-filter. **Physica B, 267-268**, 328 (1999).

[Hrycyshyn70] E.S. Hrycyshyn and L. Krause. Inelastic collisions between excited alkali atoms and molecules. VII. Sensitized fluorescence and quenching in mixtures of rubidium with $H_2 2, HD, D_2, N_2, CH_4, CD_4, C_2H_4$, and C_2H_6, **Can. J. Phys. 48**, 2761 (1970).

[Ino04] T. Ino, S. Muto, Y. Masuda, G. Kimb and V.R. Skoyc. Development of ^{3}He polarized neutron spin filters at KEK. **Physica B, 58** (2004).

[Jackson] J.D. Jackson. **Classical Electrodynamics**. New York: Wiley, (1999), p 196.

[Jacob04] R.E. Jacob, J. Teter, B. Saam, W. C. Chen and T. R. Gentile. Low-field orientation dependence of 3He relaxation in spin-exchange cells. **Phys. Rev. A, 69**, 021401(4), (2004).

[Jau02] Y.-Y Jau, N.N. Kuzma, and W. Happer. High-field measurement of the 129Xe-Rb spin-exchange rate due to binary collisions. **Phys. Rev. A, 66**, 052710, (2002)

[Jau04] Y.-Y Jau, A.B. Post, N.N. Kuzma, A.M. Braun, M.V. Romalis and W. Happer. Intense narrow atomic-clock resonances. **Phys. Rev. Lett, 92** 110801(4) (2004).

[Jones00] G. Jones, T. Gentile, A. Thompson, Z. Chowdhuri, M. Dewey, W. Snow and F. Wietfeldt. Test of ^{3}He-based neutron polarizers at NIST.**Nucl. Instrum. & Methods A, 440**, 772-6, (2000).

[Jones04] G.L. Jones, J. Baker, W.C. Chen, B. Collett, J.A. Cowan, M.F. Dias, T.R. Gentile, C. Hoffmann, T. Koetzle, W.T. Lee, M. Miller, A. Schultz, W.M. Snow, X. Tong, H. Yan, A. Yue. Continuously operating compact 3He-based neutron spin filter. **submitted to Physica B**, (2004)

[Kadlecek00] S. Kadlecek. Ph.D. thesis. University of Wisconsin, Madison. (2000).

[Larson91] B. Larson, O. Hausser, P.P.J. Delheij, D.M. Whittal and D. Thiessen. Optical pumping of Rb in the presence of high pressure ^{3}He buffer gas. **Phys. Rev. A, 44**, 3108-18, (1991).

[Lister04] G.G. Lister, J.E. Lawler, W.P. Lapatovich and V.A. Godyak. The physics of discarge lamps. **Rev Mod. Phys., 76**, 541-598, (2004).

[Migdalek98] J. Migdalek and Y.K. Kim. Core polarization and oscillator strength ratio anomaly in potassium, rubidium and caesium. **J. Phys. B: At. Mol. Opt. Phys. 31**, 1947 (1998).

[Moller02] H.E. Moller, X.J. Chen, B. Saam, K.D. Hagspiel, G.A. Johnson, T.A. Altes, E.E. de Lange and H.-U. Kauczor. MRI of the Lungs Using Hyperpolarized Noble Gases, **Magnetic Resonance in Medicine, 47**, 102951 (2002)

[NGDC] National Geographic Data Center. Estimated values of magnetic field properties.

www.ngdc.noaa.gov/seg/geomag/jsp/struts/calcPointIGRF. (2005)

[Nelson00] I.A. Nelson, B. Chann and T.G. Walker. Spin-exchange optical pumping using a frequency-narrowed high power diode laser. **Applied Phys. Lett., 76**, 1356-58, (2000).

[Newbury93] N.R. Newbury,A.S. Barton, G.D. Cates, W. Happer and H. Middle- ton. Gaseous ^{3}He-^{3}He magnetic dipolar spin relaxation. **Phys. Rev. A, 48**, 4411-20, (1993).

[Omega] **The Temperature Handbook**. Omega Engineering Inc. z56-z89, (2000).

[Ramsey53] N.F. Ramsey. **Nuclear moments**. New York: Wiley&Sons Inc. (1953).

[Rich02] D.R. Rich, T.R. Gentile, T.B. Smith, A.K. Thompson and G.L. Jones. Spin exchange optical pumping at pressures near 1 bar for neutron spin filters. **Applied Phys. Lett., 80**, 2210-3 (2002).

[Romalis97] M.V. Romalis, E. Miron and G.D. Cates. Pressure broadening of Rb D_1 and D_2 lines by ^{3}He, ^{4}He, N_2, and Xe: line cores and near wings. **Phys. Rev. A, 56**, 4569-78, (1997).

[Romalis98] M.V. Romalis and G.D. Cates. Accurate ^{3}He polarimetry using the Rb Zeeman frequency shift due to the Rb-3He spin-exchange collisions. **Phys. Rev. A, 58**, 3004-11, (1998).

[Romalis00] M.V. Romalis. Narrowing of high power diode laser arrays using reflection feedback from an etalon. **Applied Phys. Lett., 77,** 1080-81, (2000).

[Scheafer89] S.R. Schaefer, G.D. Cates, Ting-Ray Chien, D. Gonatas, W. Happer and T.G. Walker. Frequency shifts of the magnetic-resonance spectrum of mixtures of nuclear spin-polarized noble gases and vapors of spin-polarized alkali-metal atoms. **Phys. Rev. A., 39**, 5613, (1989).

[Skomski] R. Skomski and J.M.D. Coey. **Permanent Magnetism**. Bristol: Institute of Physics Publishing, (1999), p. 55.

[SMCHandbook] Special Metals Corp Handbook. www.specialmetals.com (2003)

[Souza] M. Souza, Glass Blower, Princeton University. personal comunication. (2004)

[Stoner02] R.E. Stoner and R.L. Walsworth. Measurement of the ^{21}Ne Zeeman frequency shift due to Rb-^{21}Ne collisions. **Phys. Rev. A., bf 66**, 32704, (2002).

[Pascale76] J. Pascale and J. Vanderlanque. Excited molecular terms of the alkalimrare gas atom pairs. **J. of Chem. Phys., 60**, 2278-89, (1976).

[Pomeroy] V. Pomeroy. Ph. D. thesis. University of New Hampshire, (1998), unpublished.

[Vliegen01] E. Vliegen, S. Kadlecek, L. W. Anderson and T. G. Walker. Faraday rotation density measurements of optically thick alkali metal vapors. **Nucl. Inst. Meth. Phys. Res. A, 460**, 444-50 (2001).

[Walker97] T.G. Walker and W. Happer. Spin-exchange optical pumping of noble-gas nuclei. **Rev. Mod. Phys., 69**, 629-642 (1997).

[Walker89] T.G. Walker. Estimates of spin-exchange parameters for alkali-metal-noble gas pairs. **Phys. Rev. A, 40**, 4959-64, (1989).

[Walter98] D.K. Walter, W. Happer and T.G. Walker. Estimates of the relative magnitudes of the isotropic and anisotropic magnetic-dipole hyperfine interactions in alkali-metalnoble-gas systems. **Phys. Rev. A, 58**, 3642-53, (1998).

[Walter01] D.K. Walter, W.M. Griffith and W. Happer. Energy transport in high-density spin-exchange optical pumping cells. **Phys. Rev. Lett., 86**, 2364-8 (2001).

[Wang03] G. Wang, W. Shao and E.W. Hughes. Highly polarized ^{3}He by spin exchange with potassium. **Phys. Rev. A, 68**, 65402(4), (2003).

[Wilms97] E. Wilms, M. Ebert, W. Heil and R. Surkau. Polarimetry on dense samples of spin-polarized ^{3}He by magnetostatic detection. **Nucl. Instrum. & Methods A, 401**, 491, (1997).

[Wieman91] C. Wieman and L, Hollberg. Using diode lasers for atomic physics. **Rev. Sci. Instrum., 62**, 1-20, (1991).

[Wu86] Z.Wu, M. Kitano, W. Happer, M. Hou, and J. Daniels. Optical determination of alkali metal vapor number density using Faraday rotation. **Applied Optics, 25**, 4483-91, (1986)

[Xu00] W. Xu, et al. Transverse asymmetry A_T' from the quasielastic ^{3}He $--> (e--> , e')$ process and the neutron magnetic form factor. **Phys. Rev. Lett., 85**, 2900-4, (2000).

[Young97] A.R. Young, S. Appelt, A.B. Baranga, C. Erickson and W. Happer. Three-dimensional imaging of spin polarization of alkali-metal vapor in optical pumping cells. **Appl. Phys. Lett., 70** 3081-3 (1997)

[Zhang99] X. Zhang, L. Zhu, Y. Wang, X. Liu, R. Feng, K. Xu, Z. Zhong. Optical oscillator strengths for $3^2S \rightarrow 4^2P$ and $3^2S \rightarrow 5^2P$ excitations of Na. **Chin. Phys. Lett., 16**, 882-4, (1999)